

REPORT 1319

CONTENTS

	Page
SUMMARY.....	851
INTRODUCTION.....	851
SYMBOLS.....	852
I. DEVELOPMENT OF INDUCED VELOCITY FIELDS BY SUPERPOSITION	
THEORY.....	853
The Wake Considered as a System of Coaxial Vortex Cylinders.....	853
Sample Calculation.....	853
Induced Velocity at Center of Rotor.....	854
A Limitation on the Analysis.....	855
CALCULATED RESULTS.....	855
Longitudinal Plane of Symmetry.....	855
Longitudinal Axis.....	856
Lateral Axis.....	856
Other Regions.....	856
DISCUSSION OF CALCULATED RESULTS.....	856
Longitudinal Plane of Symmetry.....	856
Longitudinal Axis.....	856
Lateral Axis.....	856
CONCLUDING REMARKS FOR PART I.....	870
II. SYMMETRY RELATIONS AND THE RELATION BETWEEN RADIAL LOAD DISTRIBUTION AND THE DOWNWASH DISTRIBUTION IN THE WAKE	
SYMMETRY RELATIONS CONCERNING THE INDUCED VELOCITIES IN THE PLANE OF THE ROTOR.....	870
Points on the Rotor Disk.....	870
Points Outside the Rotor Disk.....	871
Flow About an Elliptic Cylinder.....	872
RELATIONS BETWEEN THE RADIAL VARIATION OF DISK LOADING AND THE RADIAL VARIATION OF DOWNWASH VELOCITY WITHIN THE DOWNSTREAM WAKE.....	872
The Case $\chi=0^\circ$	872
The Case $0^\circ<\chi<90^\circ$	872
The Case $\chi=90^\circ$	873
CONCLUSIONS FOR PART II.....	875
III. ANALYSIS AND COMPARISON WITH THEORY OF FLOW-FIELD MEASUREMENTS NEAR A LIFTING ROTOR IN THE LANGLEY FULL-SCALE TUNNEL	
APPARATUS AND TESTS.....	875
CORRECTIONS.....	875
PRECISION.....	876
RESULTS AND DISCUSSION.....	877
Basic Data.....	877
Discussion of Applicable Theory.....	877
Comparison of Measured Data With Calculated Values of Reference 6 and Part I.....	877
Longitudinal plane of symmetry.....	877
Longitudinal axis.....	877
Lateral axis.....	877
Comparison of Measured Data With Calculated Values of Reference 5.....	883
Modification of calculations for finite lift coefficient.....	883
Plane of rotor.....	883
Far wake.....	884
Nature of the Flow.....	895
CONCLUSIONS FOR PART III.....	897
REFERENCES.....	897
APPENDIX—BASIC DATA.....	897

REPORT 1319

INDUCED VELOCITIES NEAR A LIFTING ROTOR WITH NONUNIFORM DISK LOADING¹

By HARRY H. HEYSON and S. KATZOFF

SUMMARY

A theoretical and experimental investigation of the induced velocities near a lifting rotor has been conducted. The results are presented in three parts.

Part I presents a method for computing, from available calculations for uniform disk loading, the effect of nonuniform circularly symmetrical disk loading on the normal component of induced velocity in the vicinity of a lifting rotor. Charts of the normal component of induced velocity are given for the longitudinal plane of symmetry and for the major axes of rotors with two different, nonuniform circularly symmetrical disk-load distributions. It is shown that the normal component of induced velocity must be zero at the center of any practical rotor. A comparison of the results of this report with those for a uniform disk loading shows that nonuniform disk loading has a powerful effect on the induced velocity distribution and that it must be taken into account in estimating the effect of the rotor on most components of an aircraft.

Part II develops certain symmetry relations for the induced velocities in the plane of a uniformly loaded rotor and also develops relations between the radial load distribution of the rotor and the radial variation of induced velocities in the wake.

Part III presents the results of an investigation in the Langley full-scale tunnel of the induced flow near a lifting rotor. Measurements of stream angles and velocities were made in several transverse planes along and behind the rotor in four different conditions representative of the cruising and high-speed ranges of flight. These measurements indicate that available theory may be used to calculate with reasonable accuracy the induced flow over the forward three-quarters of the disk for these flight conditions provided that a realistic nonuniform rotor disk-load distribution is assumed. Rearward of the three-quarter-diameter point, calculations of the induced velocity are increasingly inaccurate due to the rolling up of the trailing-vortex system. Farther rearward, well behind the rotor, the flow may be represented more accurately by the flow behind a uniformly loaded wing.

INTRODUCTION

A knowledge of the flow induced by a lifting rotor is necessary in any detailed study of the characteristics of a helicopter or convertiplane. The induced flow is one of the most

important factors involved in fuselage downloads or in the performance and loading of the wings of convertiplanes. Large effects on stability may also be experienced as a result of the induced flow acting on the tail surfaces. The rotor-induced flow actually involves a problem of unsteady aerodynamics, however, a knowledge of the time-averaged velocities should be sufficient for study of the problems mentioned. Experimental evidence (ref. 1) indicates that the time-averaged induced velocities may also be sufficient to estimate the interference between the rotors of multiple-rotor configurations. However, the differences between the time-averaged and the instantaneous velocities (ref. 2) is such that a more rigorous approach is probably required for accurate analyses (for example, blade vibrations) of the rotor system.

Even the time-averaged velocities have proved difficult to compute, but several simplified analyses are available (for example, refs. 3 to 6). These analyses are limited by the restricted number of locations for which the calculations have been made and also by the fact that the loading is usually assumed to be uniform. The most complete treatment is that of reference 6, which computes the normal component of induced velocity along the rotor axes and throughout the longitudinal plane of symmetry. Despite the assumption of uniform loading and the restriction to a single plane, it was hoped that the calculations would prove adequate to explain the effect of the rotor on short-span tail surfaces. Such, however, is not the case, for the results of wind-tunnel tests of the present investigation indicate that the induced velocity at typical tail locations may differ from that of reference 6 by as much as 1½ times the mean induced velocity at the rotor. One principal cause of this difference is the fact that the disk loading on an actual rotor is far from uniform as is assumed in reference 6.

In view of the difficulty of calculating the induced velocities, it would be expected that comprehensive measurements of these velocities would be available. However, the actual direct measurement of these velocities in flight or in small wind tunnels has proved to be exceedingly difficult. Several previous investigations have provided some qualitative information by the use of smoke, but quantitative measurements are relatively scarce. (A comprehensive review and

¹ Supersedes NACA Technical Note 3650 by Harry H. Heyson and S. Katzoff, 1956, and 3661 by Harry H. Heyson, 1956.

bibliography on induced-flow measurements is given in ref. 7.) Such measurements as are available are generally inadequate in scope to provide designers with sufficient experimental information or to define the general nature of the flow.

The present investigation attacks the problem both theoretically and experimentally. The report is divided into three parts as follows: Part I uses the results of reference 6 to build up by superposition the induced flow near a rotor having any arbitrary axisymmetric nonuniform distribution of disk load. For two rotors having different realistic disk-load distributions, charts of the normal component of induced velocity are given. Part II contains analytical treatments of some interesting characteristics of the downwash field that were observed during the course of the calculations for part I. More specifically, this part develops certain symmetry relations for the induced velocities in the plane of the uniformly loaded rotor as well as relations between the radial load distribution of the rotor and the radial variation of induced velocities in the wake. Part III presents the results of an experimental investigation conducted in the Langley full-scale tunnel. Stream-angle and dynamic-pressure measurements were made in several transverse planes near a rotor. The simulated flight conditions were chosen so as to represent a helicopter in level flight at normal cruising speeds. The tip-speed ratios range between 0.095 and 0.232; the calculated skew angles, between 75.0° and 85.8°. Essentially all of the basic data are presented in order to provide the maximum possible amount of experimental information for design purposes. At those locations for which theoretical calculations are available, the data are compared with theory in order to indicate the extent to which the theory is adequate and also to determine the general nature of the flow.

SYMBOLS

The following symbols are typical of usual rotary-wing terminology and are used throughout parts I and III of this report. The usual complex-variable symbols are used in part II since they are more convenient for that analysis. The symbols for part II are defined separately in that portion of the report.

A	area
b	number of blades
C_L	rotor lift coefficient, $\frac{L}{\frac{\rho V^2}{2} \pi R^2}$
C_T	rotor thrust coefficient, $\frac{T}{\rho (\Omega R)^2 \pi R^2}$
f	equivalent flat-plate area representing parasite drag, based on unit drag coefficient, $\frac{\text{Helicopter parasite drag}}{\frac{\rho V^2}{2}}$, sq ft
i	complement of skew angle (used in ref. 5 as angle of attack of rotor tip-path plane), deg
L	lift, lb
q	dynamic pressure, lb/sq ft
q_0	free-stream dynamic pressure, lb/sq ft

r	blade-element radius, ft
R	rotor radius, ft
R_v	radius of vortex cylinder, ft
s	semispan of wing, ft
T	rotor thrust, lb
v	normal component of induced velocity, positive downward, ft/sec
v_0	average or momentum theory value of the normal component of induced velocity, positive downward, ft/sec
V	forward speed of rotor, ft/sec
X	distance parallel to longitudinal rotor tip-path-plane axis, measured positive rearward from center of rotor, ft (fig. 1)
Y	distance parallel to lateral rotor tip-path-plane axis, measured positive on advancing side of disk from center of rotor, ft (fig. 1)
Z	distance parallel to axis perpendicular to rotor tip-path plane, measured positive above rotor from center of rotor, ft (fig. 1)
α	rotor control-axis angle of attack, radians
γ	vorticity, radians/sec
Γ	circulation, ft ² /sec
Γ'	circulation at tip of blade, ft ² /sec
λ	inflow ratio, $\frac{V \sin \alpha - v_0}{\Omega R}$
μ	tip-speed ratio, $\frac{V \cos \alpha}{\Omega R}$
ρ	mass density of air, slugs/cu ft
χ	rotor wake skew angle, angle between Z -axis of tip-path plane and axis of skewed wake, positive rearward from Z -axis, deg (fig. 1)
Ω	rotor angular velocity, radians/sec

Note that the definitions of X , Y , and Z , together with the direction of rotation of the rotor in part III of this investigation, result in a left-handed axis system.

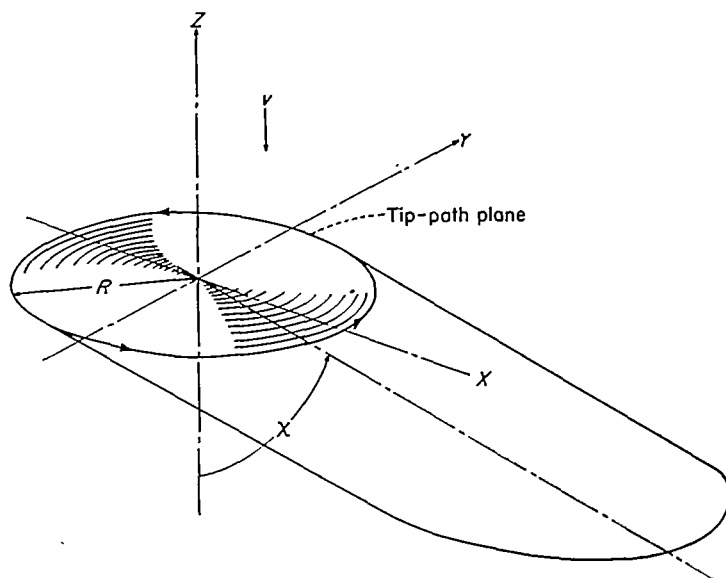


FIGURE 1.—Coordinate system of rotor and wake. Arrows denote positive direction.

I. DEVELOPMENT OF INDUCED VELOCITY FIELDS BY SUPERPOSITION

By Harry H. Heyson

THEORY

THE WAKE CONSIDERED AS A SYSTEM OF COAXIAL VORTEX CYLINDERS

For the present simplified theory, the forward speed of the rotor is assumed negligible relative to the rotational speed of the blades. Then, at any radial location, the local velocity of a blade element is simply Ωr , so that the lift per unit radial distance can be written

$$\frac{dL}{dr} = b\rho\Omega r\Gamma \quad (1)$$

where Γ , in general, is a function of r . The local disk loading (or annulus loading) is

$$\text{Local disk loading} = \frac{b\rho\Omega r\Gamma dr}{2\pi r dr} = \frac{b\rho\Omega\Gamma}{2\pi} \quad (2)$$

In general, as illustrated by equations (1) and (2), the local disk loading varies as $\frac{1}{r}$ times the blade loading. Thus, a uniform disk loading implies a triangular blade loading, and a triangular disk loading implies a parabolic blade loading.

Equation (2) also shows that for a uniform disk loading the circulation is constant along the blade. For this case, vorticity is accordingly shed only at the blade tips, and the wake consists of a single vortex cylinder (fig. 2 (a)). In references 3 and 6, where the lifting rotor is represented by a uniformly loaded disk, the downwash field is correspondingly calculated as the downwash field of this single vortex cylinder.

If, however, the disk loading is not uniform, the circulation varies along the length of the blade and vorticity must be shed all along the blade instead of only at the tip. Consequently, a rotor having nonuniform disk loading must be represented by a distribution of shed vortex cylinders.

In the present calculations, these cylinders are all assumed parallel and concentric (see fig. 2 (b)) and are inclined at a skew angle defined by the forward velocity of the rotor and the momentum-theory value of the rotor induced velocity. Such an assumption presents obvious inconsistencies, because such an idealized geometry could not be produced or maintained in the nonuniform induced-flow field that it itself creates. In spite of such inconsistencies, however, the arrangement of concentric cylinders is probably a better basis for computations than a single vortex cylinder trailing from the blade tips.

It is possible to consider that the solution of reference 6 represents the flow generated by any one of these vortex cylinders. The radius used in that report should now be considered to be the radius R_* of the individual vortex cylinder. The contribution of any single vortex cylinder to the total induced flow at a point $\left(\frac{X}{R}, \frac{Y}{R}, \frac{Z}{R}\right)$ may be read directly from the charts of reference 6 at the point $(X/R)(R/R_*), (Y/R)(R/R_*), (Z/R)(R/R_*)$.

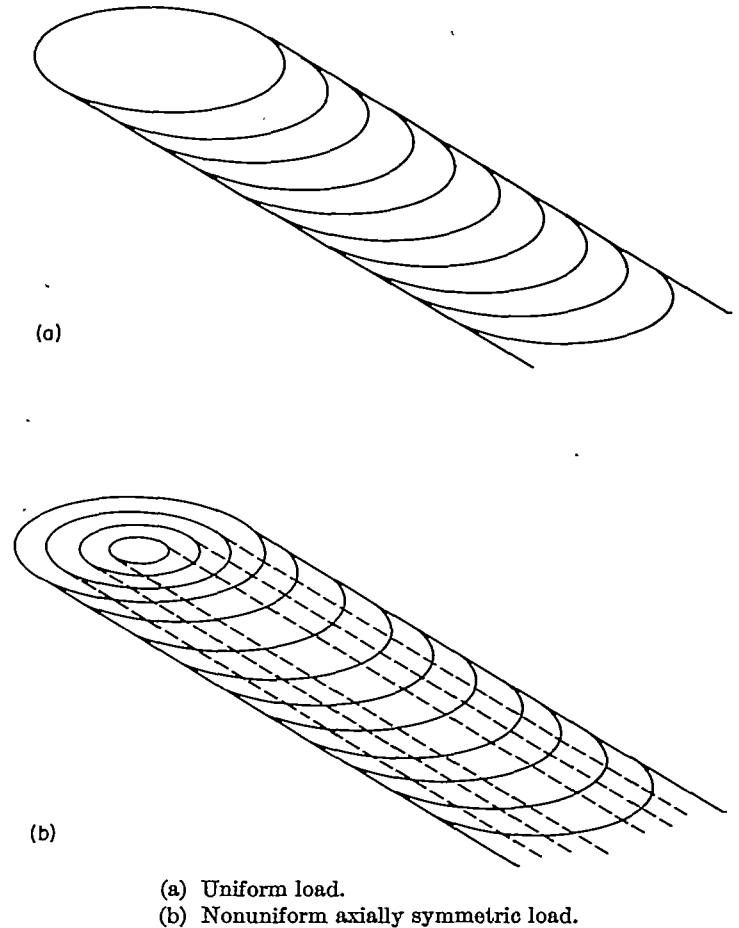


FIGURE 2.—Assumed vortex pattern of rotor wake.

In practice, any arbitrary circularly symmetrical rotor disk-load distribution may be approximated by the sum of the loads carried by a finite number of superposed concentric vortex cylinders of suitable strength and dimensions. Then the induced velocity field of the nonuniformly loaded rotor will be the sum of the superposed induced velocity fields of the vortex cylinders comprising its wake.

Some difficulty may be anticipated because of the discontinuities in the flow at the edges of the vortex cylinders. In practice, however, only a small error occurs if a sufficient number of vortex cylinders are used, and the points of discontinuity themselves are avoided.

SAMPLE CALCULATION

In order to demonstrate the method of superposition, the induced velocity at the point $\left(\frac{X}{R}=0.2, \frac{Y}{R}=0, \frac{Z}{R}=0.1\right)$ will be calculated for a rotor with a triangular disk loading and operating at a skew angle of 90° .

As shown previously, the local disk loading is proportional to Γ ; therefore, for uniform disk loading the circulation is constant along the blade. If the disk loading is triangular,

$$\Gamma = \Gamma' \frac{r}{R}$$

so that the local disk loading is

$$\text{Local disk loading} = \frac{b\rho\Omega}{2\pi} \Gamma' \frac{r}{R}$$

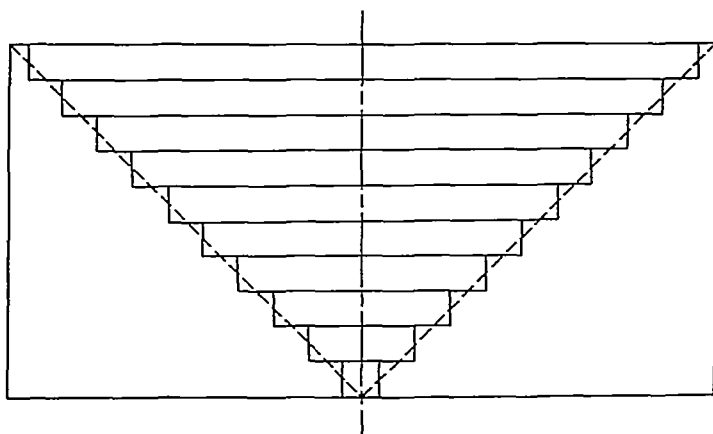
and the average disk loading for the entire rotor is

$$\begin{aligned} \text{Average disk loading} &= \frac{1}{\pi R^2} \int_0^R \frac{b\rho\Omega}{2\pi} \Gamma' \frac{r}{R} 2\pi r dr \\ &= \frac{b\rho\Omega\Gamma'}{3\pi} \end{aligned}$$

Thus, for this case of the triangular disk loading,

$$\text{Local disk loading} = \frac{3}{2} \frac{r}{R} \times (\text{Average disk loading})$$

Thus, the vortex field of a rotor with a triangular loading may be represented by one positive vortex cylinder with the same radius as the blade tips and a strength 1.5 times as great as a uniformly loaded rotor, plus ten equal negative vortex cylinders of smaller radii and a strength 0.15 times as great as a uniformly loaded rotor. The sum of the resulting disk loads is shown in sketch 1 and adequately represents a triangularly loaded rotor:



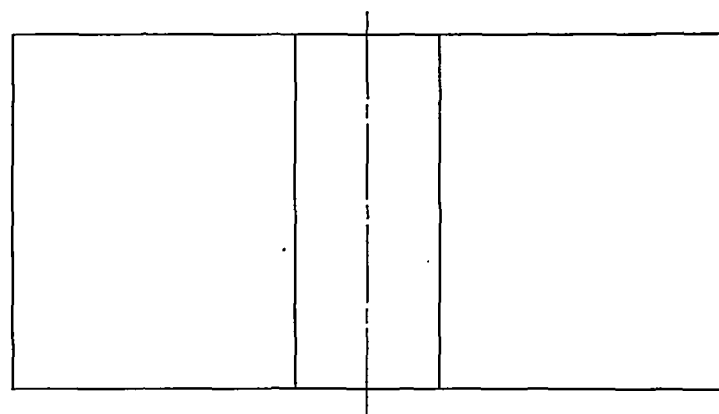
Sketch 1.

The contribution of each vortex cylinder may be found from figure 4 (g) of reference 6.

The computation may be carried out in tabular form as follows:

$\left(\frac{R_1}{R}\right)$	$\left(\frac{X}{R}\right)\left(\frac{R}{R_1}\right)$	$\left(\frac{Y}{R}\right)\left(\frac{R}{R_1}\right)$	$\left(\frac{Z}{R}\right)\left(\frac{R}{R_1}\right)$	$\left(\frac{v}{v_0}\right)$
1.00	0.200	0	0.100	1.15 (1.50) = 1.725
.95	.211	0	.106	1.15 (-.15) = -.173
.85	.236	0	.118	1.17 (-.15) = -.176
.75	.267	0	.134	1.19 (-.15) = -.179
.65	.308	0	.154	1.20 (-.15) = -.180
.55	.364	0	.182	1.21 (-.15) = -.182
.45	.445	0	.223	1.23 (-.15) = -.185
.35	.571	0	.286	1.24 (-.15) = -.186
.25	.800	0	.400	1.25 (-.15) = -.188
.15	1.330	0	.667	.95 (-.15) = -.143
.05	4.000	0	2.000	.26 (-.15) = -.039
				$v/v_0 = \Sigma(v/v_0) = 0.094$

It will be noted, in general, that the charts of reference 6 must be extrapolated to obtain the contribution of some of the smaller cylinders. Also, if the maximum loading does not occur at the tips, more than one positive vortex cylinder will be required to adequately represent the flow.

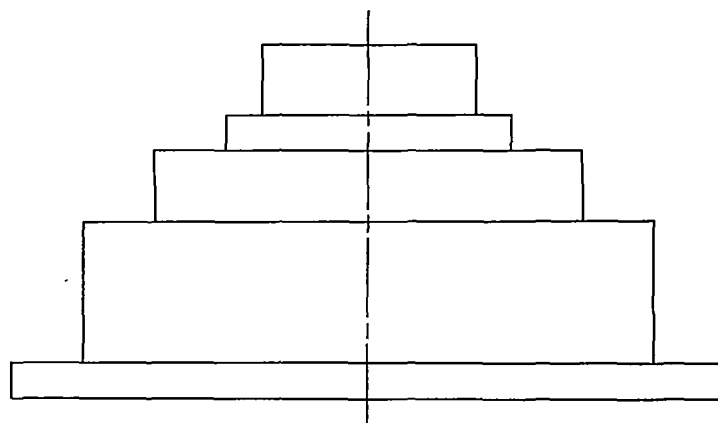


Sketch 2.

INDUCED VELOCITY AT CENTER OF ROTOR

Consider a rotor with a disk loading that is uniform everywhere except in a central "cut-out" portion where it carries no load. (See sketch 2.) The vortex field of this rotor may be represented by just two vortex cylinders of equal, but opposite, vorticity. Since the smaller cylinder has the same downwash field as the larger cylinder (except for dimensions), it follows that the induced velocity is zero at the center of the rotor disk. The same result, of course, will follow whenever any rotor has zero disk load at its center. Since all practical rotors have some cut-out near their centers (due to hub, etc.), they all must have zero induced velocity at their centers.

This result is a special case of a more general theorem which is occasionally useful in comparing the results of theoretical calculations made for several different load distributions. Consider a rotor with a step loading composed of a number of uniform loads of different radii such as in sketch 3. The vortex field of this rotor may be represented by several vortex cylinders of different strength. A uniformly loaded rotor produces an induced velocity of v_0 at its center. Therefore, the induced velocity at the center of the step-loaded rotor will be v_{01} (due to uniform load 1) plus v_{02} (due to uniform load 2) and so on. The final result is that the induced velocity at the center of the step-loaded rotor will then be the same as if the local load at the center existed over the entire disk rather than just at the center.



Sketch 3.

A LIMITATION ON THE ANALYSIS

It is important to note that the foregoing analysis is predicated upon a wake consisting of straight elliptic cylinders in which all of the vorticity is carried downward at some uniform velocity rather than the local velocities. The effect of this assumption is greatest in hovering for here the induced velocities are the sole velocities present. Since in this case the flow near the rotor center is carried away from the rotor at a much slower rate than the flow near the edges of the disk, the vorticity along the wake cylinders near the center must be correspondingly greater. In this extreme case, an appreciable error will be incurred in the computed induced velocities. However, when an appreciable flight velocity is imposed on the rotor, as in rapid vertical climb or in forward flight, the vortices will be carried downstream at a more uniform rate and the error will be small.

Since the assumptions of the present analysis are grossly violated in static thrust, this case may be used to give an indication of the maximum possible error. From momentum theory, for any annulus

$$dT = 4\pi r \rho v^2 dr$$

$$\frac{dT}{dA} = \frac{1}{2\pi r} \frac{dT}{dr} = 2\rho v^2$$

which shows that in static thrust, the local induced velocity should be proportional to the square root of the local disk loading. In contrast, under the assumptions of the present report, the induced velocity has been shown to be directly proportional to the disk loading. The effect of this difference on the induced velocities in the plane of a hovering triangularly loaded rotor is shown in figure 3. The momentum theory gives $\frac{v}{v_0} = \sqrt{\frac{3}{2} \frac{r}{R}}$ whereas the present vortex

theory gives $\frac{v}{v_0} = \frac{3}{2} \frac{r}{R}$. The maximum difference in induced velocity occurs at the tip of the rotor and is $0.275v_0$. Thus the results of the present vortex theory may be adequate to explain qualitatively certain trends even in hovering. For example, recent unpublished results from flow surveys below a hovering rotor indicate a region of upwash below the rotor center. Calculated results from the present theory for a triangularly loaded rotor also indicate the presence of an upwash in this region.

In forward flight the assumptions of this report are much less severe. For example, reference 6 gives the mean induced velocity at the rotor as

$$v_0 \approx \frac{\frac{1}{2} \Omega R C_T}{\left(1 - \frac{3}{2} \mu^2\right) \sqrt{\lambda^2 + \mu^2}}$$

For tip-speed ratios greater than 0.10, λ is small compared with μ so that the induced velocity will be proportional to the loading as herein assumed. Thus the charts which will be presented in the following section should be sufficiently accurate for the rotor in forward flight.

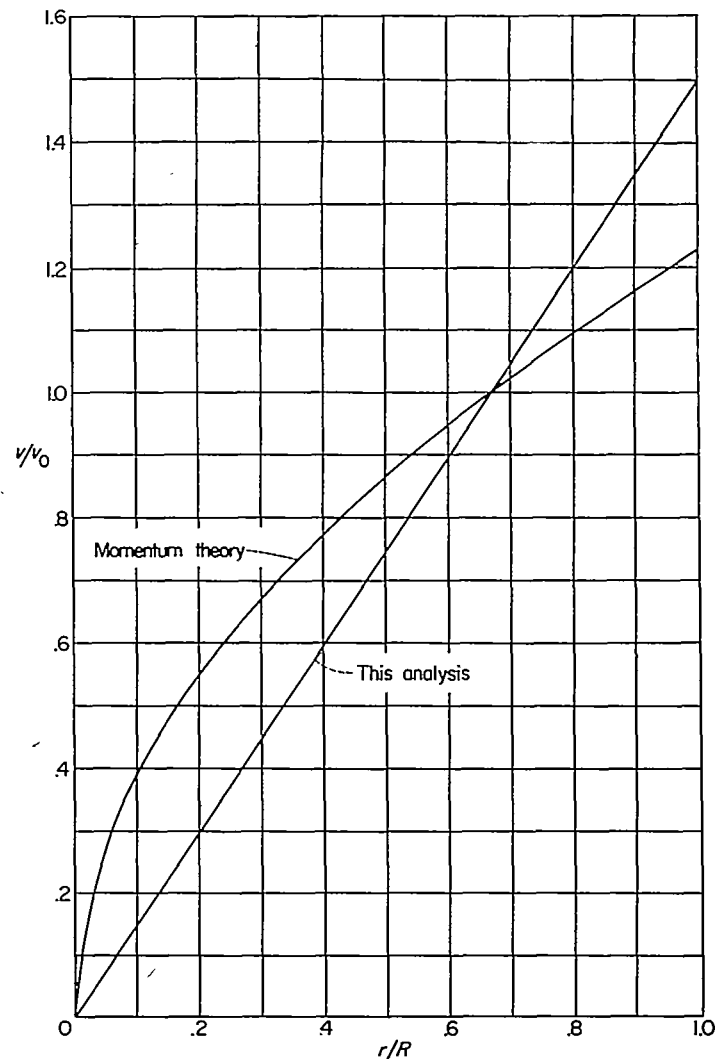


FIGURE 3.—Comparison of the results of momentum theory and present analysis for the induced velocities in the plane of a hovering, triangularly loaded rotor.

CALCULATED RESULTS

LONGITUDINAL PLANE OF SYMMETRY

A number of nondimensional charts of the induced velocity have been computed. These charts not only illustrate the effect of a nonuniform disk loading, but they may also be used as working charts for the determination of the induced velocity at points in the field of practical rotors. The calculations were made for rotors having two different, circularly symmetrical, nonuniform disk loadings. These assumed disk loadings are shown in figure 4. The triangular loading was chosen since it is the simplest approximation to the actual rotor disk loading in all flight conditions. The variation of disk load labeled "typical load" was measured at a typical cruising condition during tests in the Langley full-scale tunnel of a rotor equipped to measure the rotor-blade pressure distribution.

Figure 5 presents contour charts of the normal component of induced velocity in the longitudinal plane of symmetry for the rotor with a triangular disk loading for six different skew angles in the range from 0° to 90° . Figure 6 presents similar charts for a rotor having the typical measured disk-

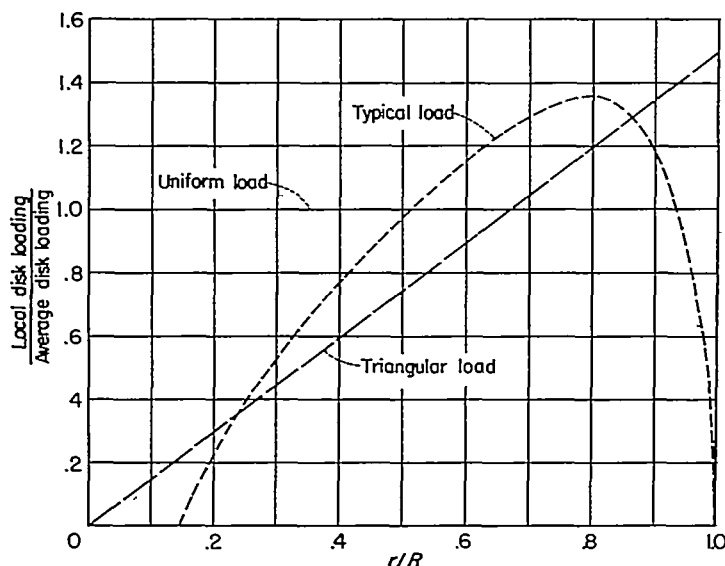


FIGURE 4.—Disk loadings considered in calculations.

load distribution for three different skew angles between 63.43° and 90° , which bracket the skew angle at which this load distribution was measured. Figures 5 and 6 may also be used to find the induced velocity distributions for skew angles between 90° and 180° (the autorotation range) if the Z/R scale is multiplied by -1 and the chart for the supplement of the desired skew angle is read.

LONGITUDINAL AXIS

Figures 7 and 8 present the induced velocity distribution along the X -axis (or longitudinal axis) of the rotors with the triangular and typical measured load distributions, respectively.

LATERAL AXIS

Figures 9 and 10 present the induced velocity distribution along the Y -axis (or lateral axis) of the same two rotors.

Figures 7 to 10 may be used for skew angles from 90° to 180° merely by reading the curves for the supplement of the desired angle.

Figure 9 indicates the order of accuracy of the calculations. Part II of this report will show that the variation of induced velocity on the lateral axis must be triangular if the disk loading is triangular. Actually, figure 9 indicates a slight upward curvature. The difference between these curves and straight lines is, however, small and could probably have been avoided by using a somewhat larger number of cylinders to represent the wake.

OTHER REGIONS

It would be interesting to carry out these calculations over the lateral planes where auxiliary devices such as wings, tail surfaces, or propellers would be located on flight machines. However, such calculations would be dependent upon a knowledge of the flow field of the uniformly loaded rotor and this flow field has not yet been computed. The flow in these regions can be calculated, if required, from considerations in reference 6 and the present report.

DISCUSSION OF CALCULATED RESULTS

LONGITUDINAL PLANE OF SYMMETRY

Figure 11 presents a chart of the induced velocity in the

longitudinal plane of symmetry of a uniformly loaded rotor at a skew angle of 63.43° (reproduced from ref. 6).

The effect of nonuniform axisymmetric loading may be seen by comparing figure 11 with figures 5 (d) and 6 (a). Since both of the assumed nonuniform loads are zero at the center of the rotor, the induced velocity at the center is zero in both cases, as opposed to a value of $v/v_0 = 1.0$ at the center of the uniformly loaded rotor. Both of the nonuniformly loaded rotors show an appreciable area of upwash just below and behind the center of rotation. They also show zero induced velocity further rearward on the center line of the wake. In this plane, the chart for the triangular load distribution shows a roughly triangular induced-velocity profile across the wake, and the chart for the typical measured load distribution shows a more rounded profile across the wake with a larger area of zero induced velocity reflecting the effect of the cut-out region in the vicinity of the hub. In contrast, the results for the uniformly loaded rotor case show the induced velocity building up continuously as the flow passes through the rotor and rearward in the wake until it reaches a uniform value of $v/v_0 = 2.0$ near the trailing edge of the rotor.

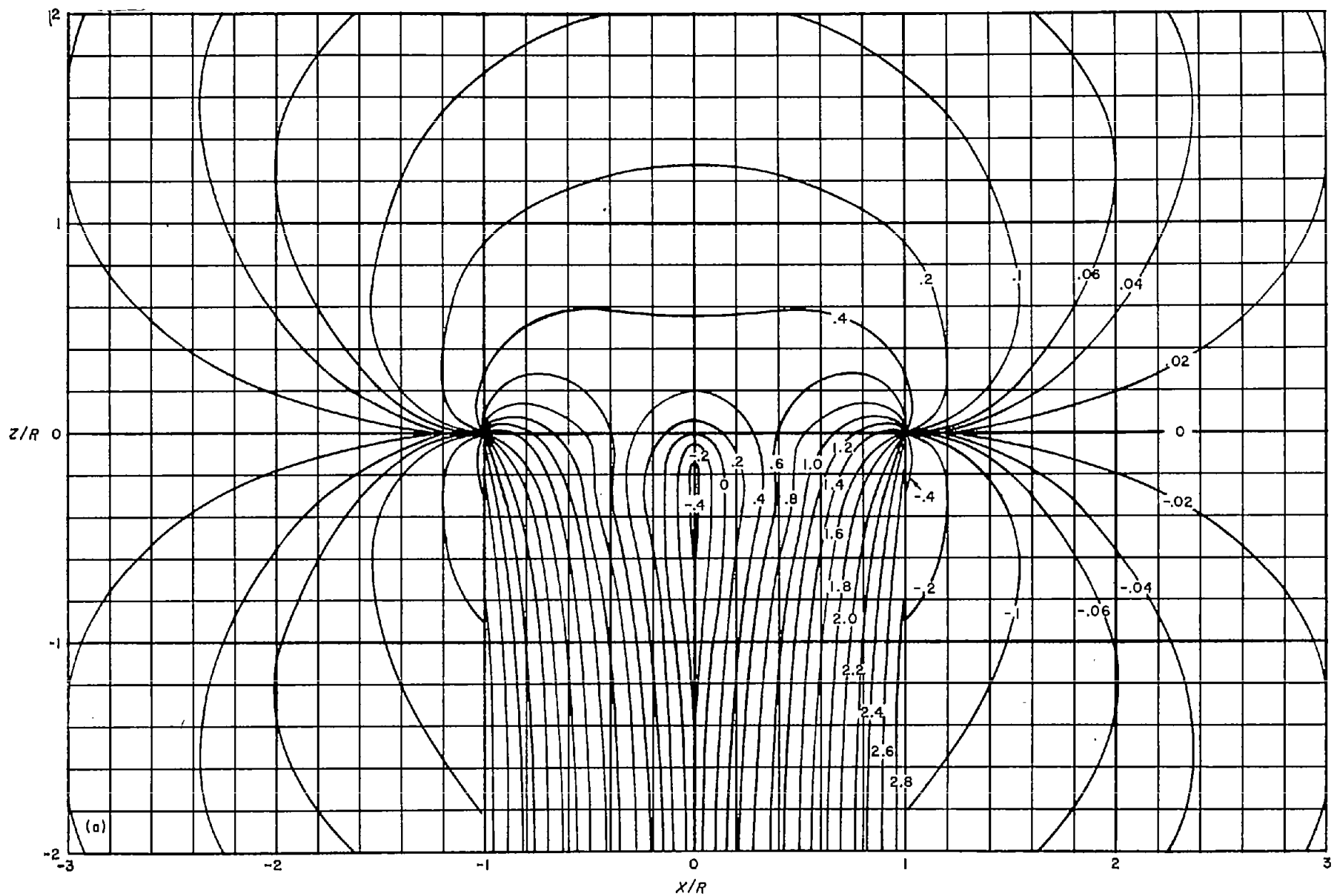
LONGITUDINAL AXIS

Figure 12 (obtained from figs. 7 and 8 and ref. 6) shows the calculated effect of rotor disk-load distribution on the induced-velocity distribution along the X -axis (longitudinal axis) of the rotor. This figure clearly shows the large effect caused by the requirement that the induced velocity be zero at the center of the rotor for each of the nonuniformly loaded cases. Each of the nonuniformly loaded rotors has an upwash just behind its center, whereas the uniformly loaded rotor has downwash values of $v/v_0 > 1$ in this region. The differences in induced velocity between the nonuniformly loaded rotors are small along this axis, however, the rotor with the typical measured load distribution does have a somewhat greater upwash behind the center as a result of the larger cut-out region.

LATERAL AXIS

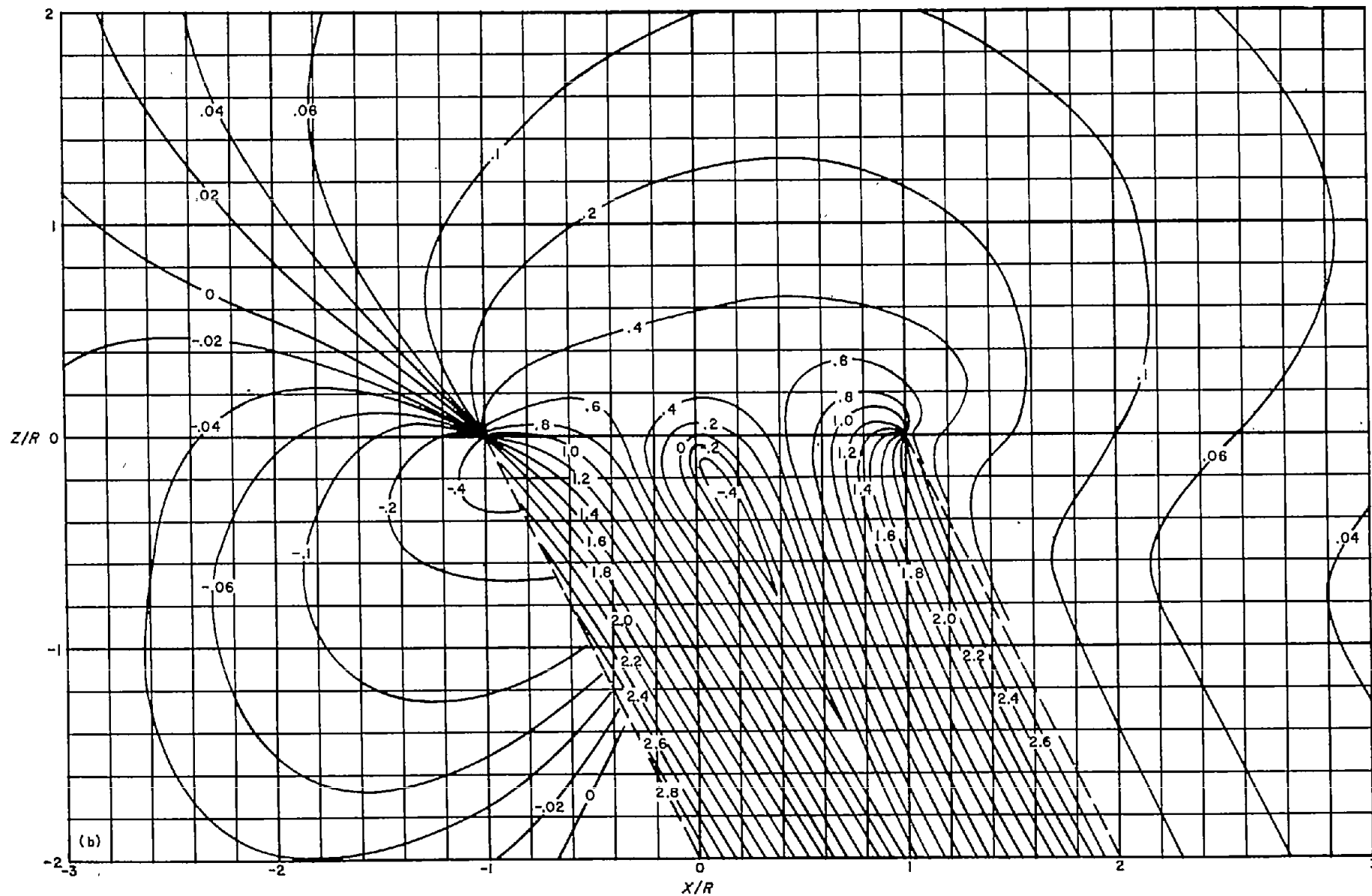
Figure 13 presents a similar comparison along the Y -axis (lateral axis) of the rotors at a skew angle of 90° . This figure shows that the lateral center-line distribution is closely similar in shape to the distribution of load on the disk. This similarity is discussed further in part II.

It should be noted that the distribution given for the uniformly loaded rotor is not the same as that given in reference 6, since in the present report the induced velocity is shown as being uniform across the lateral axis. A proof that the induced-velocity distribution must be uniform at this location is given in part II. In discussions between the senior author of reference 6 and the authors of the present report, it was suggested that the inaccuracy in the plane of the disk resulted from a basic difficulty in the computational procedure in the location near the edge of the disk. It is assumed that the values given in reference 6 are correct for locations outside the rotor tips. The calculations made for the present report were based on composite curves similar to the one shown in figure 13.



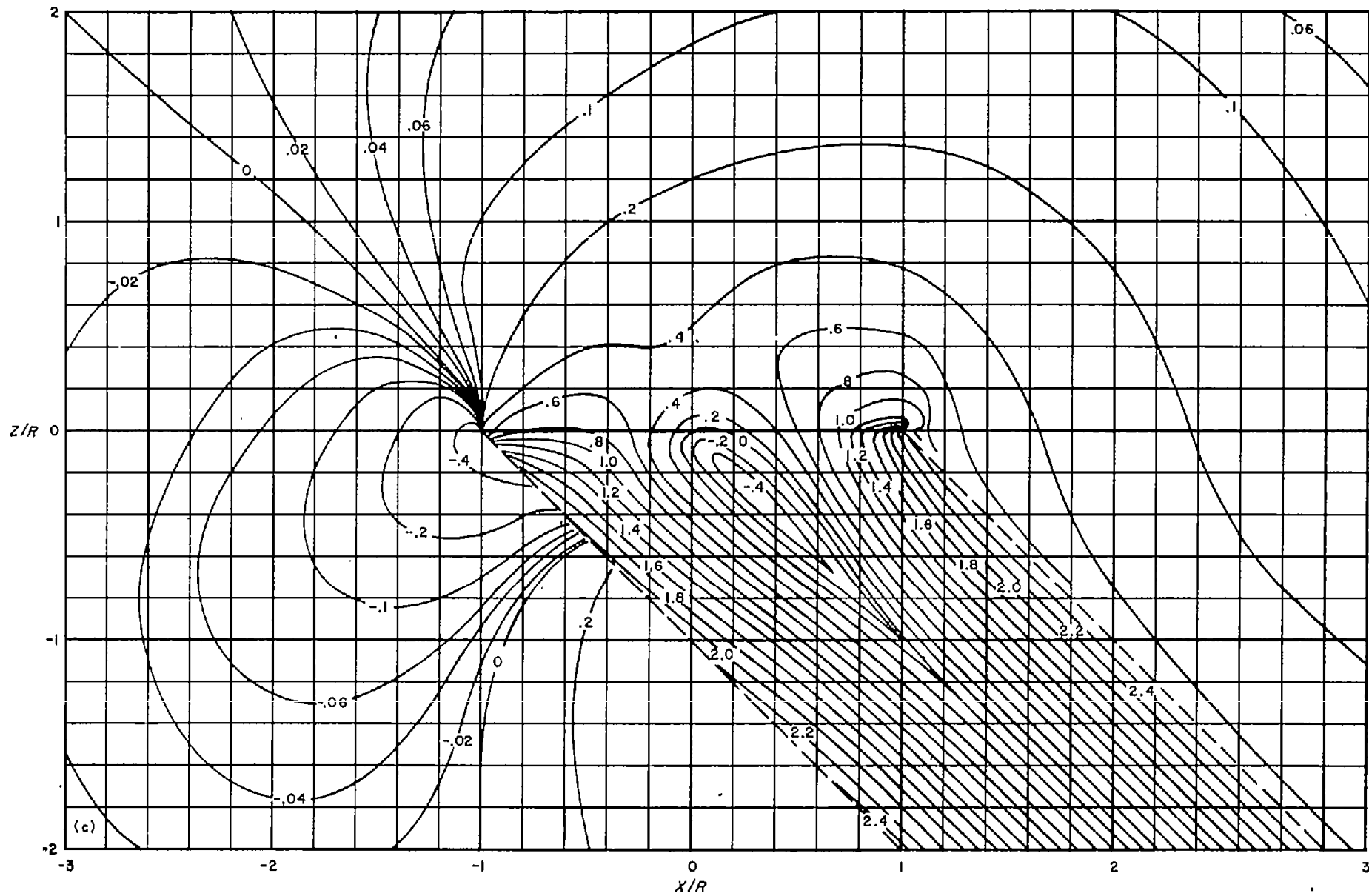
(a) $\chi = 0^\circ = \tan^{-1} 0$.

FIGURE 5.—Lines of constant value of induced velocity ratio v/v_0 in the longitudinal plane of symmetry of a rotor with a triangular disk load.



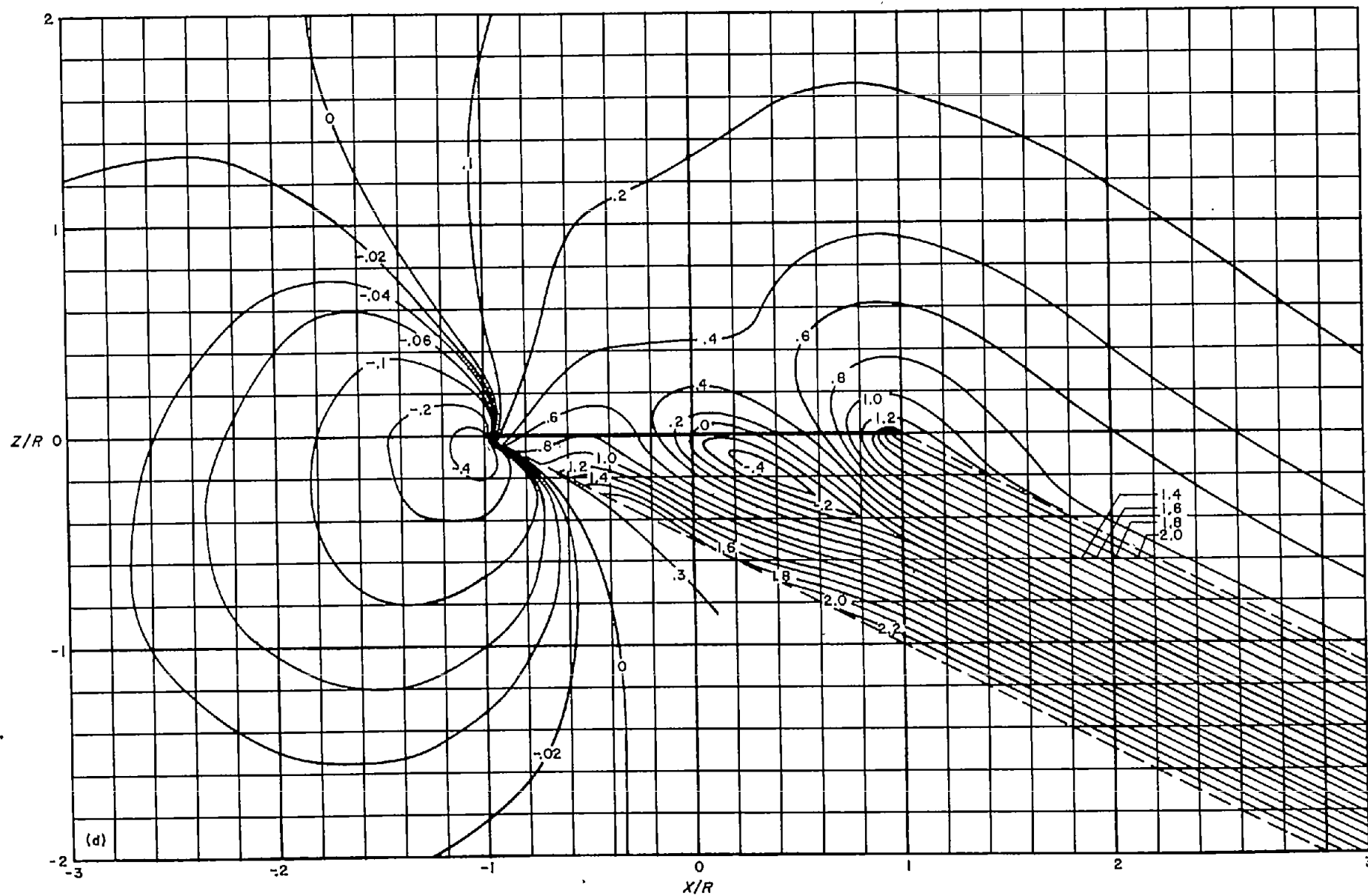
(b) $\alpha = 26.56^\circ = \tan^{-1} 1/2$.

FIGURE 5.—Continued.



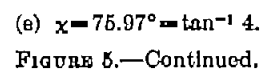
(c) $\alpha = 45^\circ = \tan^{-1} 1$.

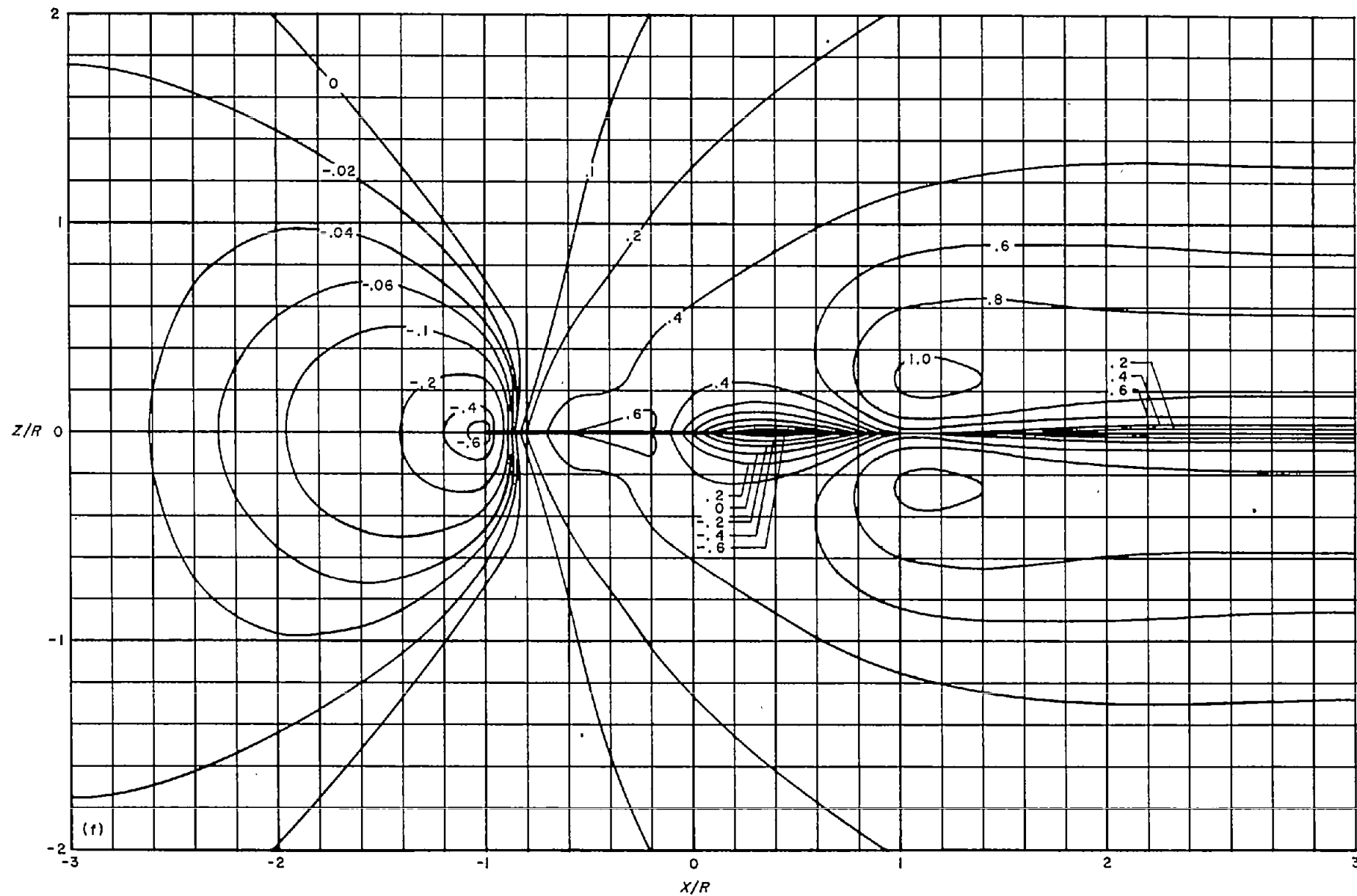
FIGURE 5.—Continued.



(d) $\chi = 03.43^\circ = \tan^{-1} 2$.

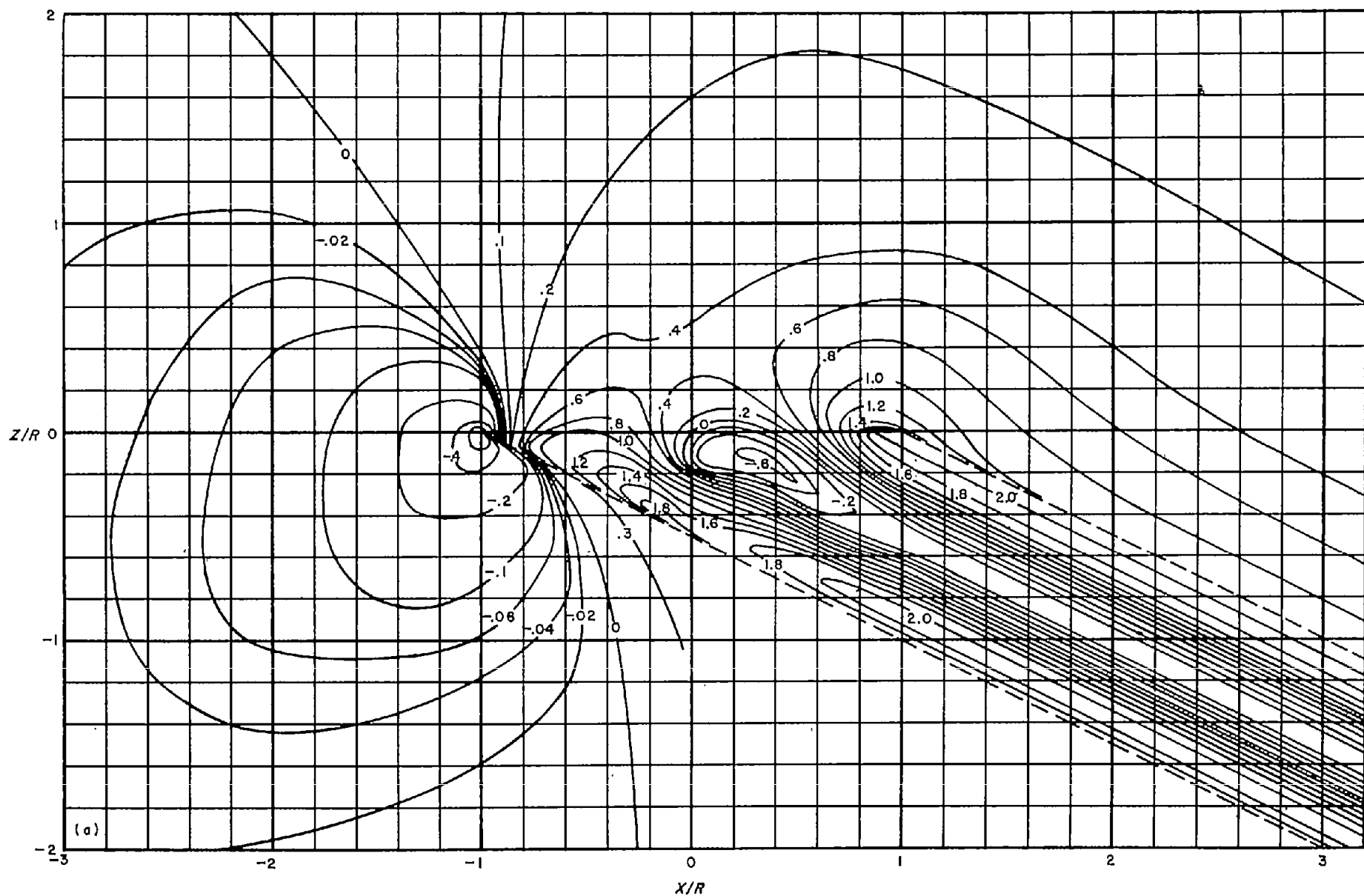
FIGURE 5.—Continued.





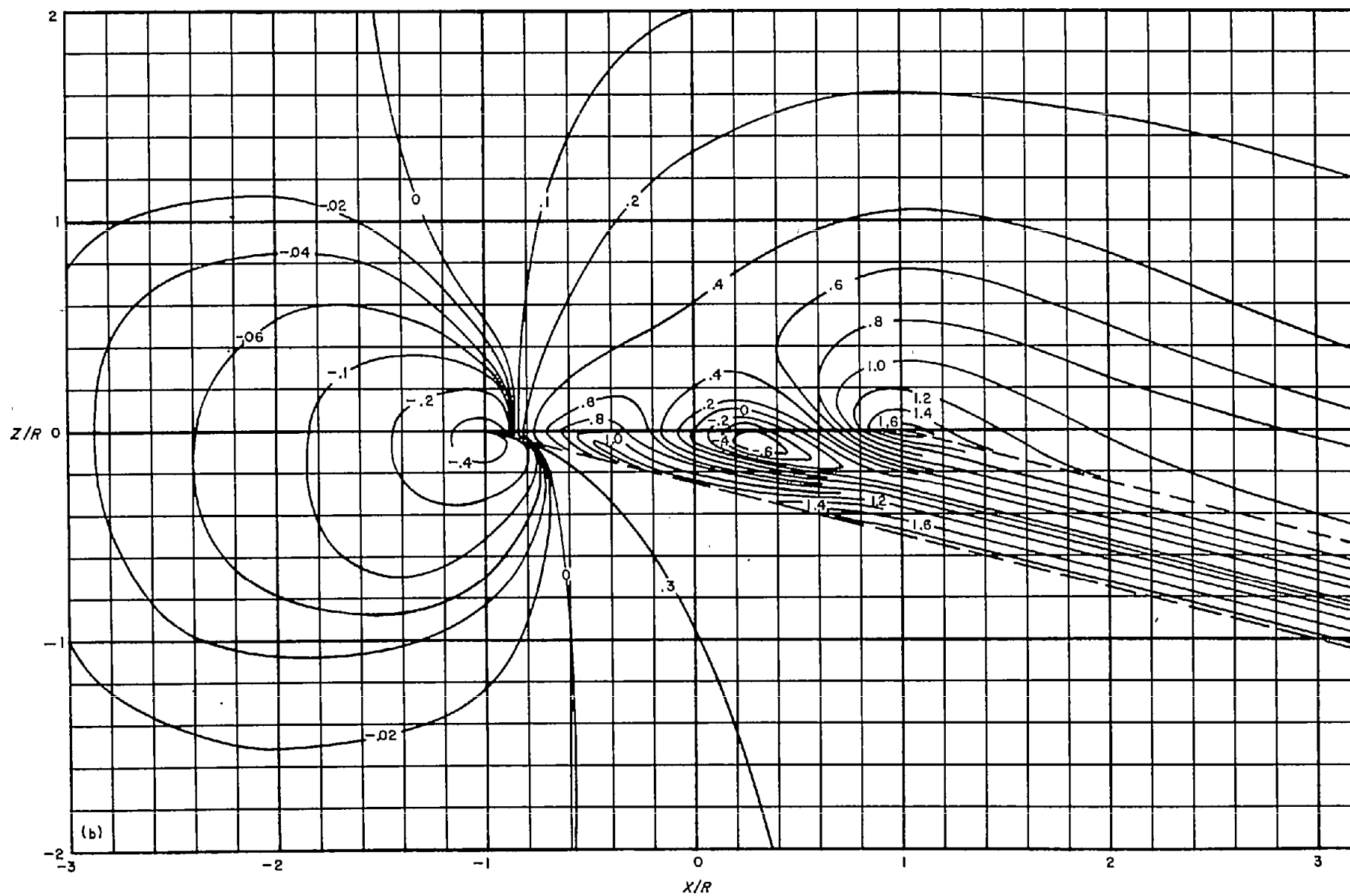
(f) $\chi = 90^\circ = \tan^{-1} \infty$.

FIGURE 5.—Concluded.



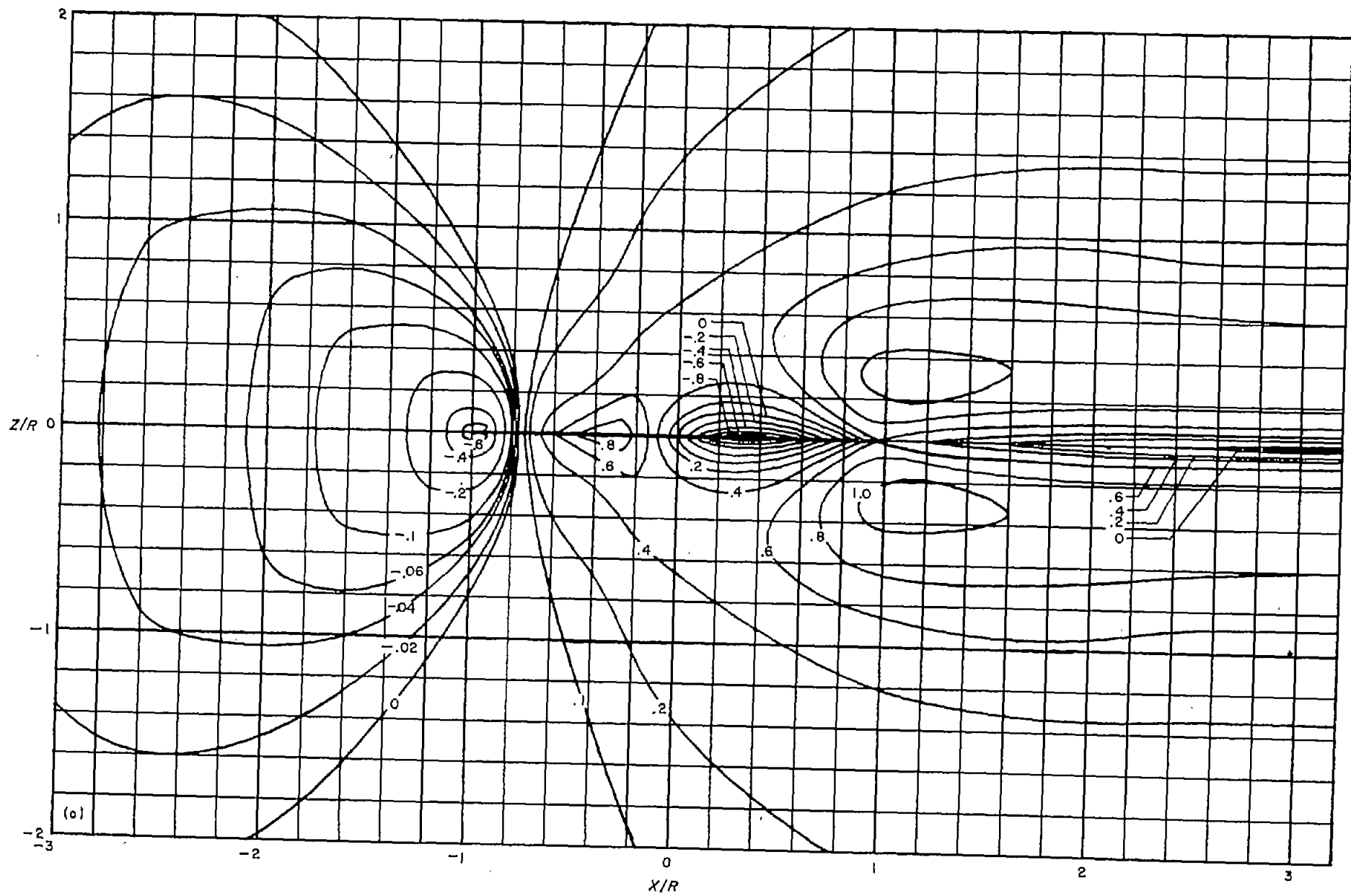
(a) $\chi = 03.43^\circ = \tan^{-1} 2$.

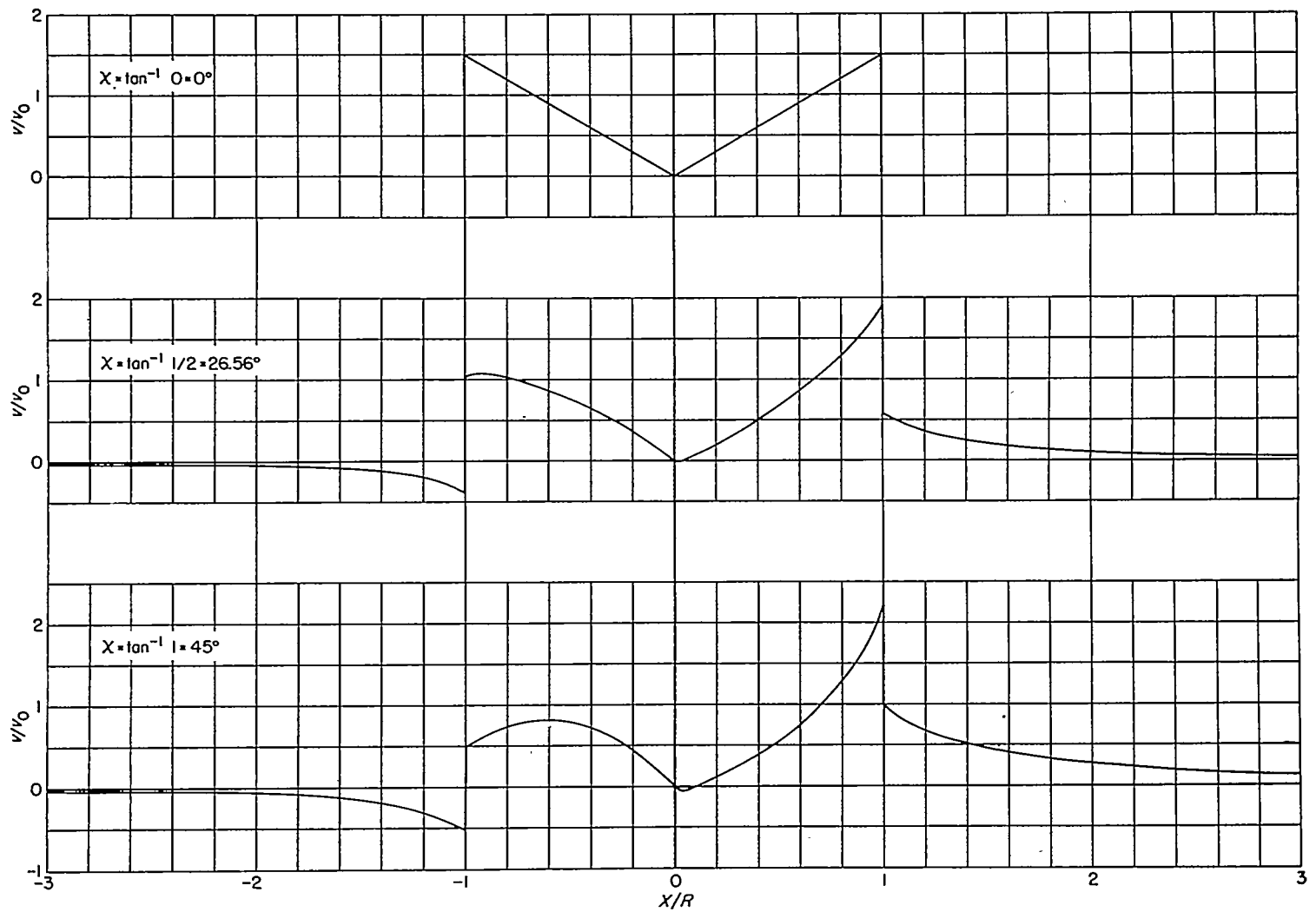
FIGURE 6.—Lines of constant value of induced velocity ratio v/v_0 in the longitudinal plane of symmetry of a rotor with a typical measured mean disk load.



(b) $\chi = 75.97^\circ = \tan^{-1} 4$.

FIGURE 6.—Continued.



FIGURE 7.—Induced velocity distribution along the X -axis of a rotor with a triangular disk load.

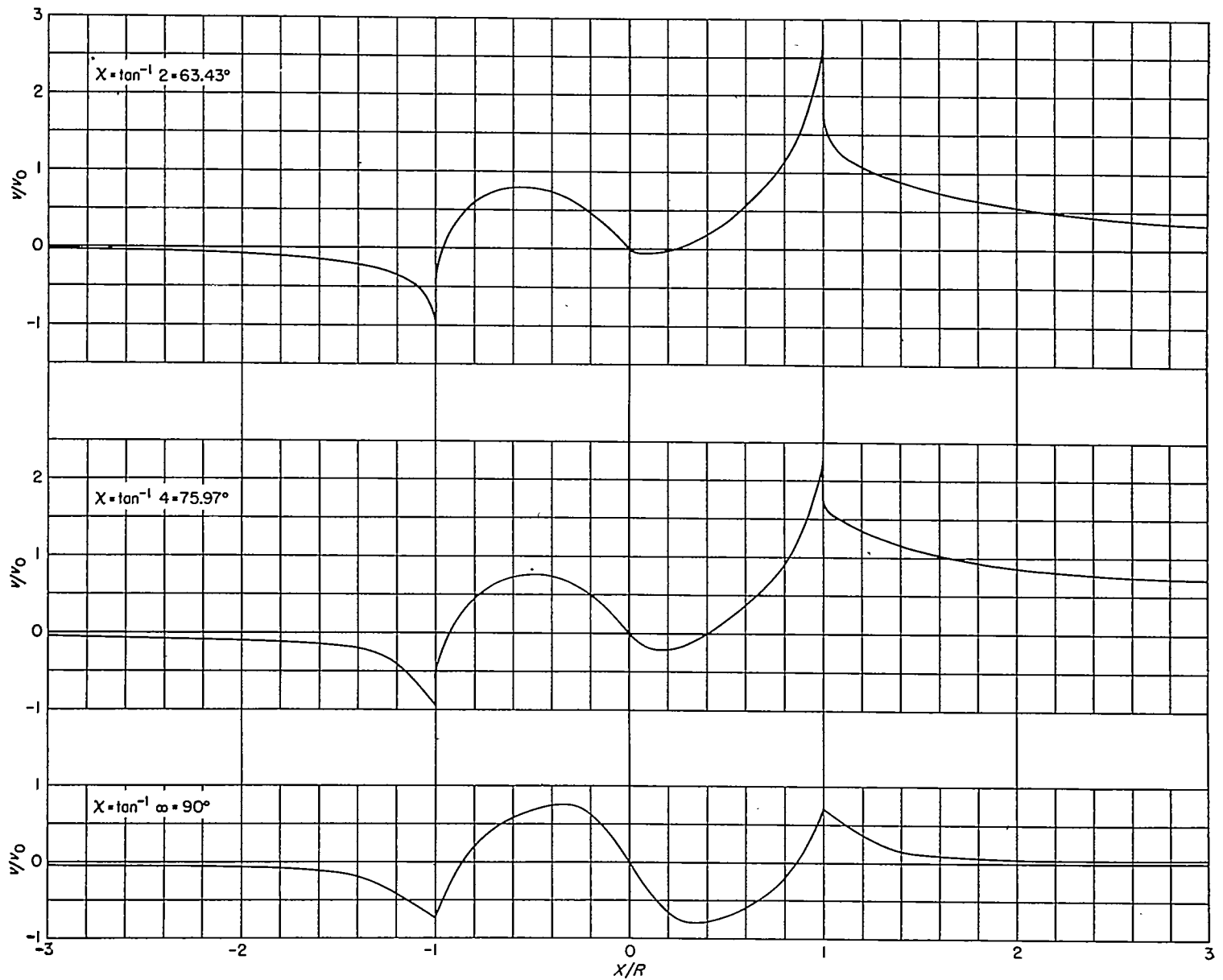
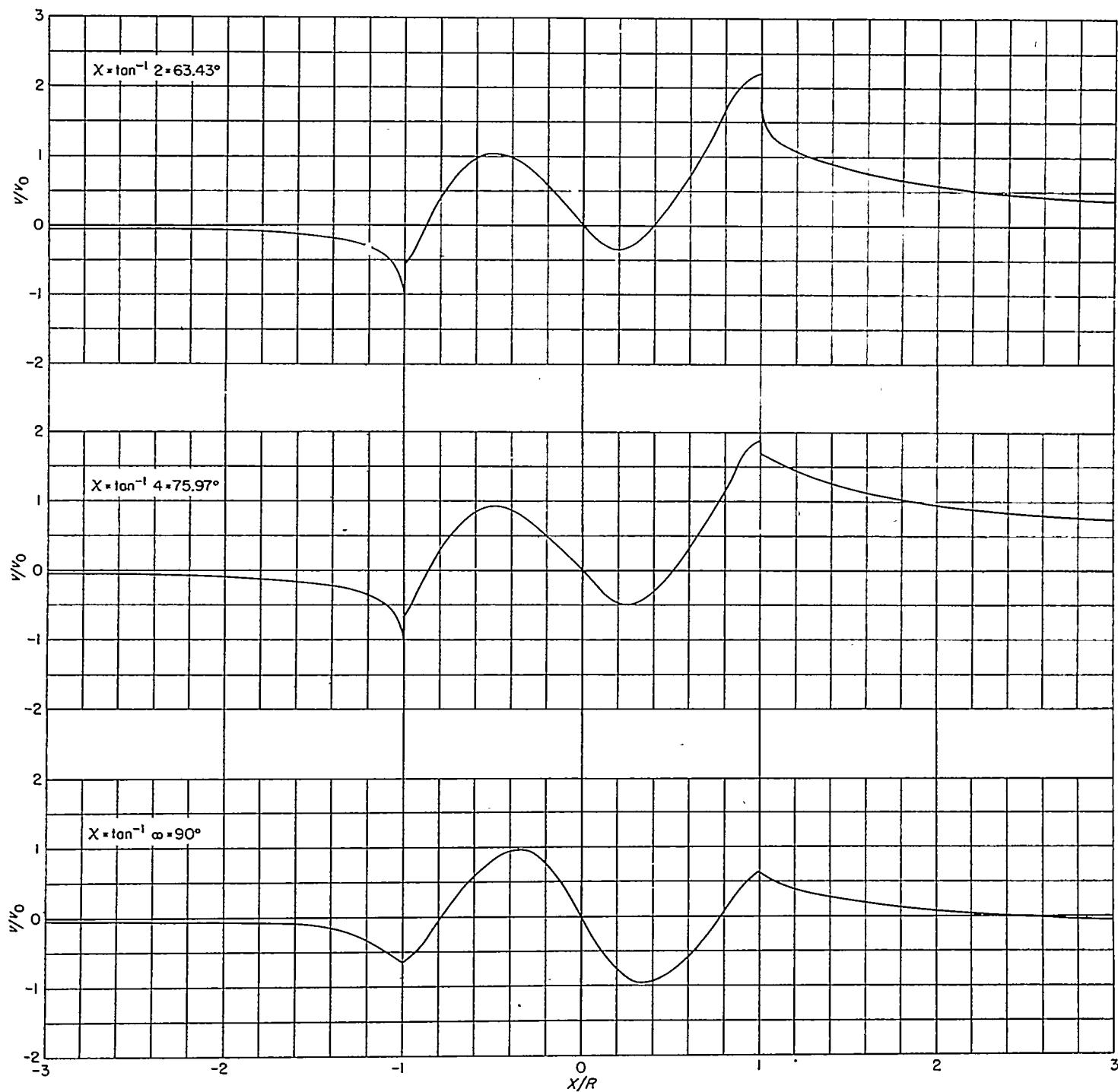


FIGURE 7.—Concluded.

FIGURE 8.—Induced velocity distribution along the X -axis of a rotor with a typical measured mean disk load.

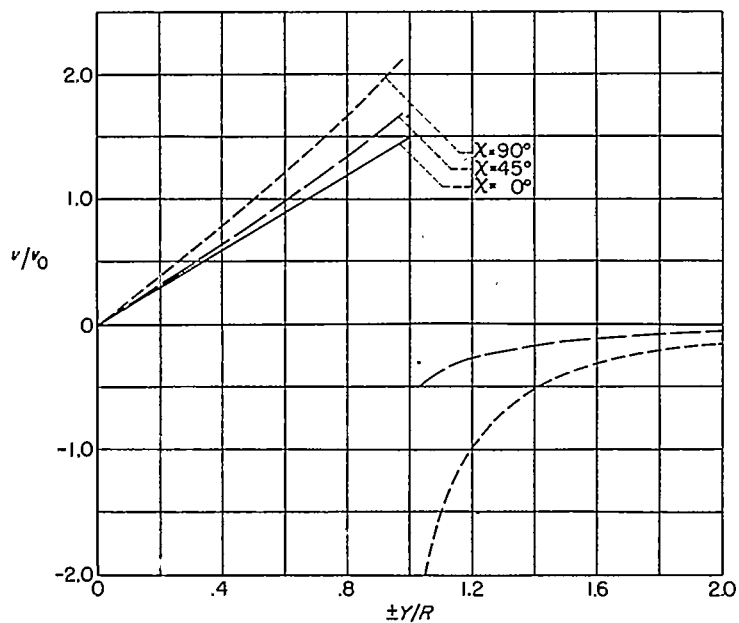


FIGURE 9.—Induced velocity distribution on the Y-axis of a rotor with a triangular disk load.

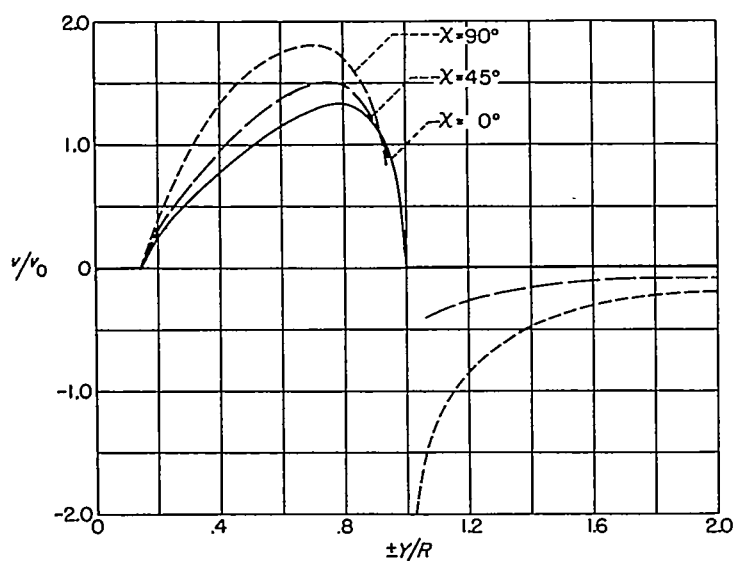


FIGURE 10.—Induced velocity distribution on the Y-axis of a rotor with a typical measured mean disk loading.

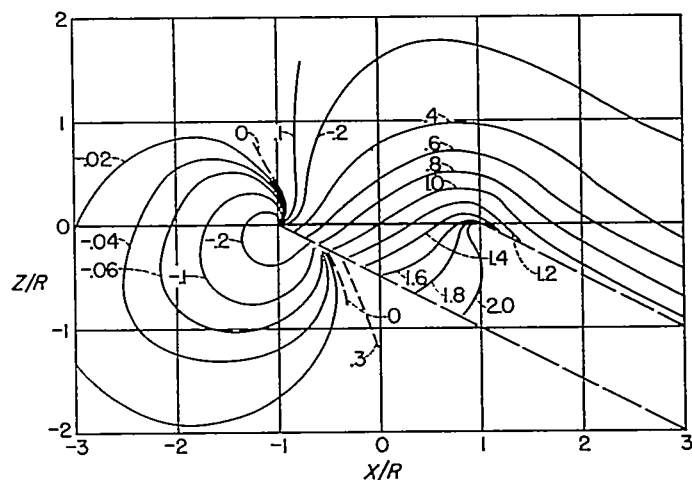


FIGURE 11.—Lines of constant value of induced velocity ratio v/v_0 in the longitudinal plane of symmetry of a rotor with a uniform disk load. $\chi = 63.43^\circ = \tan^{-1} 2$. (Reproduced from ref. 6.)

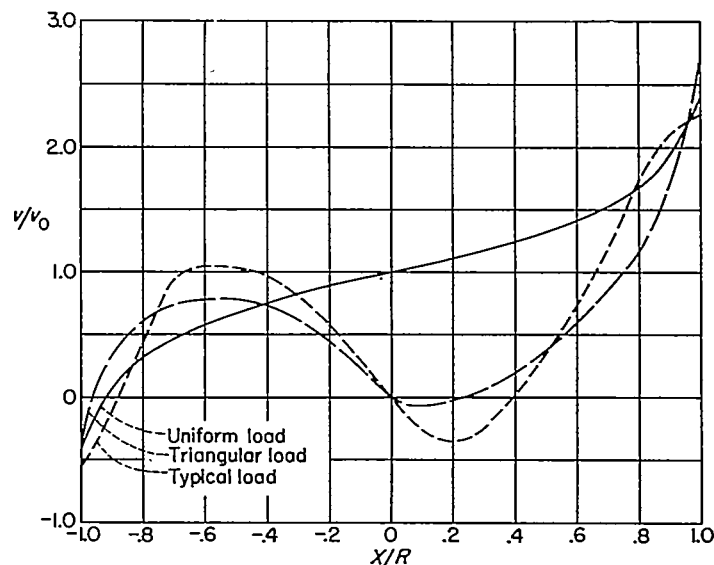


FIGURE 12.—Effect of disk load distribution on the distribution of induced velocity along X-axis. $\chi = 63.43^\circ = \tan^{-1} 2$.

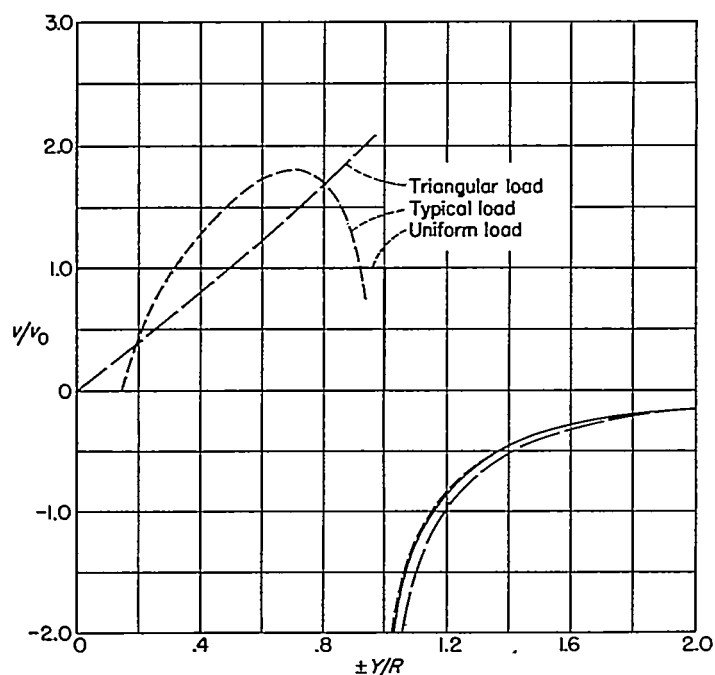


FIGURE 13.—Effect of disk load distribution on the distribution of induced velocity along the Y -axis. $\alpha = 90^\circ = \tan^{-1} \infty$.

An interesting observation can be made from figure 13. Reference 1 has shown that the uniformly loaded rotor values of induced velocity in the plane of symmetry (ref. 6) can be used as a guide to estimate the average induced velocity across a span of the order of the rotor diameter at any loca-

tion. The downwash values for the lateral axis justify this result to the same order of accuracy as the measurements of reference 1, since the average induced velocity across the span for both nonuniform disk loadings is approximately the same as that for the uniformly loaded rotor. (That is, the average value of v/v_0 is about 1.0 in all three cases.) However, the differences between the results of reference 6 and this report in the longitudinal plane of symmetry indicate the possibility of large errors if the uniformly loaded rotor flow field is used to estimate the effect of the rotor on items of appreciably different span than the rotor.

CONCLUDING REMARKS FOR PART I

A method of calculating the effect of nonuniform circularly symmetrical disk-load distributions on the normal component of the induced velocity of a lifting rotor has been presented in part I.

The induced velocity at the center of any rotor which has zero load at its center (including all practical rotors) must be zero.

Charts have been presented for the normal component of induced velocity along the major axes and for the longitudinal plane of symmetry over a wide range of skew angles for rotors with two different, nonuniform axisymmetric disk loadings that are representative of the actual loading on the rotor disk.

Rotor disk-load distribution has a large effect on the induced-velocity distribution and must be taken into account in estimating the effect of the rotor on most components of an aircraft.

II. SYMMETRY RELATIONS AND THE RELATION BETWEEN RADIAL LOAD DISTRIBUTION AND THE RADIAL DOWNWASH DISTRIBUTION IN THE WAKE

By S. Katzoff

SYMMETRY RELATIONS CONCERNING THE INDUCED VELOCITIES IN THE PLANE OF THE ROTOR

The first section of part II is concerned with the induced field of the skewed-cylinder vortex that is assumed in references 3 and 6 to represent the wake of a uniformly loaded disk. It will be shown, without reference to the detailed equations of the flow, that the induced-velocity field produced in the plane of the disk by this idealized wake possesses certain symmetries. By providing relations between the induced velocities at pairs of symmetrically located points, such symmetries are useful for checking the accuracy of calculated values such as those of reference 6. They also provide directly the values of induced velocities along the lateral axis of the disk.

As previously mentioned, the symbol notation followed in this part of the report differs from that usually used in rotary-wing work. The present notation was used in order to retain the usual complex-variable symbols in two-dimensional flow analyses and also to avoid a confusing multiplicity of subscripts. The reader should note in particular that the normal component of induced velocity w is positive upward in the following material.

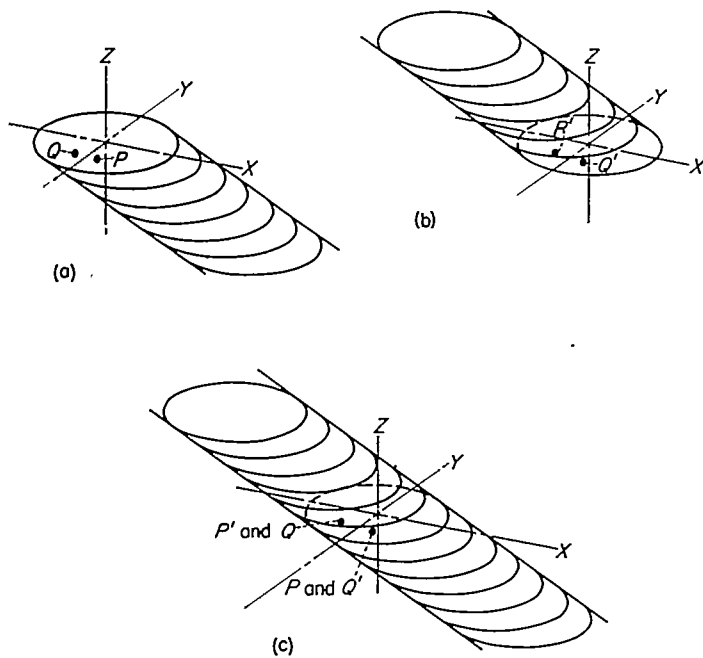
POINTS ON THE ROTOR DISK

In figure 14 (a) consider a pair of points on the rotor disk, such as P and Q , that have the same lateral location and are symmetrically located with respect to the lateral axis. That is, if P is at point $(x, y, 0)$, then Q is at point $(-x, y, 0)$. Let the three components of the induced velocity at P be (u_1, v_1, w_1) and at Q be (u_2, v_2, w_2) , where the third component is generally the only component of interest.

Now consider the entire diagram rotated 180° about the Y -axis so that it appears as in figure 14 (b). Points P and Q thereby move to points P' and Q' , where the induced velocities are, respectively, $(-u_1, v_1, -w_1)$ and $(-u_2, v_2, -w_2)$.

If figure 14 (b), with the vorticity reversed, is fitted to figure 14 (a), so that P' falls on Q and Q' falls on P , the two semi-infinite vortex cylinders form a single continuous infinite vortex cylinder (fig. 14 (c)). The induced velocity at the left-hand point (P' and Q) is $(u_1 + u_2, v_2 - v_1, w_1 + w_2)$, and at the right-hand point (Q' and P) it is $(u_1 + u_2, v_1 - v_2, w_1 + w_2)$. The two velocities are thus equal except for the lateral components, which are equal and opposite.

In appendix A of reference 3, however, it was shown that



(a) Rotor and wake. (b) Wake rotated 180° about Y-axis.
(c) Vortex cylinders shown in figures 14 (a) and (b) fitted together to form an infinite cylinder.

FIGURE 14.—Symmetrically located points in the rotor disk.

the induced velocity within this infinite skewed helix is uniform and has no lateral component. The first result of the present discussion, then, is that $v_2 - v_1 = v_1 - v_2 = 0$ or $v_1 = v_2$.

The second result is that the sums $u_1 + u_2$ and $w_1 + w_2$ are uniform. That is, the sums of the two longitudinal components and of the two vertical components are the same for all pairs of symmetrically located points on the disk (as P and Q), and are equal to the longitudinal and vertical components of the induced velocity within the infinitely long helix. In the nomenclature of reference 3,

$$u_1 + u_2 = v_x'$$

$$w_1 + w_2 = v_z'$$

Furthermore, if points P and Q are on the lateral (Y) axis, so that they coincide ($u_1 = u_2$ and $w_1 = w_2$),

$$u_1 = \frac{v_x'}{2}$$

$$w_1 = \frac{v_z'}{2}$$

That is, the longitudinal and vertical components of the induced velocity are constant all along the lateral diameter of the disk and are equal to the values at the center of the disk.

POINTS OUTSIDE THE ROTOR DISK

If points P and Q are beyond the edge of the rotor disk (fig. 15), the discussion proceeds as before except that it no longer follows that $u_1 + u_2$ and $w_1 + w_2$ are constant or that $v_1 - v_2$ is zero. The reason, of course, is that after superposition of the two semi-infinite skewed vortex cylinders

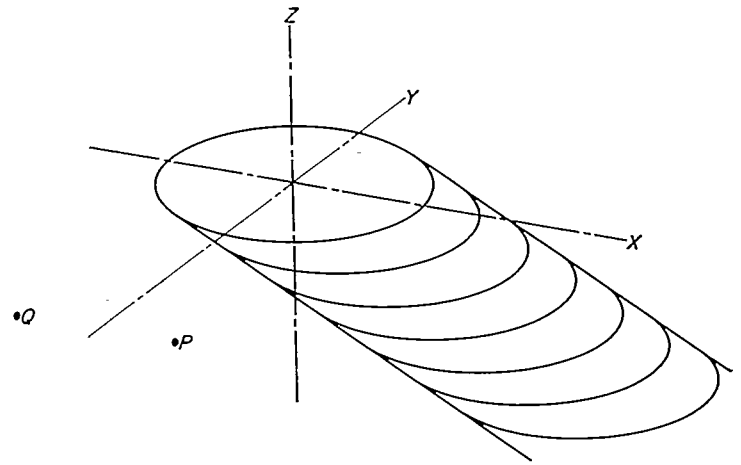


FIGURE 15.—Symmetrically located points in the plane of, but outside, the rotor disk.

the points lie outside the infinite elliptic cylinder instead of inside of it. The combined flow field outside the cylinder is not uniform but is the same as if the cylinder had a solid boundary. That is, the combined induced flow is two-dimensional in planes normal to the cylinder axis and can be computed as that induced by an elliptic cylinder in a steady flow of velocity $V \cos \chi$ normal to its axis. The streamlines of the induced flow in the normal plane are sketched in figure 16. The components u' and v' of the induced flow in this plane are related to $u_1 + u_2$, $v_1 - v_2$, and $w_1 + w_2$ as follows:

$$u_1 + u_2 = v' \cos \chi$$

$$w_1 + w_2 = v' \sin \chi$$

$$v_1 - v_2 = u' \text{ at the right-hand point } (P \text{ and } Q')$$

For points along the lateral axis,

$$u_1 + u_2 = 2u_1 = v' \cos \chi$$

$$w_1 + w_2 = 2w_1 = v' \sin \chi$$

$$v_1 - v_2 = 0$$

Thus, for points along the lateral axis, u_1 and w_1 can be determined directly from the known two-dimensional flow about the ellipse.

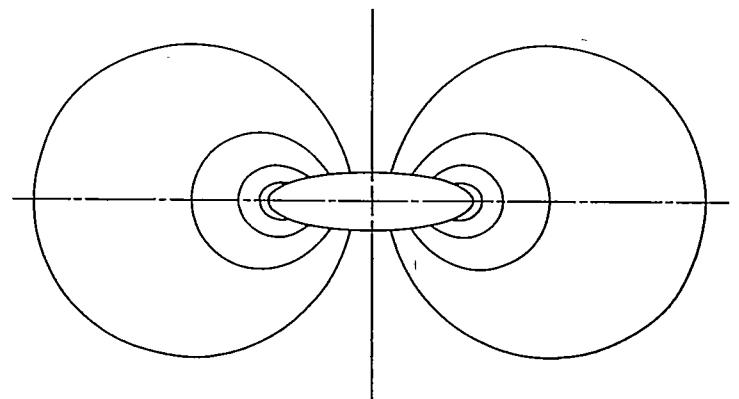


FIGURE 16.—Two-dimensional crossflow around an ellipse.

In order to facilitate application of these results, a few remarks concerning the calculation of v' are contained in the next section.

FLOW ABOUT AN ELLIPTIC CYLINDER

Consider (fig. 16) the flow induced by an elliptic cylinder of semimajor axis a and semiminor axis b in a cross flow of velocity $V \cos \chi$. Let the plane of the figure be the z' plane, where $z' = x' + iy'$ (the x' axis is parallel to the y -axis, or the lateral axis of the disk).

The flow is probably best treated in elliptic coordinates, related to the rectangular coordinates by

$$z' = c \cosh \zeta$$

where

$$\zeta = \xi + i\eta$$

$$c = \sqrt{a^2 - b^2}$$

The complex flow function w for the field induced by the ellipse in the steady cross flow of velocity $V \cos \chi$ is

$$w = (V \cos \chi) ia \sqrt{\frac{a+b}{a-b}} e^{-\zeta}$$

(The equation may be obtained, for example, from the equation on page 256 in ref. 8 by setting U equal to zero, replacing V by $V \cos \chi$, and omitting the free-stream flow function.) Then the complex velocity is

$$\begin{aligned} \frac{dw}{dz'} = \frac{dw/d\zeta}{dz'/d\zeta} &= -(V \cos \chi) ia \sqrt{\frac{a+b}{a-b}} \frac{e^{-\zeta}}{c \sinh \zeta} \\ &= -(V \cos \chi) \frac{ia}{c} \sqrt{\frac{a+b}{a-b}} \frac{2}{e^{2\zeta} - 1} \end{aligned}$$

Setting $\zeta = \xi + i\eta$ and multiplying numerator and denominator by the conjugate of the denominator ($e^{2(\xi-i\eta)} - 1$) leads to the following expression for v' , the negative of the imaginary part of $\frac{dw}{dz'}$:

$$v' = 2(V \cos \chi) \frac{a}{c} \sqrt{\frac{a+b}{a-b}} \frac{e^{2\xi} \cos 2\eta - 1}{e^{4\xi} - 2e^{2\xi} \cos 2\eta + 1}$$

or

$$v' = (V \cos \chi) \frac{a(a+b)}{c^2} \frac{\cos 2\eta - e^{-2\xi}}{\cosh 2\xi - \cos 2\eta}$$

Since $x' + iy' = c \cosh (\xi + i\eta)$, the values of ξ and η corresponding to any point (x', y') in the field of the ellipse are obtainable directly from tables of complex hyperbolic functions (ref. 9). (In using these tables, note that η is given in units of $\pi/2$. It will be observed that $\cos \chi = \frac{b}{a}$ and $\sin \chi = \frac{c}{a}$.)

The points P , P' , Q , and Q' will be noted to lie in a plane which intersects the plane of the ellipse at the angle χ . However, because of the two-dimensional character of the flow, the desired values of the induced velocities at a point

(x, y) in the plane of the rotor may be found at the point $(x' = y, y' = x \cos \chi)$ in the plane of the ellipse.

RELATIONS BETWEEN THE RADIAL VARIATION OF DISK LOADING AND THE RADIAL VARIATION OF DOWNWASH VELOCITY WITHIN THE DOWNSTREAM WAKE

In figure 13 the computed lateral variation of the downwash angle across the lateral axis was shown to resemble the assumed radial distribution of disk loading. An effort was therefore made to determine whether the resemblance was mainly fortuitous or whether a general theoretical basis existed for it.

It was found possible to show that, for the far wake, the downwash velocity along any radius is proportional to r^n if the disk loading is also proportional to r^n . The proportionality factor, however, depends on n (in addition to the azimuth). Accordingly, if the radial disk loading is represented by a power series, the downwash velocity along any radius is also represented by a power series where, however, the respective coefficients of the two series are not proportional. Thus the radial loading is not, in general, exactly proportional to the radial downwash-velocity distribution, although the two may be nearly proportional if the radial loading is approximately proportional to, say, r or r^2 .

In the following development the simplest case, $\chi = 0^\circ$, will be discussed first. The general case, $0^\circ < \chi < 90^\circ$, will then be discussed. Finally, the particular case $\chi = 90^\circ$, which is related to linearized lifting-surface theory, will be discussed.

THE CASE $\chi = 0^\circ$

The problem is simple for the circular wake, $\chi = 0^\circ$. Consider first the uniformly loaded disk, which produces a single helical vortex lying along a circular cylinder. In the far wake the downwash within the cylinder is uniform, and there is no downwash at all outside the cylinder. For an infinitesimal annulus (dr) of disk loading, the wake is then two concentric circular cylinders having equal and opposite vorticity and separated by dr . The downwash between the two cylinders is uniform and proportional to the annulus loading. The downwash everywhere else is zero. If the disk loading is made up of a continuous distribution of such annuli, the downwash directly downstream of each annulus is thus determined only by that annulus loading and is not affected by the loading of any other annulus. For this case, then, the radial variation of downwash velocity is proportional to the radial variation of disk loading. Restricting the theorem to loadings that are proportional to r^n is unnecessary for this case, which will be recognized as merely the well-known propeller blade-element theory applied to the far wake instead of to the disk itself where the induced velocities are only half as much.

THE CASE $0^\circ < \chi < 90^\circ$

As previously mentioned, the uniformly loaded disk produces an ultimate wake in the form of an inclined elliptic

cylinder, within which the induced flow is uniform and outside of which the induced flow is that due to an elliptic cylinder in the cross-flow component of the free-stream flow. If the loading is circularly symmetrical but not uniform, the wake consists of a corresponding distribution of concentric similar elliptic cylinders, and the present problem is concerned with the superposition of their induced flow fields.

If each cylinder induced only the uniform internal velocity field and induced no external field, the argument would proceed just as for the case $\chi=0^\circ$, and it would follow immediately that the radial distribution of induced velocity is proportional to the radial loading distribution. In order to prove the theorem, then, it is only necessary to show that the total of the *external* fields of the distribution of cylinders will, along any radius, also have velocities proportional to r^n , if the loading is proportional to r^n .

Consider the flow induced by an ellipse of given shape and unit size (say unit semimajor axis) moving at velocity $V \cos \chi$. As previously indicated, the induced velocity component parallel to the minor axis (parallel to the direction of motion of the ellipse) is the component of interest. Along any direction θ from the origin, this induced velocity is a function of the radial distance ρ .

If, while the shape remains constant, the linear dimensions of the ellipse are changed by the factor k , the velocity originally existing at radial distance ρ will be found at radial distance $k\rho$ along the given direction θ . For the general ellipse of size k , then, the velocity component v' can be expressed as

$$v' = f(\theta, k/\rho)$$

The velocity induced by an increment in size, or annulus, corresponding to dk is

$$\frac{\partial v'}{\partial k} dk = f'(\theta, k/\rho) \frac{dk}{\rho}$$

where f' denotes the derivative with respect to k/ρ . If each incremental velocity is weighted by the factor k^n , the total velocity is

$$\int_{k=0}^K k^n f'(\theta, k/\rho) \frac{dk}{\rho} = \rho^n \int_{k/\rho=0}^K (k/\rho)^n f'(\theta, k/\rho) \frac{dk}{\rho}$$

where the upper limit K is that value of k for which the ellipse just touches the specified point (ρ, θ) . (As previously noted, the present discussion concerns only the contributions of those annuli for which the point is located externally.) Changing the variable of integration from k to k/ρ changes the form of the preceding expression to

$$\rho^n \int_{k/\rho=0}^{K/\rho} (k/\rho)^n f'(\theta, k/\rho) d(k/\rho) = \rho^n F(\theta, n)$$

since the upper limit K/ρ is now a function only of θ . Thus, the induced velocity along any radial line is proportional

to ρ^n , which was to be proved. The proportionality factor is a function of both θ and n . It will be observed that this part of the proof can apply to any shape, since the fact that the wake is elliptical was not required or used in the proof.

Performing the indicated integration in order to get the proportionality factor $F(\theta, n)$ is obviously a somewhat awkward task. Possibly the most convenient method is first to integrate by parts in order to return f' to f (that is, v' , for which an expression was previously presented), and then determine the resulting integral numerically. For either the lateral or longitudinal axis, however, the calculation may be performed without excessive difficulty. The method will be here indicated.

For the lateral axis ($\eta=0$), the previously derived expression for v' reduces to

$$v' = (V \cos \chi) \frac{a}{c} \sqrt{\frac{a+b}{a-b}} \frac{x' - \sqrt{x'^2 - c^2}}{\sqrt{x'^2 - c^2}}$$

so that the problem is reduced to evaluating

$$\int_{c=0}^{c=x'} c^n \frac{\partial}{\partial c} \left(\frac{x' - \sqrt{x'^2 - c^2}}{\sqrt{x'^2 - c^2}} \right) dc$$

Substituting $c = x' \sin \alpha$ changes the integral to a form that can be integrated by application of items 274 and 263 of reference 10.

For the longitudinal axis $\eta = \frac{\pi}{2}$ the expression for v' reduces to

$$v' = -(V \cos \chi) \frac{a}{c} \sqrt{\frac{a+b}{a-b}} \left(\frac{\sqrt{c^2 + y'^2} - y'}{\sqrt{c^2 + y'^2}} \right)$$

so that the problem is reduced to evaluating

$$\int_{c=0}^{c=y'} c^n \frac{\partial}{\partial c} \left(\frac{\sqrt{c^2 + y'^2} - y'}{\sqrt{c^2 + y'^2}} \right) dc$$

Substituting $c = y' \tan \alpha$ changes the integral to a form that can be evaluated by application of item 274 of reference 10.

THE CASE $\chi=90^\circ$

The limiting case of the flat wake is frequently assumed for convenience in analyses pertaining to high-speed forward flight. Since the rotor and the wake are in the same plane the case is analogous to that of classical linearized wing theory, with the wing in this instance having a circular plan form and a circularly symmetrical loading.

Consider first a uniformly loaded rotor. The "span load" distribution of the disk, considered as a wing, is then elliptical, since it is merely proportional, at each spanwise station, to the "chord." As is well known, the downwash in the far wake behind an elliptically loaded wing is uniform. That

is, disregarding the rolling-up phenomenon, the flow in the vertical plane normal to the far wake is the two-dimensional flow about a horizontal straight line of span equal to the rotor diameter, moving downward with a velocity equal to

$$\frac{2C_L V}{\pi(\text{Aspect ratio})} = \frac{2C_L V}{\pi(4/\pi)} = \frac{C_L V}{2} \quad (\text{see fig. 17}). \quad \text{The complex velocity for this two-dimensional flow around the far wake is given by}$$

$$\frac{dw}{dz'} = u' - iv' = \frac{C_L V}{2} \frac{-iz'}{\sqrt{z'^2 - r^2}} + i$$

where

w complex flow function
 r semispan of wing (or radius of the rotor)
 $z' = x' + iy'$ where, in the present case ($\chi = 90^\circ$), x' is the same as lateral dimension y and y' is the same as vertical dimension z

If the radius of the uniformly loaded circular wing is increased by dr , the complex velocity in the flow field changes by

$$\frac{d}{dr} \left(\frac{dw}{dz'} \right) dr = \frac{C_L V}{2} \left[\frac{-irz'}{(z'^2 - r^2)^{3/2}} \right] dr$$

This expression thus gives the complex velocity in the far wake contributed by a wing in the form of a circular annulus of radius r and width dr , and having a lift coefficient C_L .

Now consider a circular wing on which the loading is proportional to the n th power of the radius. It is made up of annuli of variable radius r and lift coefficient given by, say, $A r^n$, where A is a constant. The total complex velocity in the far wake is found by substituting $A r^n$ for C_L in the preceding expression and integrating with respect to r between 0 and the outermost annulus, $r = R$. The complex velocity is thus

$$\int_{r=0}^R \frac{A r^n V}{2} \left[\frac{-irz'}{(z'^2 - r^2)^{3/2}} \right] dr$$

where the upper limit R is greater than $|z'|$.

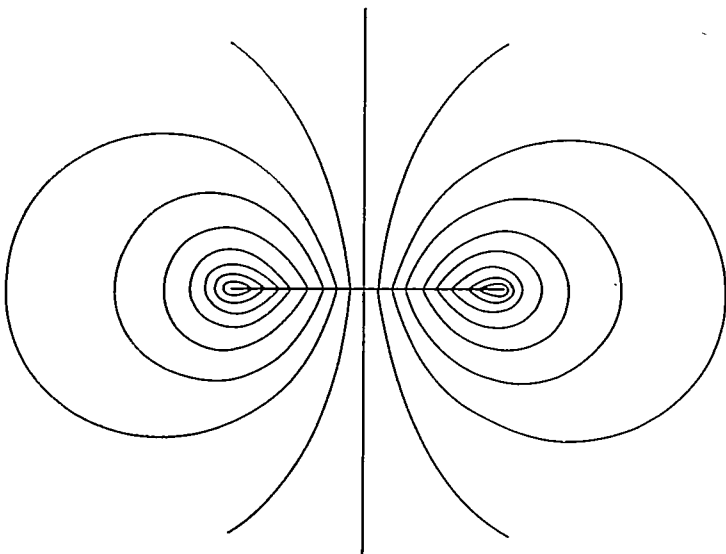


Figure 17.—Two-dimensional crossflow around a straight line.

In order to avoid a singular point in the integration, the point z' will be assumed to lie slightly above the real axis and will be allowed to approach the real axis after the integration is performed. Substituting $r = z' \sin \theta$ (where θ , in general, is complex) transforms the integral to

$$\frac{-iA z'^n V}{2} \int_{\theta=0}^{\sin^{-1} \frac{R}{z'}} \frac{\sin^{n+1} \theta d\theta}{\cos^2 \theta}$$

which can be evaluated by first applying the second form of item 274 of reference 10 and then reducing $\int \sin^{n+1} \theta d\theta$ by successive applications of item 263. Except for the last term, the integral is

$$-iA z'^n V \left[\sin^{n+1} \theta \tan \theta + \sin^n \theta \cos \theta + \frac{n}{n-1} \sin^{n-2} \theta \cos \theta + \frac{n(n-2)}{(n-1)(n-3)} \sin^{n-4} \theta \cos \theta + \dots \right]$$

Substituting the limits and letting z' become a pure real, less than R , results in a pure real; that is, all of these terms contribute nothing to the vertical-velocity component. The final term of the integral involves

$$\int_0^{\sin^{-1} \frac{R}{z'}} \sin \theta d\theta \quad \text{or} \quad \int_0^{\sin^{-1} \frac{R}{z'}} d\theta$$

depending on whether n is even or odd, respectively. For n even,

$$\begin{aligned} \text{R. P.} \int_0^{\sin^{-1} \frac{R}{z'}} \sin \theta d\theta &= \text{R. P.} (-\cos \theta) \Big|_0^{\sin^{-1} \frac{R}{z'}} \\ &= \text{R. P.} \left[-\sqrt{1 - \frac{R^2}{z'^2}} + 1 \right] \end{aligned}$$

which approaches 1 as z' approaches a pure real, $x' < R$, since the first term in the bracket approaches a pure imaginary. For n odd,

$$\text{R. P.} \int_0^{\sin^{-1} \frac{R}{z'}} d\theta = \text{R. P.} (\theta) \Big|_0^{\sin^{-1} \frac{R}{z'}}$$

which may be evaluated as follows:

Let

$$\theta = p + iq$$

then

$$\sin \theta = \sin(p + iq) = \sin p \cosh q + i \cos p \sinh q = \frac{h}{z'}$$

Since $\frac{R}{z'}$ approaches a pure real as $z' \rightarrow x'$, the imaginary term must be zero; that is, $\cos p = 0$, or $p = \pi/2$. Accordingly,

$$\text{R. P.} (\theta) \Big|_0^{\sin^{-1} \frac{R}{z'}} \rightarrow \pi/2$$

as z' approaches a pure real, $x' < R$. The final result for the downwash velocity at the real point $z' = x'$ is, for n odd,

$$\frac{A x'^n V}{2} \left[\frac{n(n-2)(n-4) \dots (1)}{(n-1)(n-3) \dots (2)} \right] \frac{\pi}{2}$$

and, for n even,

$$\frac{Ax'^n V}{2} \left[\frac{n(n-2)(n-4) \dots (2)}{(n-1)(n-3) \dots (1)} \right]$$

For $n=0$, the result is $\frac{AV}{2}$; for $n=1$, it is $\frac{Ax'\pi V}{4}$; for $n=2$, it is $\frac{1}{2}Ax'^2$; for $n=3$, it is $\frac{3}{8}\pi VAx'^3$.

CONCLUSIONS FOR PART II

A study of the symmetry relations concerning the induced velocities in the plane of a uniformly loaded rotor indicates that:

1. The sum of the induced velocities at points (x,y) and

$(-x,y)$ in the rotor disk is constant and equal to twice the induced velocity at the center.

2. The induced velocity is constant all along the lateral diameter of the disk.

3. The sum of the induced velocities at points (x,y) and $(-x,y)$ in the plane of, but outside, the rotor disk equals the induced velocity at the corresponding point near the far wake. This sum can be determined from the two-dimensional flow about the ellipse that represents the wake cross section.

A study of the relation between the radial load distribution and the radial downwash distribution in the wake of a non-uniformly loaded rotor shows that, if the disk loading varies as the n th power of the radius, the induced velocity in the far wake also varies as the n th power of the radius.

III. ANALYSIS AND COMPARISON WITH THEORY OF FLOW-FIELD MEASUREMENTS NEAR A LIFTING ROTOR IN THE LANGLEY FULL-SCALE TUNNEL

By Harry H. Heyson

APPARATUS AND TESTS

The surveys were conducted in the Langley full-scale tunnel, which is described in reference 11. The experimental apparatus used in these tests is shown in figure 18 (a).

The rotor was of the teetering or seesaw type and had untapered, untwisted blades (fig. 18 (b)) with NACA 0012 airfoil section. The rotor radius was 7.5 feet and its solidity was 0.0543. The rotor tip speed was 500 feet per second for all tests except that at $\mu=0.232$. For this test, the rotor was operated at 450 feet per second.

Two different survey rakes were used in the tests (fig. 18 (c)). A calibrated five-tube survey rake (fig. 18 (d)) was used to measure the stream pitch and yaw angles and dynamic pressures for most of the tests. This rake is fully

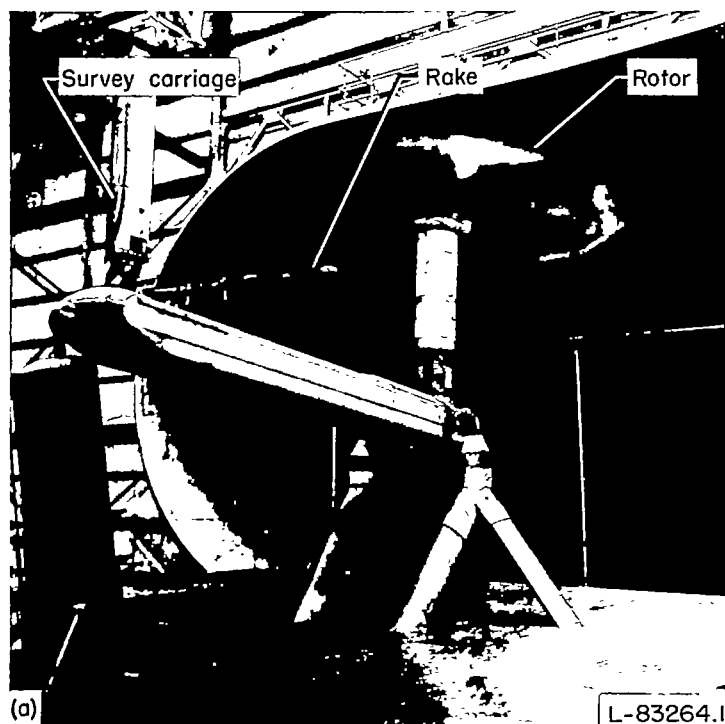
described in reference 12. In order to obtain data closer to the plane of the rotor, a calibrated pitch head (fig. 18 (e)) was used to survey points in the longitudinal plane of symmetry for one flight condition.

The procedure used in the tests was as follows: The rotor was first set approximately at a predetermined flight condition. Then, the area above, below, and behind the rotor was surveyed with the rakes. At intervals during the surveying, readings were taken of rotor thrust and drag, blade flapping and feathering motions, and tunnel dynamic pressure.

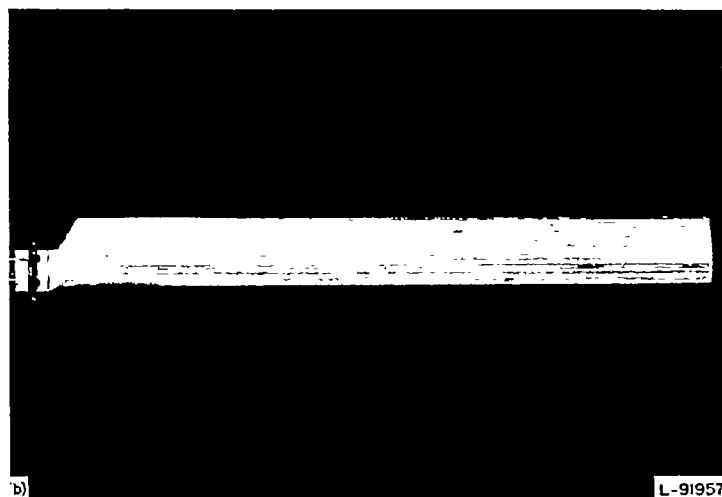
CORRECTIONS

A floor was installed in the tunnel test section for all the tests, and for this configuration the Langley full-scale tunnel has no appreciable jet-boundary correction (ref. 13).

In order to correct the measured dynamic pressures and stream angles for the flow about the supporting mechanism and for tunnel stream angle, data were taken twice at each point in space—once with and once without the rotor blades installed. The difference is considered to be characteristic



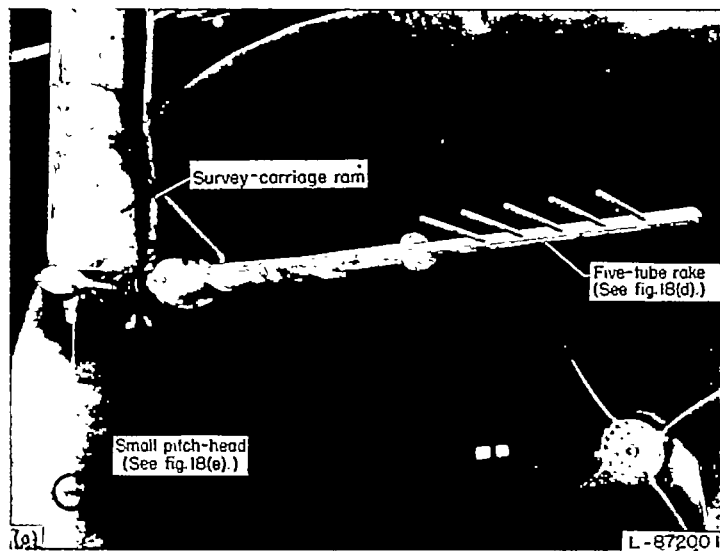
(a) Test setup looking into entrance cone of tunnel.



(b) Rotor blade.

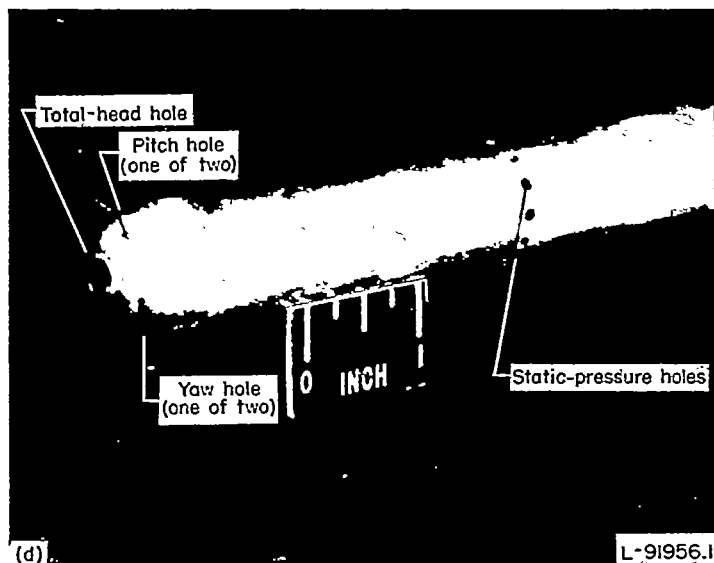
FIGURE 18.—Equipment used in surveys.

FIGURE 18.—Continued.



(c) Rakes as mounted on survey-carriage ram.

FIGURE 18.—Continued.



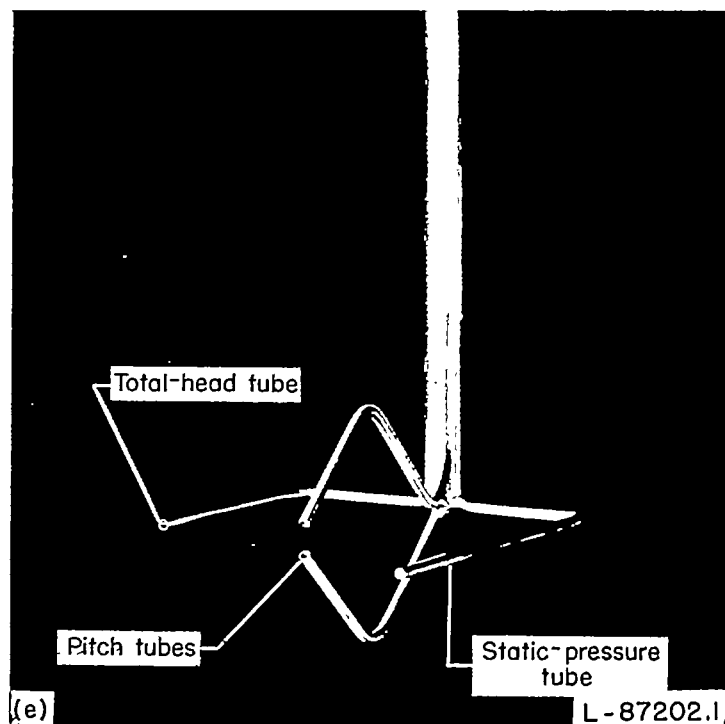
(d) End of one tube of five-tube rake.

FIGURE 18.—Continued.

of the isolated rotor. It should be noted, however, that this procedure is not adequate in regions immediately behind the rotor. Measurements made in these regions have little accuracy because of the effect of the rotor on the flow about the tower. The angle of attack of the rotor was corrected for tunnel stream angle.

PRECISION

The accuracy of the two rakes is essentially the same. Both measure dynamic pressure within 2 percent and stream angles within $\frac{1}{2}^\circ$. These figures take into account the unsteadiness of the flow and the high vibration level of the rake mount. At the lowest tip-speed ratio, additional inaccuracy is caused by the difficulty in reading the small changes of liquid height in the manometer tubes. Overall



(e) Small pitch head.

FIGURE 18.—Concluded.

accuracy in terms of the average value of the normal component of induced velocity will be a function of the rotor lift coefficient. For ease of reference, the following table gives the estimated overall accuracy for each of the flight conditions covered in this investigation:

Tip-speed ratio, μ	Accuracy, percent v_0
0.095	± 15
.139	± 10
.140	± 10
.232	± 25

The rakes used were incapable of measuring instantaneous variations of induced velocity such as might be desired for a refined blade-vibration analysis. Therefore, all data are time-averaged values. The experimental results of reference 2 indicate that instantaneous values may differ greatly from the mean values measured in these tests.

During the tests, the rotor tip speed was held constant to within 1 percent. The thrust coefficient was measured within 1 percent. The skew angle, which was computed by using the measured values of C_T and the measured blade motions in equation (29) of reference 6, should be accurate to within 1° .

The position of the rake with respect to the hub was known within 0.3 percent R . Because the rotor was of the teetering type, the only coning was due to the deflection of the blades. The tip deflection was estimated visually to be between 2 and 3 percent of the radius. The data are presented with reference to a plane parallel to the tip-path plane and passing through the teetering pin.

RESULTS AND DISCUSSION

BASIC DATA

Because of the present lack of information, both theoretical and experimental, on the induced velocities in many areas near the rotor, substantially all the basic data obtained in the investigation are presented in the appendix. In each case the rotor flight condition is identified on the figure by the skew angle χ and the tip-speed ratio μ . Table I identifies the various flight conditions more completely.

The basic-data curves are not discussed as such in this report since the more significant phenomena have already been pointed out in reference 1.

DISCUSSION OF APPLICABLE THEORY

In reference 6, Castles and De Leeuw present calculated values of the normal component of induced velocity in the longitudinal plane of symmetry and along the principal (X, Y, Z) axes of a rotor with a uniform disk loading. Part I uses the flow field of reference 6 to calculate the flow field for rotors having nonuniform but circularly symmetrical disk loadings (the specific cases calculated being rotors with a triangular disk loading and with a typical measured mean disk loading).

Additional theoretical calculations by Mangler and Squire (ref. 5) give induced-velocity information in the entire rotor disk and also for a transverse plane in the far wake. A later section discusses a method of transforming these results to correspond with the results of reference 6 and part I except for the specific disk loadings considered.

Drees (ref. 4) discusses some of the effects of a finite tip-speed ratio and presents calculations of some of these effects at selected points on the rotor disk. It should be noted that the calculated curves presented with the data are not modified for the asymmetries discussed in this reference.

COMPARISON OF MEASURED DATA WITH CALCULATED VALUES OF REFERENCE 6 AND PART I

Longitudinal plane of symmetry.—Figures 19 to 22 present the measured values of induced velocity in the longitudinal plane of symmetry as compared with the calculated values from reference 6 and part I.

For the four flight conditions, the measured data near the forward portions of the rotor fall close to the flow calculated for the rotors with zero load in the center. The existence of essentially zero induced velocity at the center of the rotor and of regions of upwash behind the center are clearly shown. Further rearward in the flow, just behind the trailing edge of the rotor ($X/R=1.07$), there is no longer any pronounced correlation between the measured and the calculated flow,

regardless of the lift distribution assumed to exist on the rotor disk. At greater distances behind the rotor ($X/R=2.07$ and 3.14), there seems to be no correlation. The physical reasons for this lack of correlation are discussed subsequently.

Longitudinal axis.—If curves are faired through the data in figures 19 to 22 and the values at $Z/R=0$ are taken from these curves, it is possible to obtain an idea of the variation of induced velocity along the longitudinal axis of the rotor. The results, plotted in figure 23, show clearly the good correlation of the nonuniformly loaded rotor calculations for the flow over the forward three-quarters of the rotor and the deviation behind that point.

Figure 24 compares the measured points of figures 23 (c) and 23 (d). These two flight conditions have very small differences in skew angles. There is, however, an appreciable difference in tip-speed ratio and lift coefficient. Actually, the calculated induced-velocity ratios for these two skew angles are virtually identical. It may be seen that, experimentally, there is very little difference between the induced velocities along the longitudinal axis for the two tip-speed ratios. This fact is as assumed in references 3 and 6.

Lateral axis.—The basic data may be cross-plotted in the same manner to obtain the induced-velocity distribution along the lateral (Y) axis. The results of these cross plots are shown in figure 25 and are compared with the calculated distributions of reference 6 and part I. The calculated flow is symmetrical since no account is taken of dissymmetries due to the finite tip-speed ratio.

A word of caution is necessary at this point. Because of the necessity of maintaining a clearance between the survey rake and the rotor, it was not possible to obtain data much closer than 20 percent R above the rotor. (See figs. 19, 21, and 22.) The theory predicts rather large gradients of induced velocity at locations closer to the rotor than this point. In the longitudinal plane of symmetry it is possible to cross-plot the data with some confidence by comparing the trends shown well above the rotor by the theory and by the measured points. At other locations, without the theory as a guide, the accuracy of cross plots is problematical. Therefore, the following discussion of the induced-velocity distribution on the Y -axis should be regarded as being on a less firm basis than the discussion in the preceding sections.

Figure 25 indicates that the rotor does have zero induced velocity at its center. This is in agreement with the assumption that the rotor carries zero load at its center and further indicates that this fact must be used if the flow is to be calculated with any degree of accuracy.

TABLE I.—FLIGHT CONDITIONS

Tip-speed ratio, μ	Rotor wake skew angle, χ , deg	C_L	C_T	ΩR , ft/sec	Disk loading, lb/sq ft	Equivalent flat-plate area, f , sq ft	Angle of attack, α , deg
0.095	75.0	0.720	0.00320	500	1.91	2.77	-9.2
.139	85.8	.386	.00373	500	.2.18	2.34	-1.1
.140	82.3	.373	.00371	500	.2.21	2.79	-5.3
.232	83.9	.122	.00321	450	1.55	1.35	-9.5

* The seeming inconsistency between the values of rotor lift coefficient and thrust coefficient on one hand and the values of average disk load on the other was caused by a slight difference in the density of air at the different times during which the tests were run.

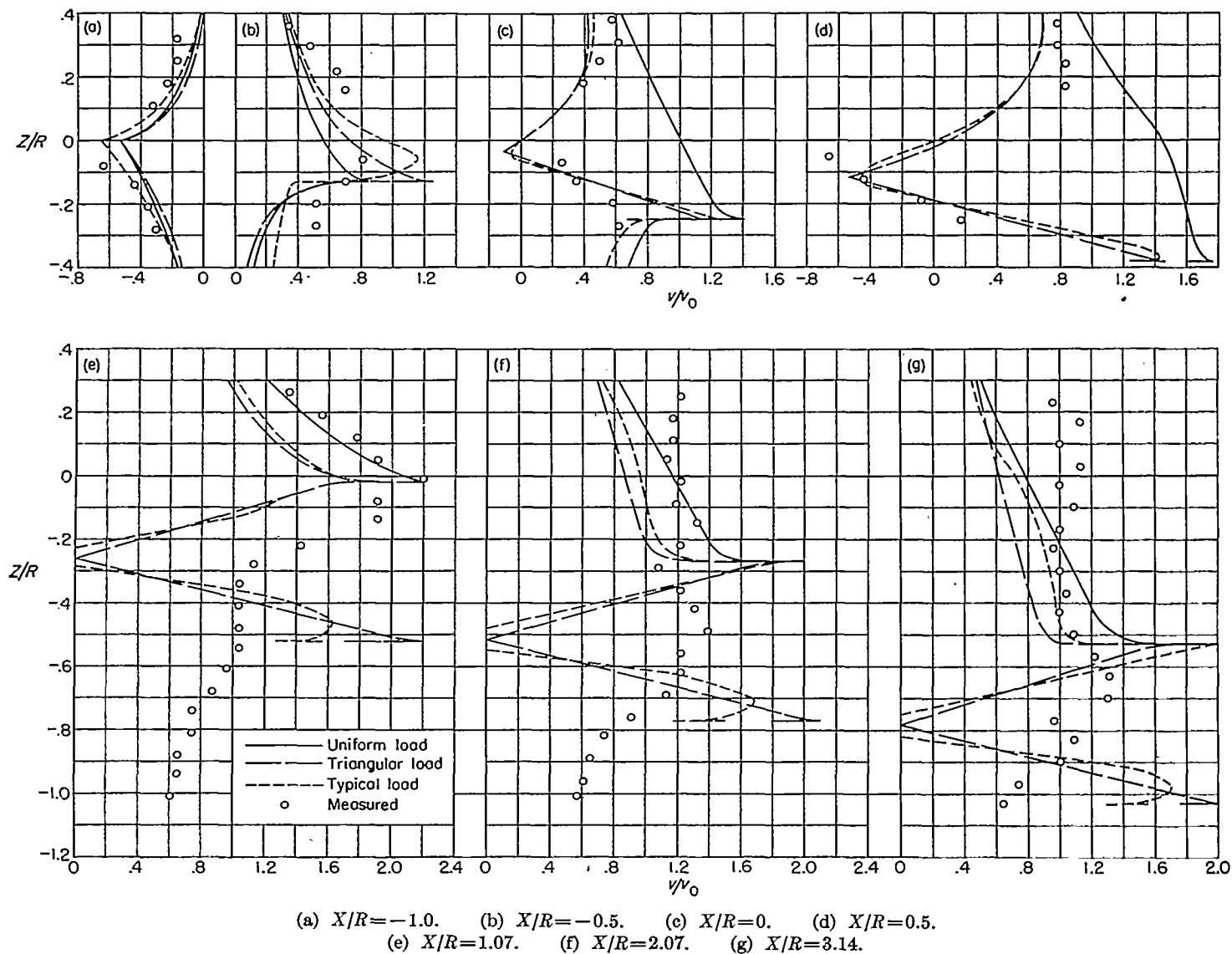


FIGURE 19.—Comparison of measured and theoretical values of induced-velocity ratio v/v_0 in longitudinal plane of symmetry. $\chi = 75.0^\circ$; $\mu = 0.005$.

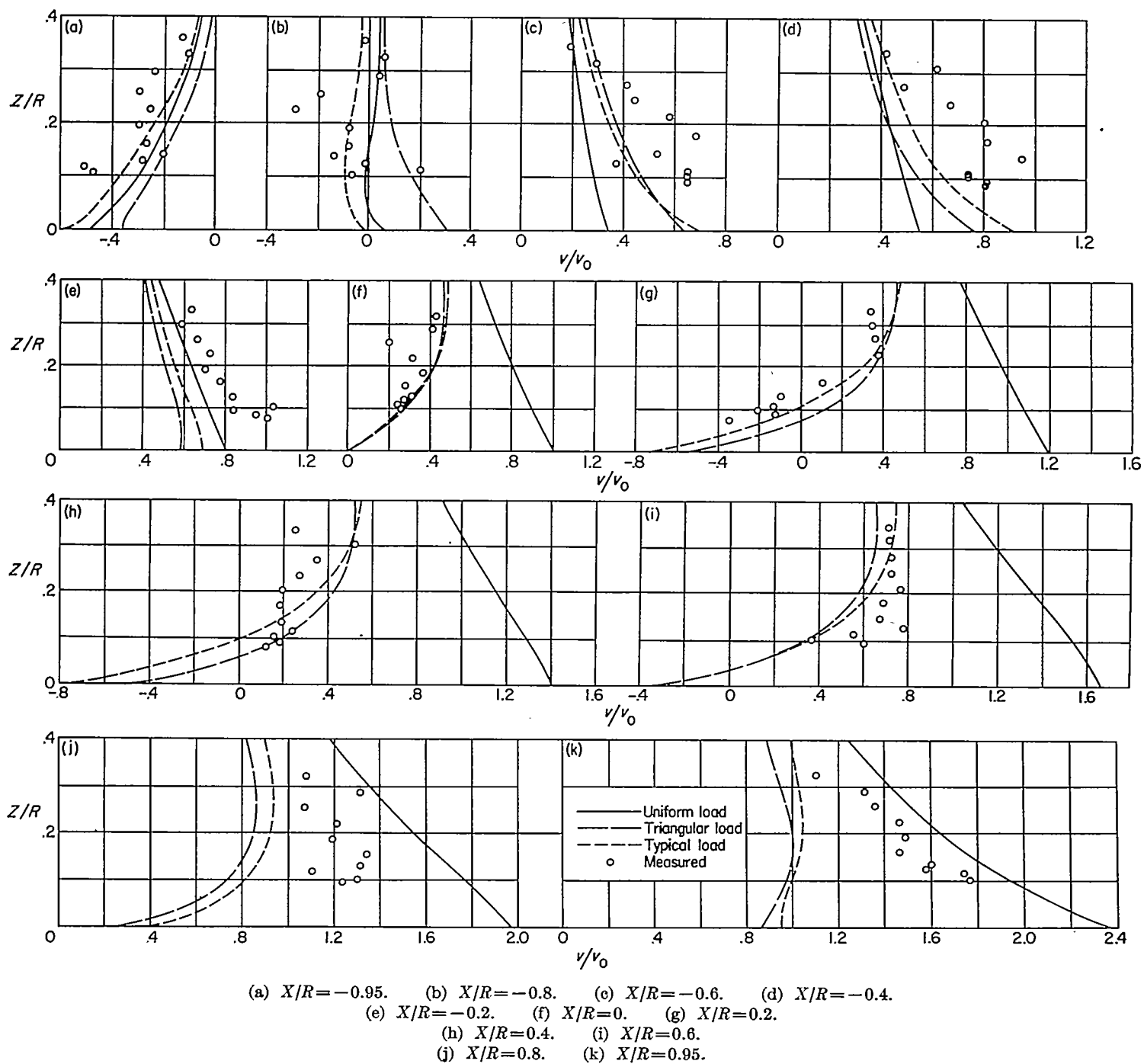


FIGURE 20.—Comparison of measured and theoretical values of induced-velocity ratio v/v_0 in longitudinal plane of symmetry. $\alpha = 85.8^\circ$; $\mu = 0.139$.

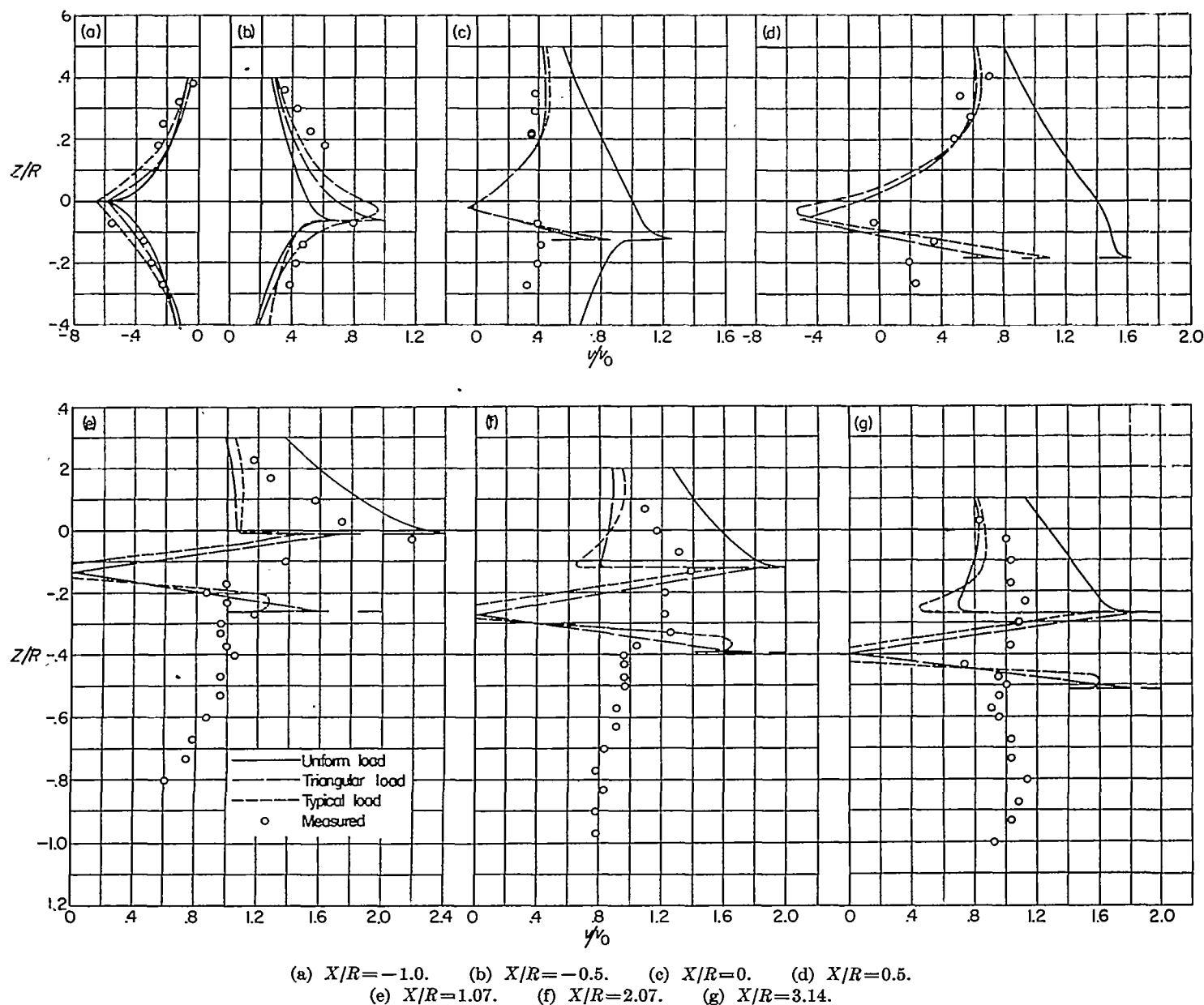


FIGURE 21.—Comparison of measured and theoretical values of induced-velocity ratio v/v_0 in longitudinal plane of symmetry. $\chi = 82.3^\circ$; $\mu = 0.140$.

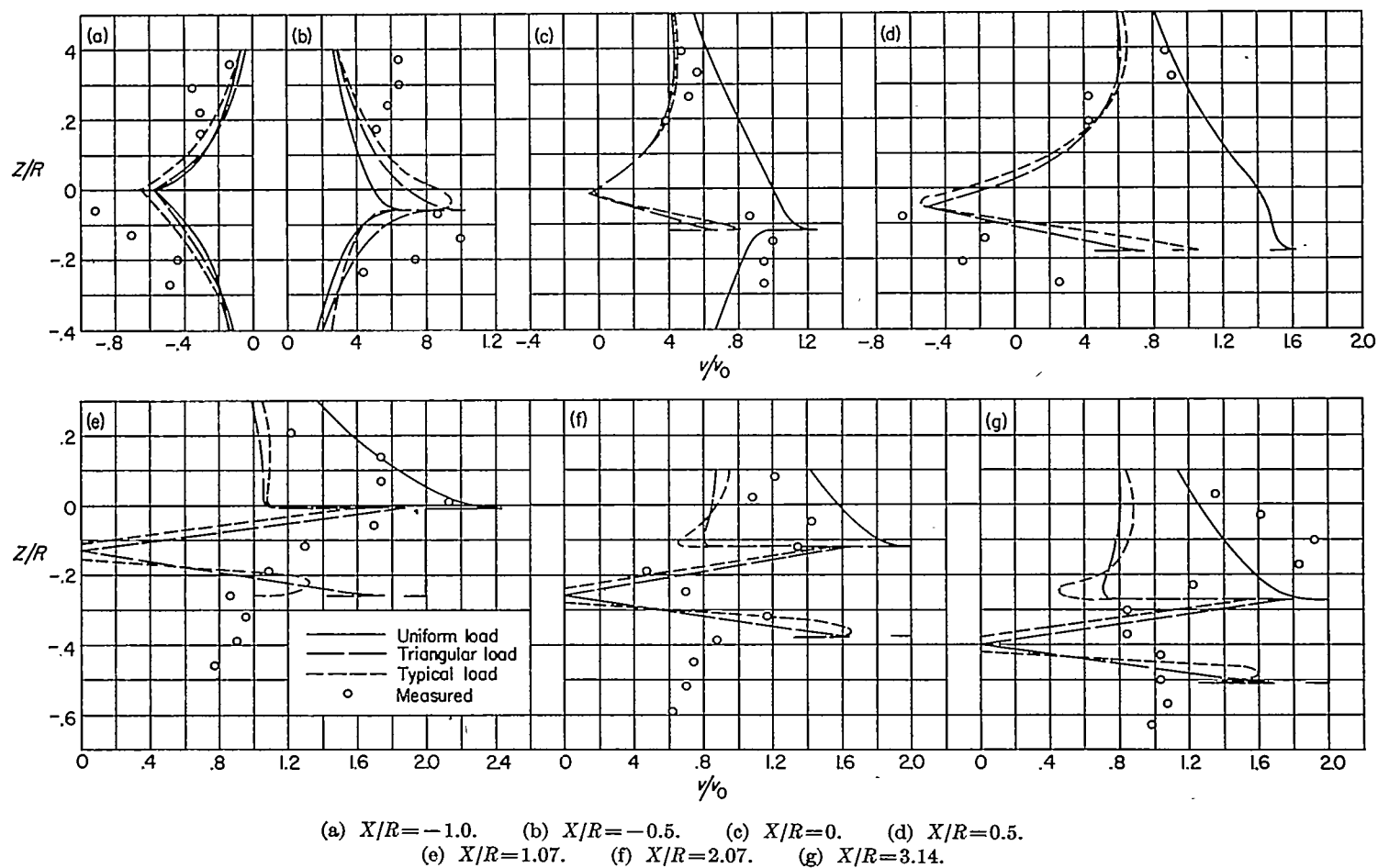
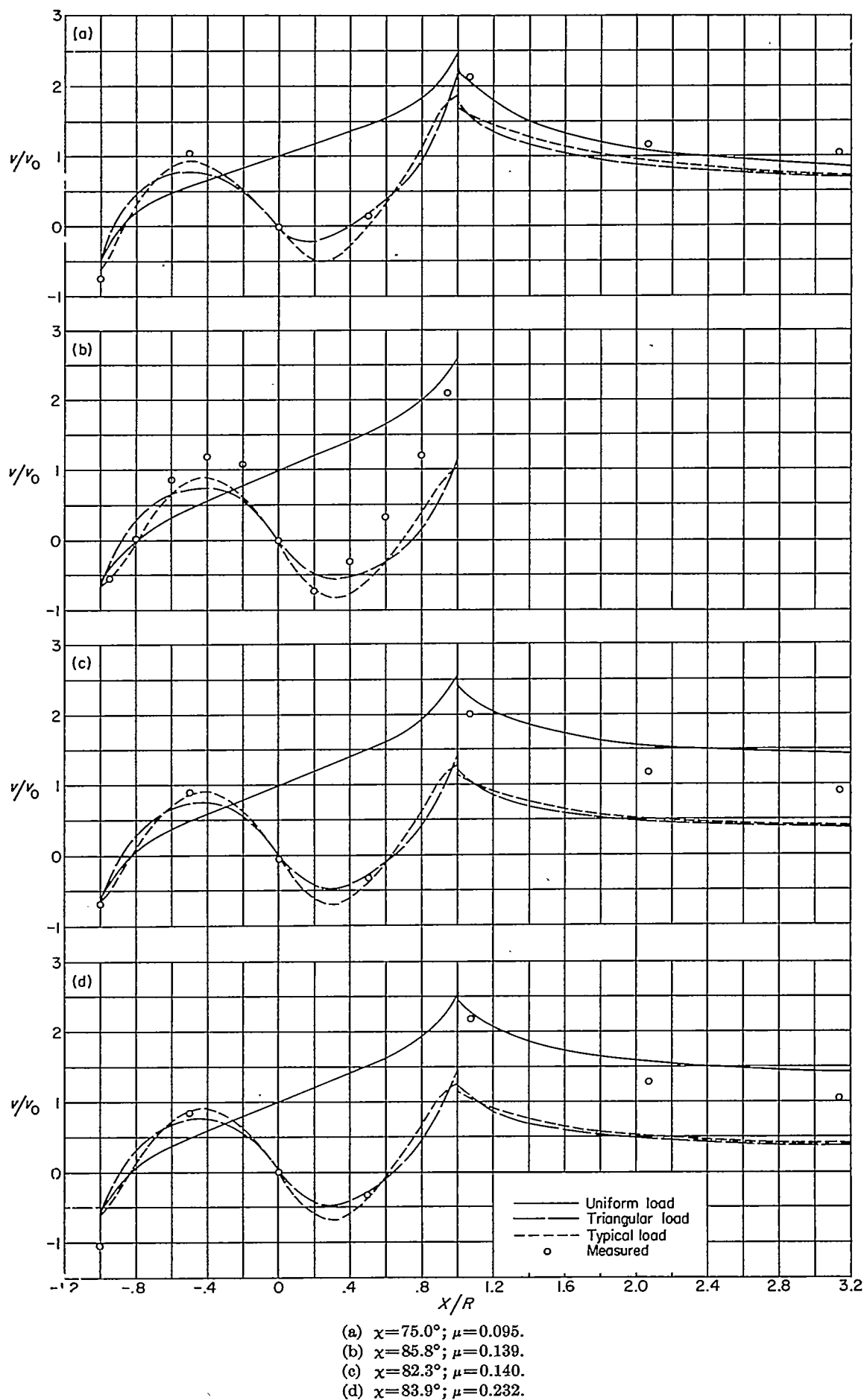


FIGURE 22.—Comparison of measured and theoretical values of induced-velocity ratio v/v_0 in longitudinal plane of symmetry. $\chi = 83.9^\circ$; $\mu = 0.232$.

FIGURE 23.—Comparison of measured and theoretical values of induced-velocity ratio v/v_0 along longitudinal center line.

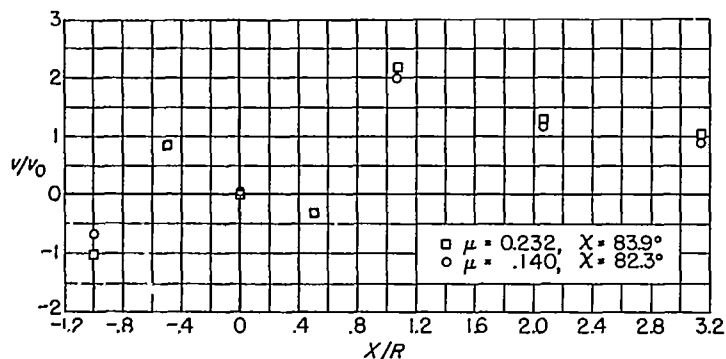
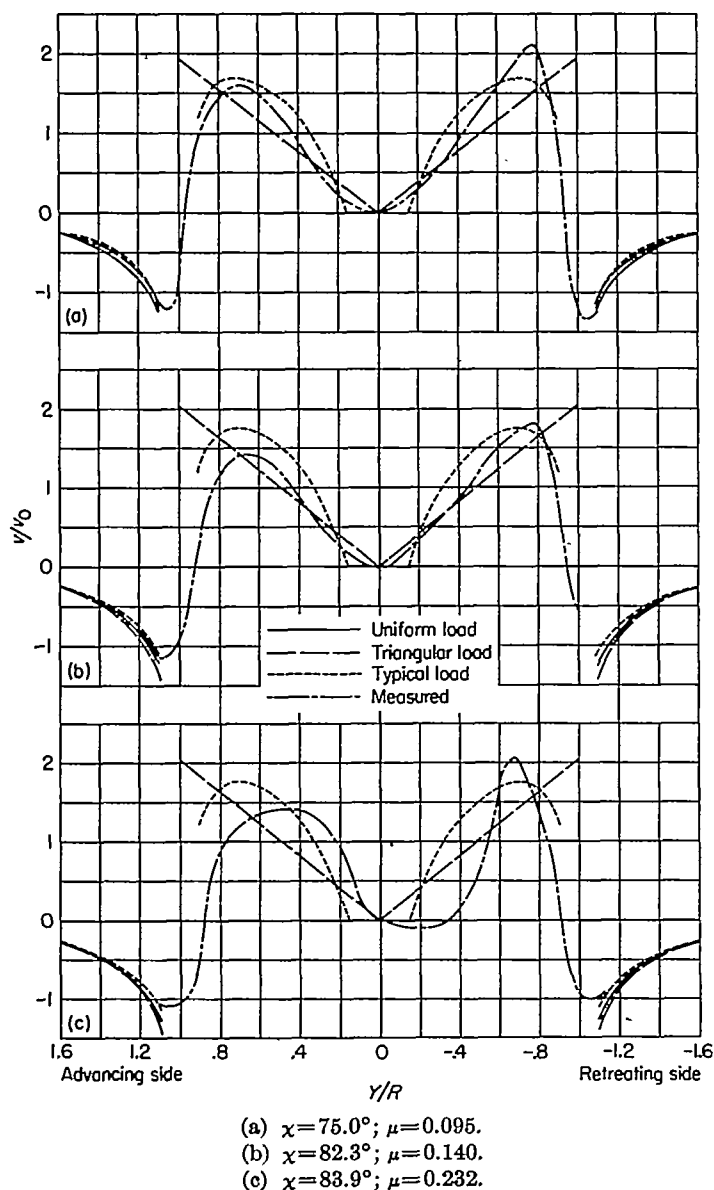


FIGURE 24.—Effect of tip-speed ratio on distribution of induced-velocity ratio v/v_0 along longitudinal center line.



- (a) $\chi = 75.0^\circ$; $\mu = 0.095$.
 (b) $\chi = 82.3^\circ$; $\mu = 0.140$.
 (c) $\chi = 83.9^\circ$; $\mu = 0.232$.

FIGURE 25.—Comparison of measured and theoretical values of induced-velocity ratio v/v_0 along lateral center line.

Figure 25 also shows that the induced-velocity peak on the retreating side is higher and further outboard than the peak on the advancing side. This result is logical when the difference in loading on the two sides of the rotor are compared. The resultant velocities at the inner portion of the blades on the retreating side are very low or even negative, whereas the corresponding velocities on the advancing side

are much higher. Therefore, the loading on the inner portion of the retreating side of the disk must be less than that on the advancing side. The outer portion of the retreating side must then carry a greater loading in order that the blade thrust moment remain essentially constant around the disk. Thus, the loading on the retreating side will peak farther outboard and at a higher value than the loading on the advancing side of the disk. This is the same trend shown by the measured induced velocities and is indicative of the very close relation between the induced velocities and the loading along this axis.

COMPARISON OF MEASURED DATA WITH CALCULATED VALUES OF REFERENCE 5

Modification of calculations for finite lift coefficient.—Mangler and Squire, in reference 5, compute the induced velocities in the rotor disk and in a transverse plane in the far wake. Their calculated results are limited to vanishingly small lift coefficients in that the trailing-vortex system leaves the rotor in the same direction and with the same velocity as the free stream.

The assumption of a finite lift coefficient alters this picture in two ways: First, the trailing-vortex system must now cross the free-stream flow and, second, there will be a change in the vortex density.

The results of reference 5 are easily modified to account for these changes and, when so modified, will correspond with the results of reference 6 and part I except for the specific disk loadings considered. The first modification is merely a rotation of the field to account for the inclination of the wake. The incidence i is then the complement of the skew angle χ . The change in vortex density, although affecting the absolute induced velocity v , will have no effect upon the induced-velocity ratio $\frac{v}{v_0} = 4 \left(\frac{v}{\sqrt{C_L}} \right)$. Therefore, the new value of v may be found by using the value of v/v_0 from reference 5 and by calculating v_0 from an equation which considers the finite lift coefficient (such as eq. (32) of ref. 6).

For the purpose of comparison with the measured data of this report, all the induced velocities of reference 5 have been modified to correspond with reference 6 in regard to both skew angle and vortex density.

Plane of the rotor.—Values of induced-velocity ratio in the plane of the rotor obtained by cross-plotting the measured data are compared with the corrected calculated values from reference 5 in figures 26 to 32. These figures are discussed only in general, since they indicate the same results as the previous comparison with reference 6 and part I. This result might be expected since the calculated results should be comparable if the same load distributions are assumed. The resemblance between the typical loading of part I and pressure distribution III of reference 5 is evident.

In general, the same extent of agreement is noticeable (see especially fig. 26 (b)); that is, the calculated flow field is close to the measured field only over the forward three-quarters of the disk.

Each figure (figs. 26 to 32) shows that the induced-velocity field for pressure distribution III is closer to the measured field on both sides of the disk than that for pressure distribution I. Since pressure distribution III represents a disk loading with zero load in the center and the

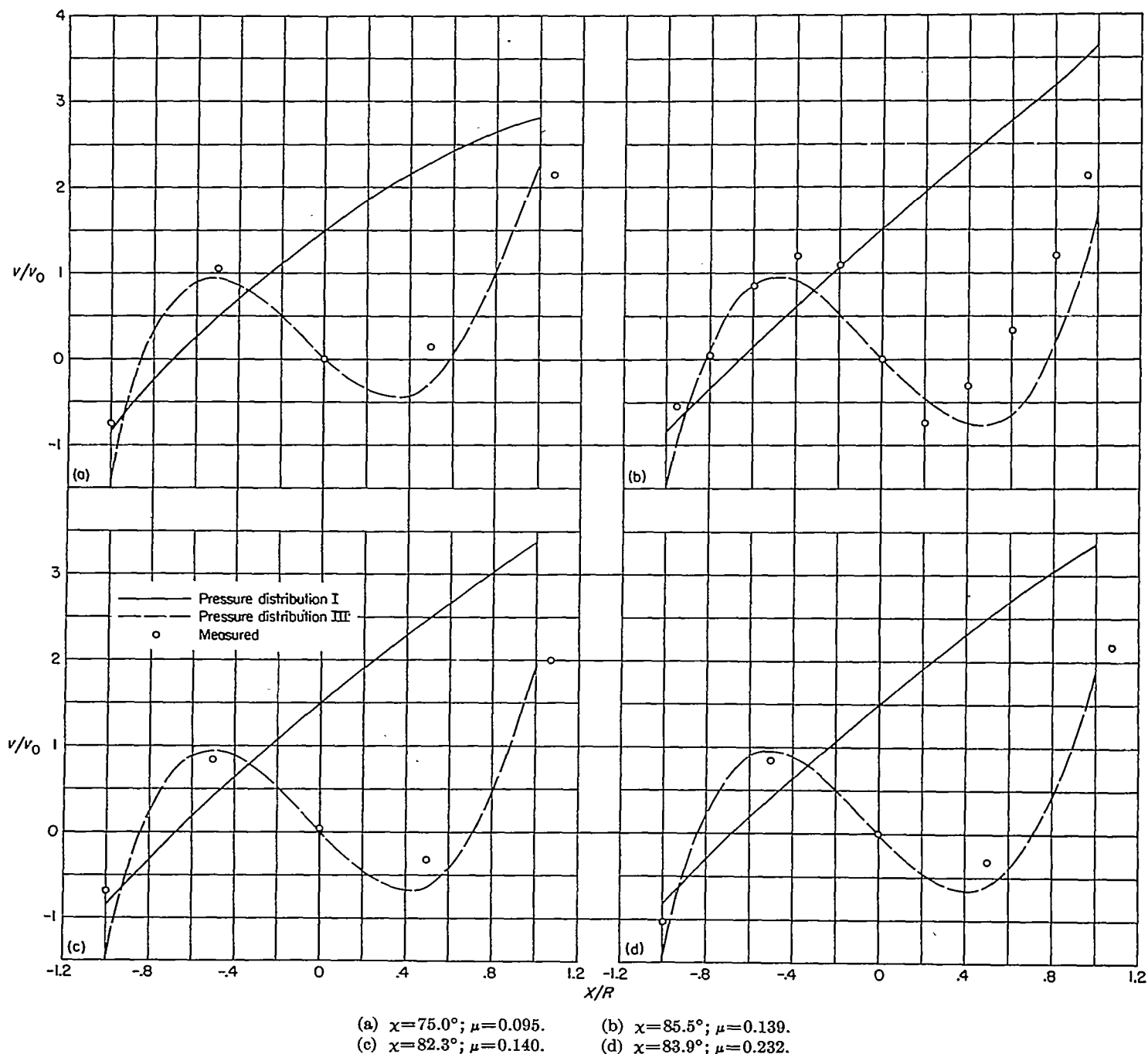


FIGURE 26.—Comparison of measured values of induced-velocity ratio v/v_0 on longitudinal center line with theory of reference 5 modified.

other distribution does not, this result is as expected.

This result does not agree with that of reference 14, which indicates that pressure distribution I should be used for calculating the induced velocities over the advancing side and pressure distribution III, over the retreating side of the rotor. This result (ref. 14) arose from measurements made at $X/R=1.5$ and, as such, is subject to error because of the discrepancy between theory and the measured data in this region. The present result is considered to be more accurate.

The values at $X/R=0.5$ (fig. 32) seem to indicate that, at this location, the error is generally somewhat larger near the outer edges of the disk. This result might be expected

since the roll-up of the trailing-vortex system would be expected to affect the outer edges of the disk sooner than the center.

Far wake.—Reference 5 also computes the induced-velocity distribution in the far wake. The computed contours of induced-velocity ratio for both pressure distributions in the far wake are compared in figures 33 to 38 with measured contours of induced velocity at $X/R=2.07$ and $X/R=3.14$ for three different flight conditions. (Notice that the rotation of the calculated flow field required to obtain correspondence with reference 6 results in a vertical displacement of the computed induced velocities.)

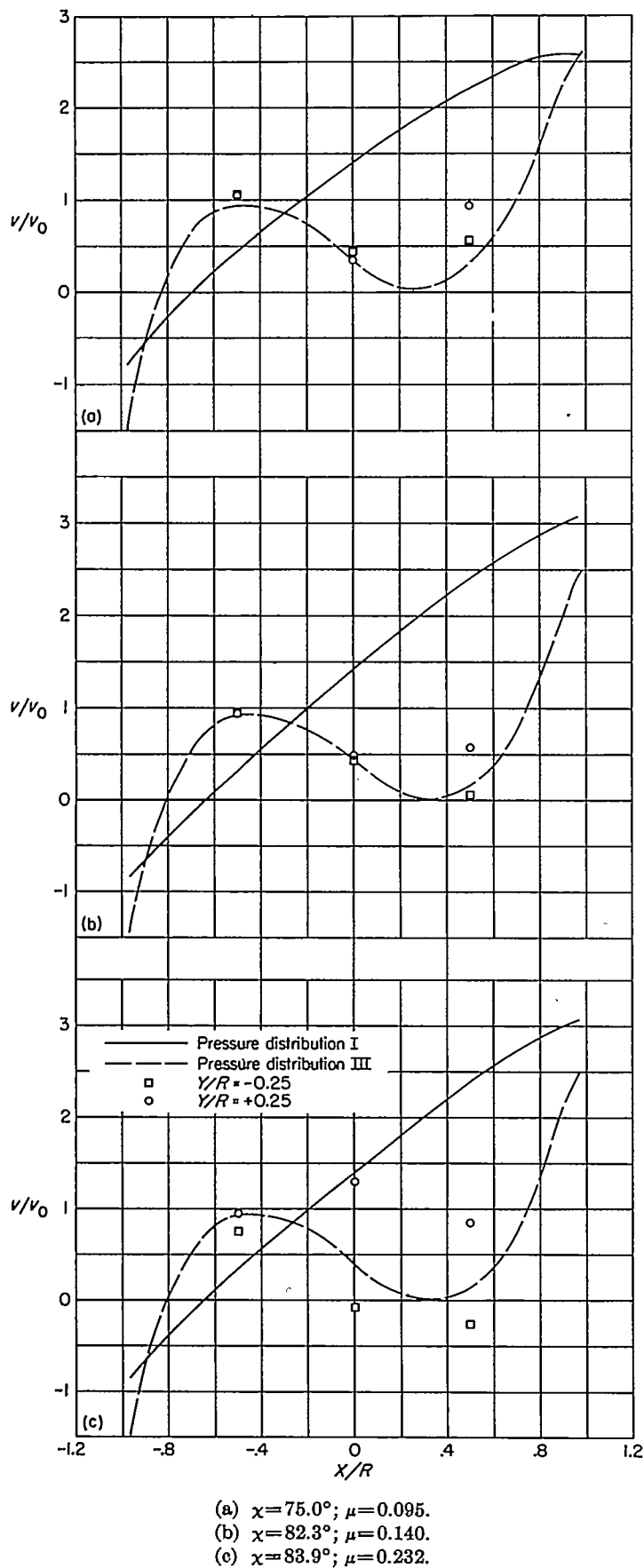


FIGURE 27.—Comparison of measured values of induced-velocity ratio v/v_0 at $Y/R = \pm 0.25$ with theory of reference 5 modified.

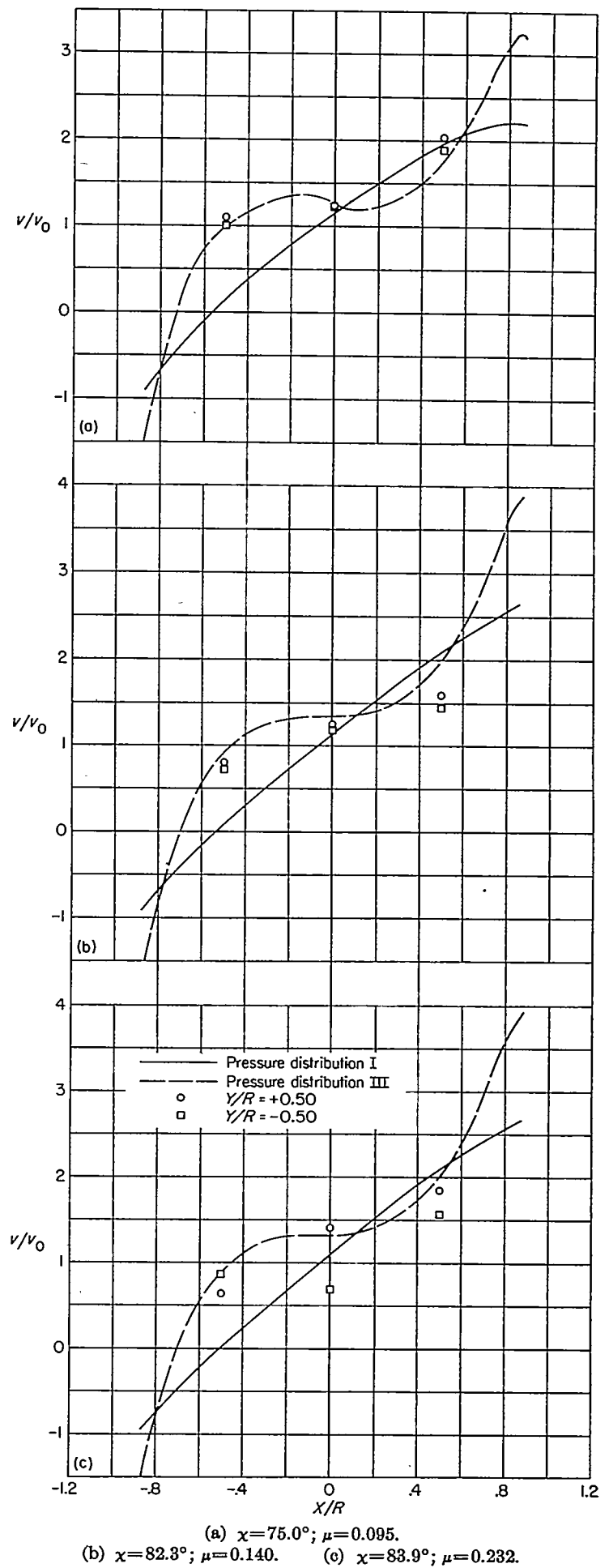
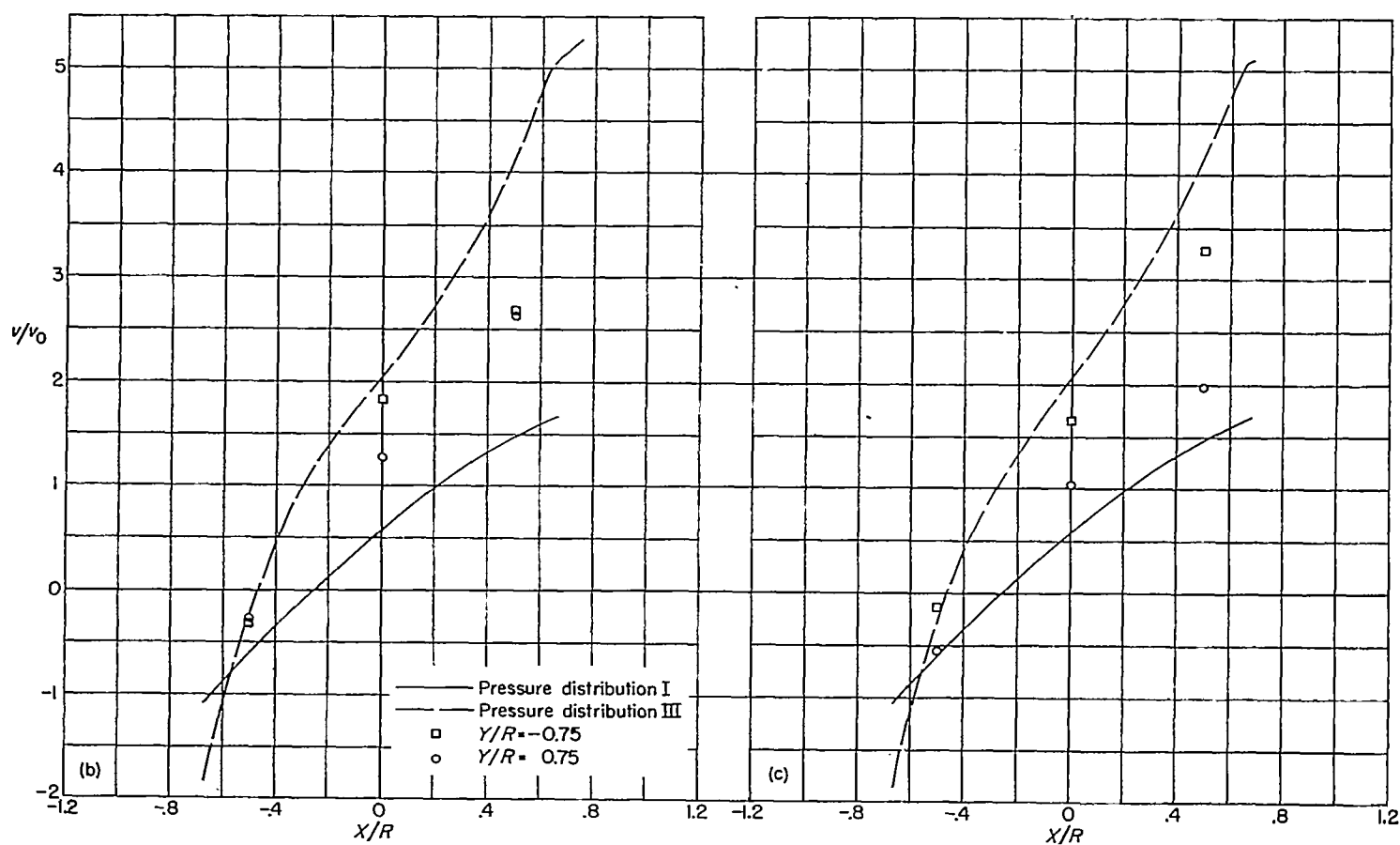
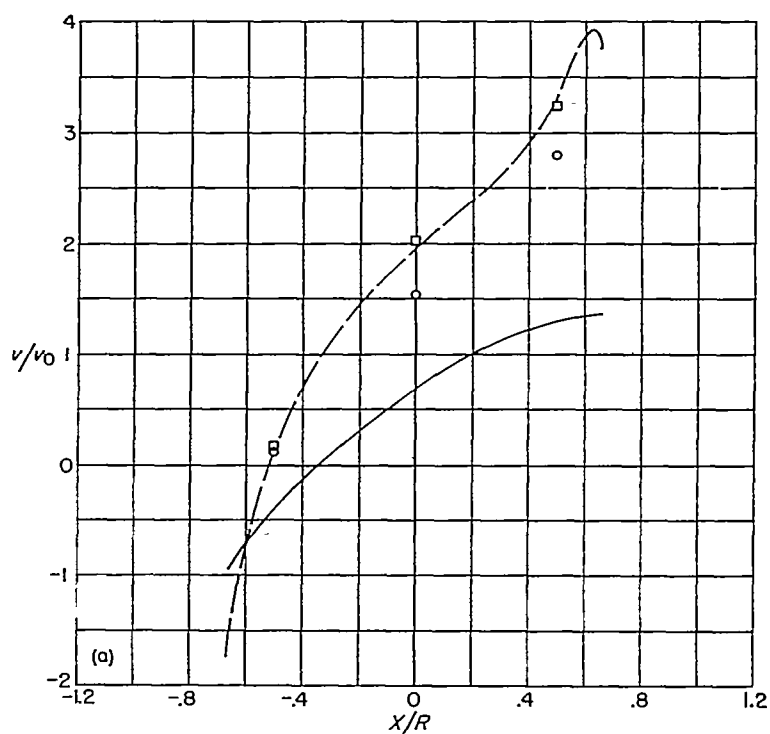


FIGURE 28.—Comparison of measured values of induced-velocity ratio v/v_0 at $Y/R = \pm 0.50$ with theory of reference 5 modified.

(a) $\chi = 75.0^\circ$; $\mu = 0.095$.(b) $\chi = 82.3^\circ$; $\mu = 0.140$.(c) $\chi = 83.9^\circ$; $\mu = 0.232$.FIGURE 29.—Comparison of measured values of induced-velocity ratio v/v_0 at $Y/R = \pm 0.75$ with theory of reference 5 modified.

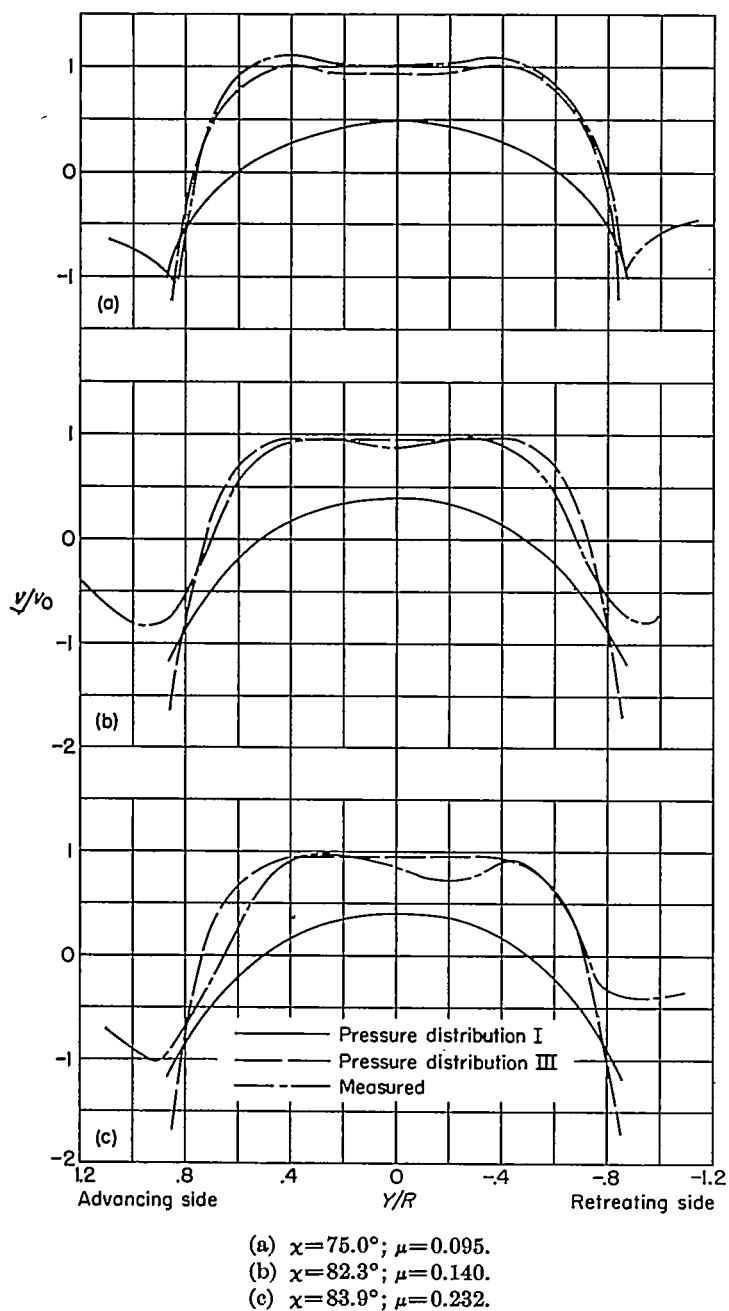


FIGURE 30.—Comparison of measured values of induced-velocity ratio v/v_0 at $X/R = -0.5$ with theory of reference 5 modified.

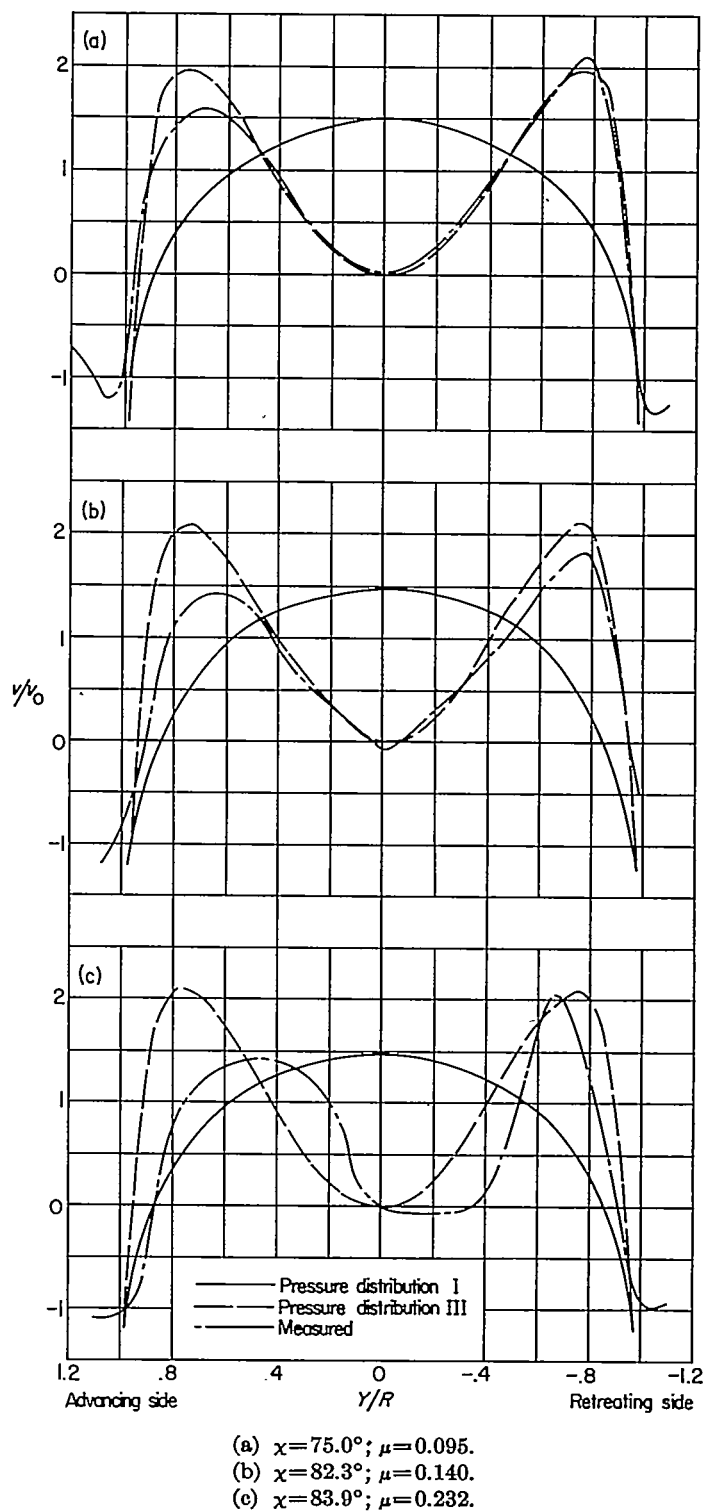


FIGURE 31.—Comparison of measured values of induced velocity ratio v/v_0 on lateral center line with theory of reference 5 modified.

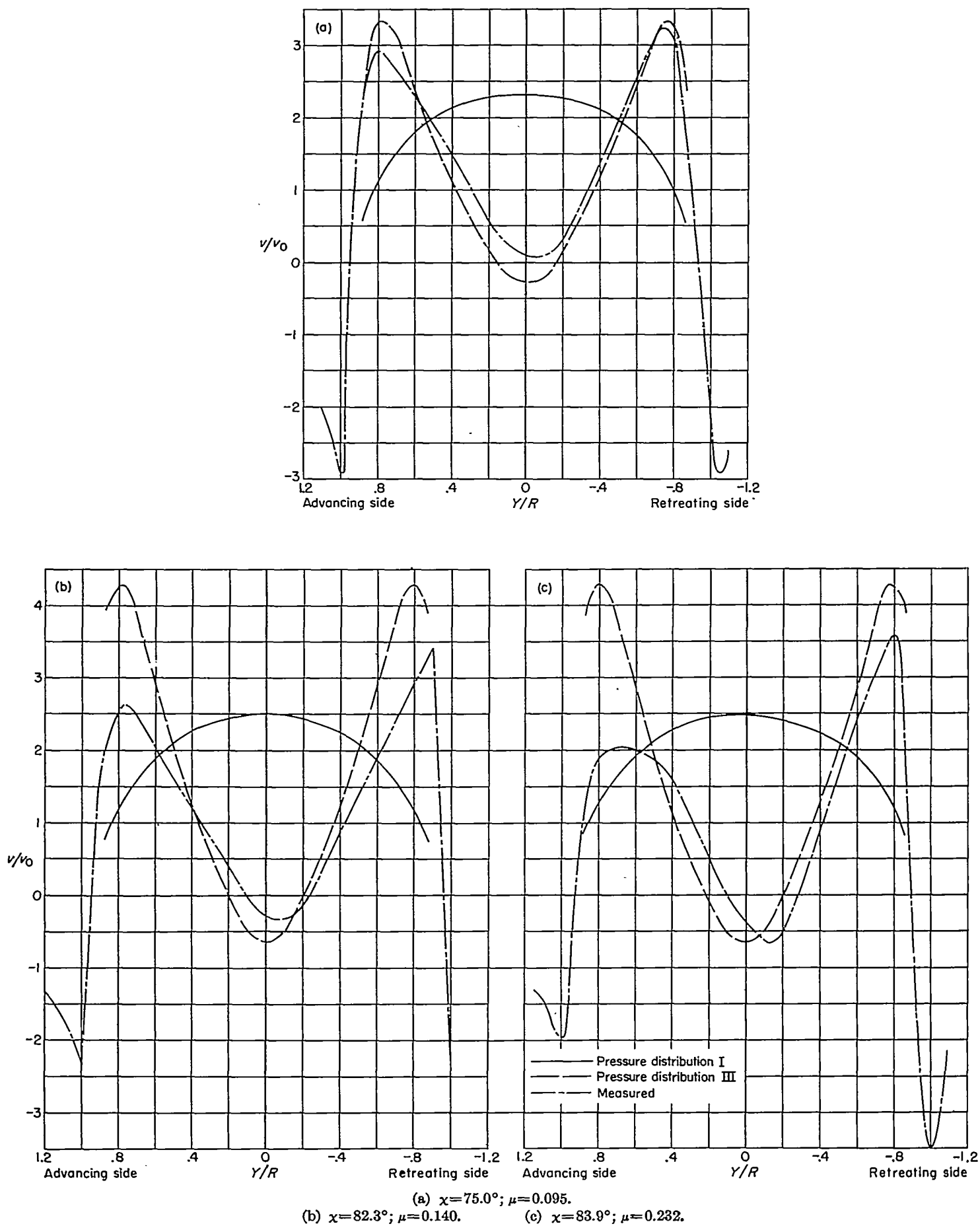
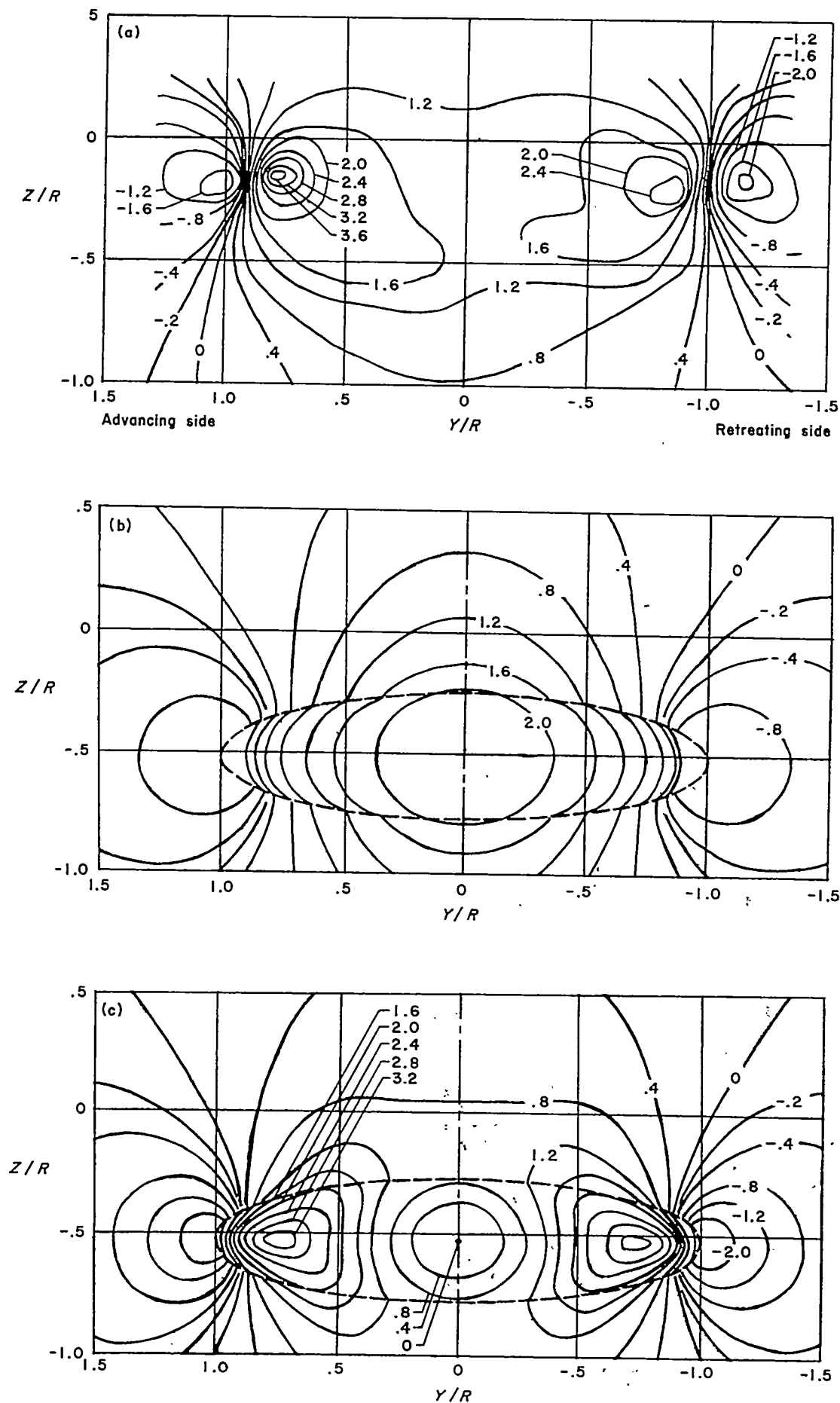


FIGURE 32.—Comparison of measured values of induced-velocity ratio v/v_0 at $X/R=0.5$ with theory of reference 5 modified.

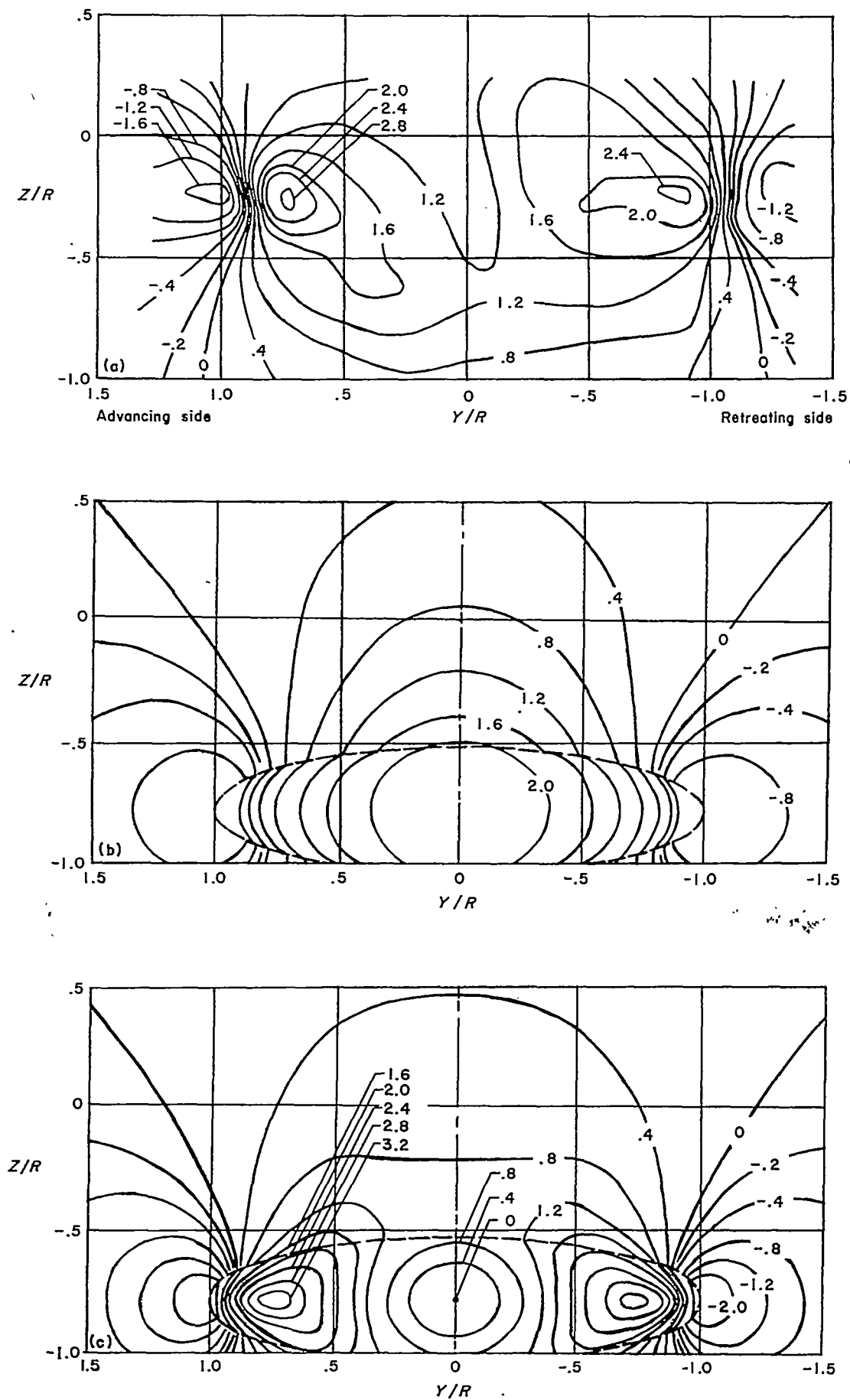


(a) Measured data.

(b) Theoretical, pressure distribution I.

(c) Theoretical, pressure distribution III.

Figure 33.—Comparison of measured values of induced-velocity ratio v/v_0 at $X/R=2.07$ with theory of reference 5 modified. $\alpha=75.0^\circ$; $\mu=0.095$.

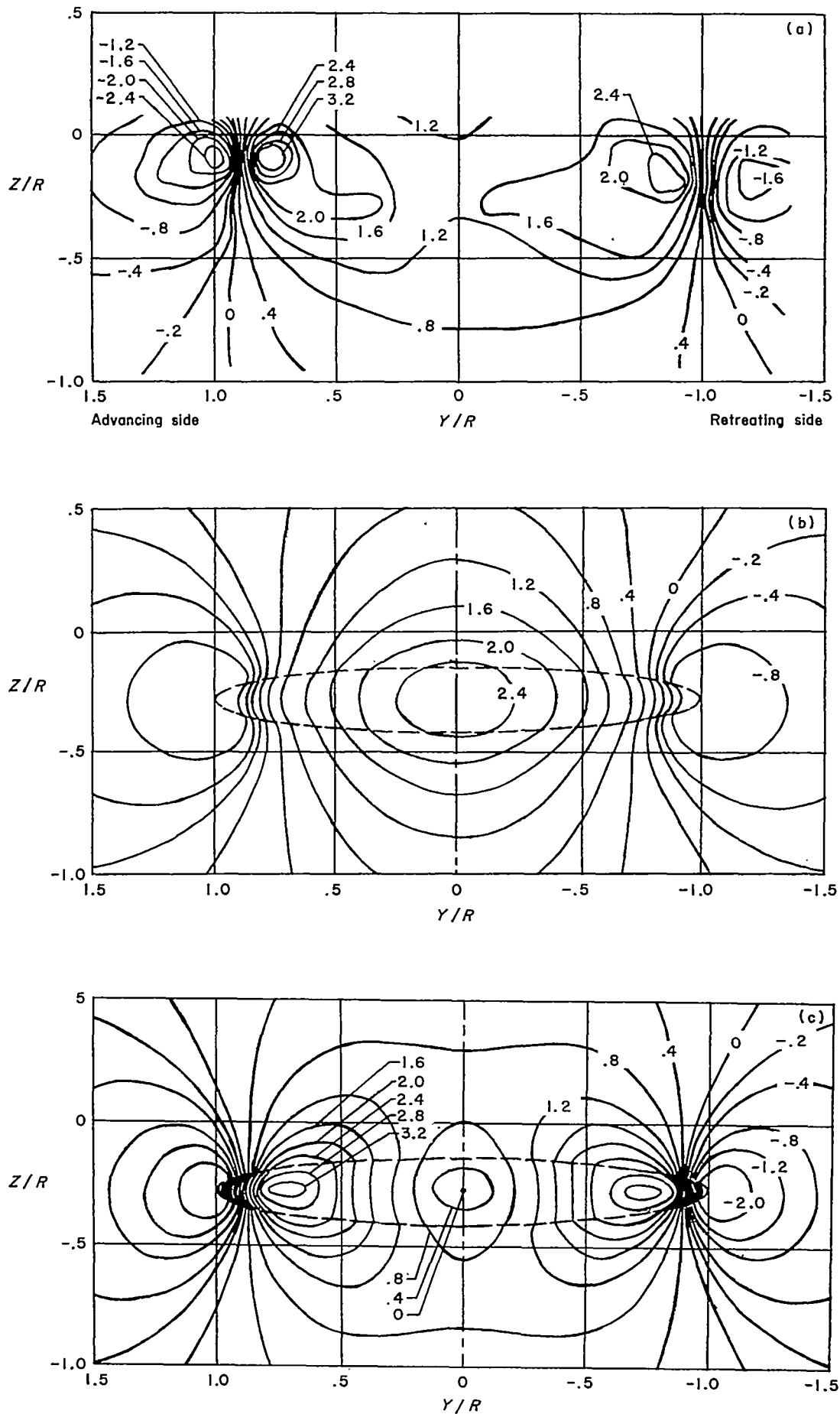


(a) Measured data.

(b) Theoretical, pressure distribution I.

(c) Theoretical, pressure distribution III.

Figure 34.—Comparison of measured values of induced-velocity ratio v/v_0 at $X/R=3.14$ with theory of reference 5 modified. $\chi=75.0^\circ$; $\mu=0.095$.



(a) Measured data.

(b) Theoretical, pressure distribution I.

(c) Theoretical, pressure distribution III.

Figure 35.—Comparison of measured values of induced-velocity ratio v/v_0 at $X/R=2.07$ with theory of reference 5 modified. $\alpha=82.3^\circ$; $\mu=0.140$.

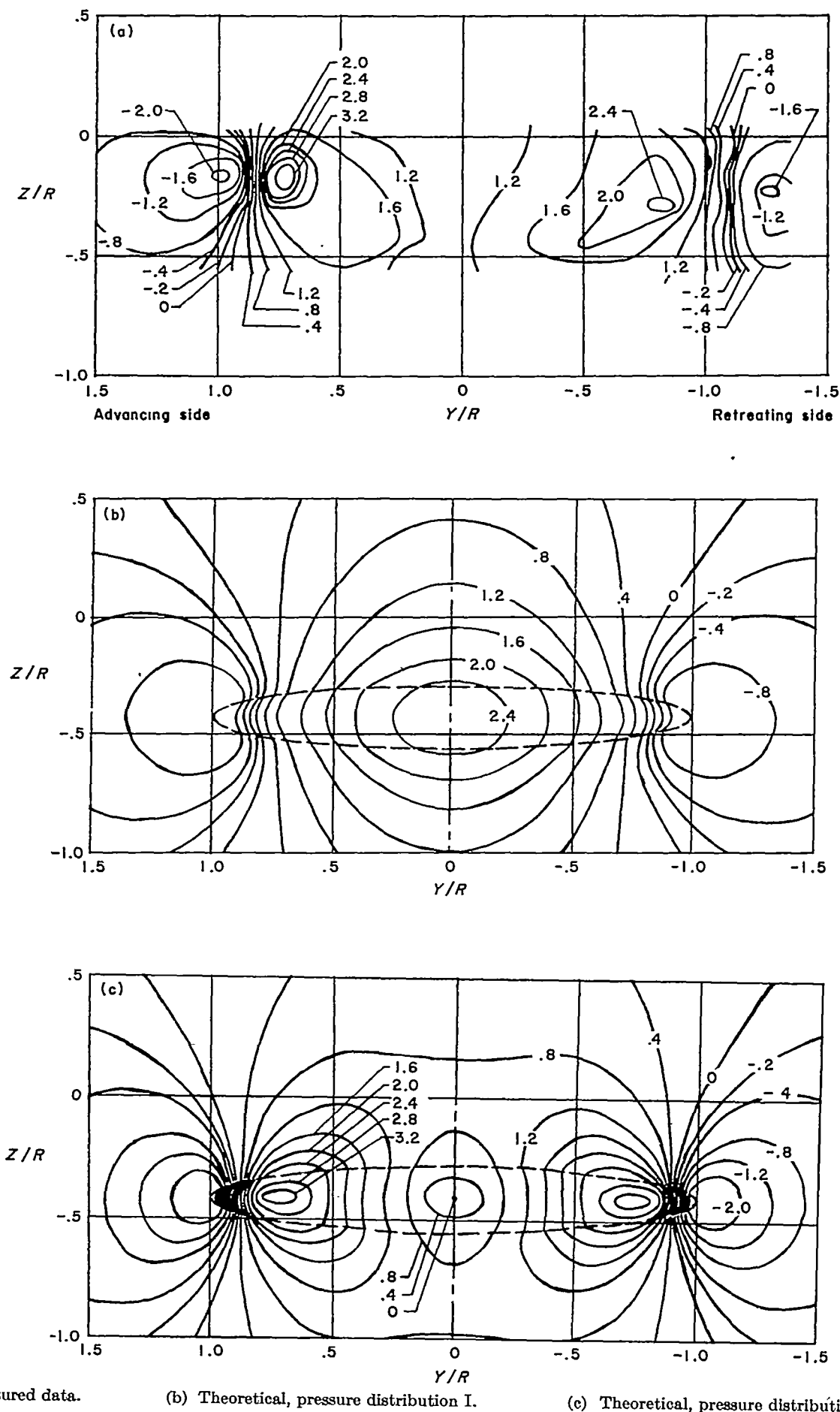
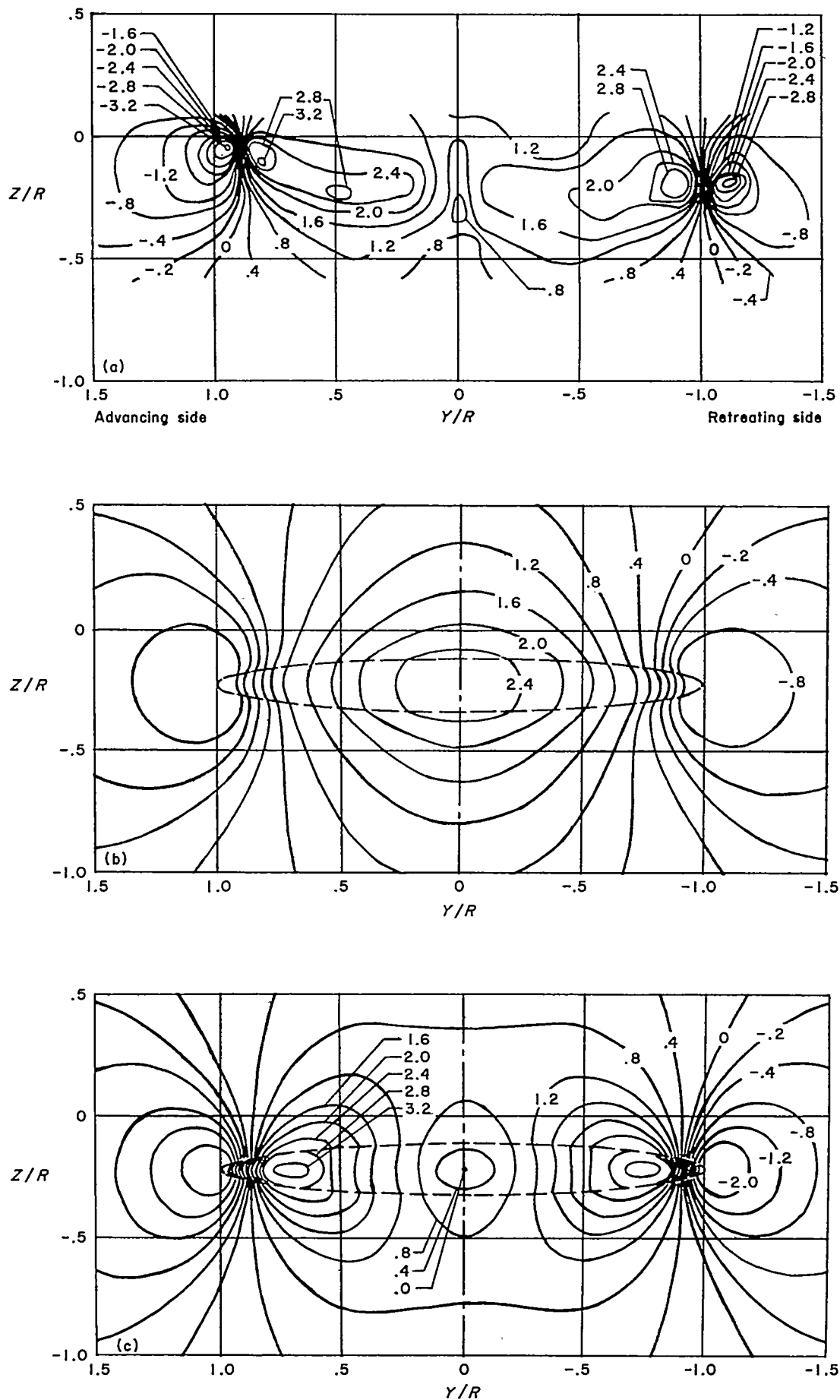


FIGURE 36.—Comparison of measured values of induced-velocity ratio v/v_0 at $X/R=3.14$ with theory of reference 5 modified. $\alpha=82.3^\circ$; $\mu=0.140$.

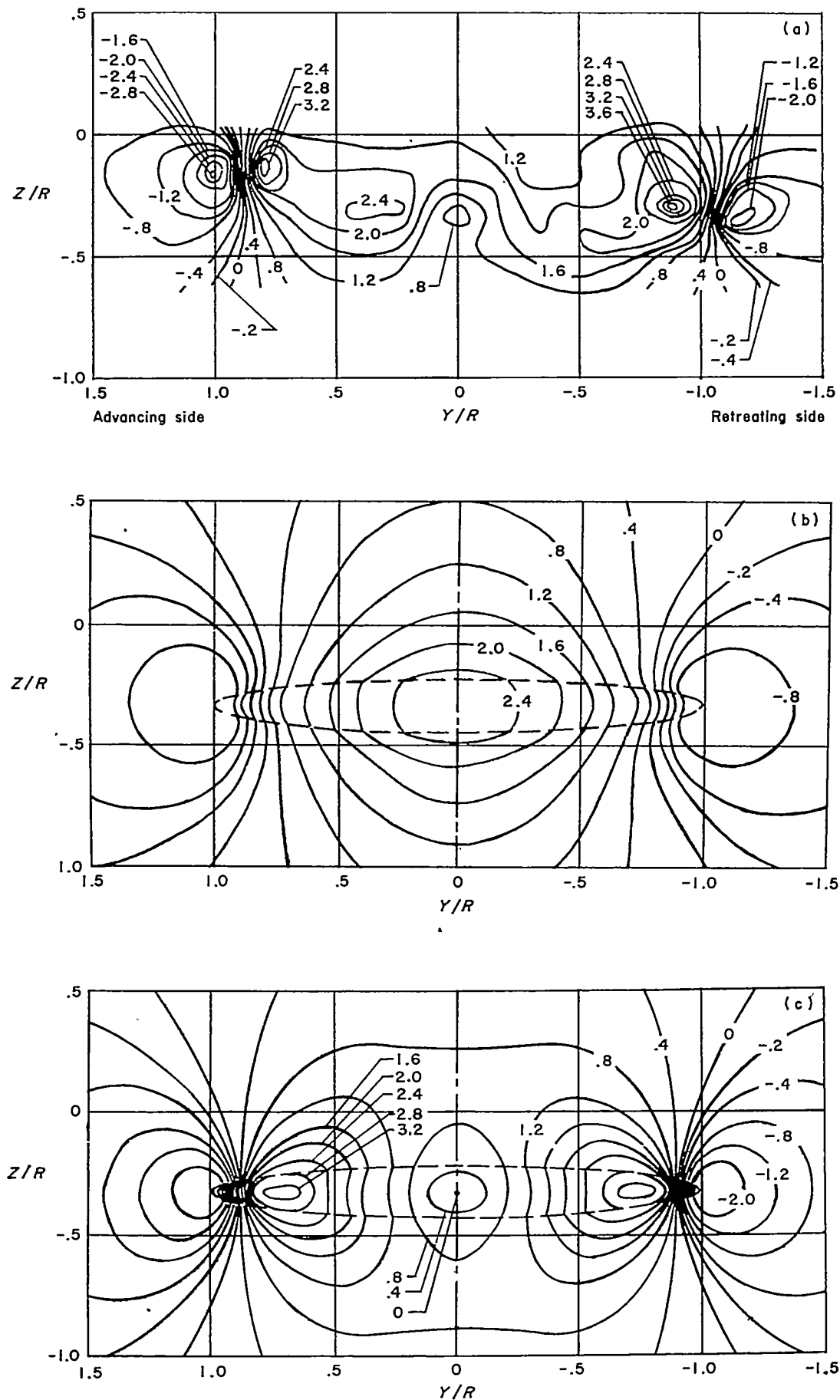


(a) Measured data.

(b) Theoretical, pressure distribution I.

(c) Theoretical, pressure distribution III.

FIGURE 37.—Comparison of measured values of induced velocity ratio v/v_0 at $X/R=2.07$ with theory of reference 5 modified. $\chi=83.9^\circ$; $\mu=0.232$.



(a) Measured data.

(b) Theoretical, pressure distribution I.

(c) Theoretical, pressure distribution III.

FIGURE 38.—Comparison of measured values of induced-velocity ratio v/v_0 at $X/R=3.14$ with theory of reference 5 modified. $\alpha=83.9^\circ$; $\mu=0.232$.

In general, the measured induced velocities are of the same order of magnitude as the calculated values. This result would be expected, regardless of the flow pattern assumed for the calculations, since a given amount of downward momentum must be imparted to the air to obtain a given lift. The distribution of induced velocity is, however, rather different from the calculated values, particularly in the central portion of the wake. In some cases, the calculated induced-velocity field in the usual location of short-span tail surfaces could be incorrect by as much as $1.5v_0$.

NATURE OF THE FLOW

At this point the reason for the rather severe discrepancies between the calculated and the measured induced velocities in the rearward portion of the flow is considered. Reference 1 has already noted the rolling up of the vortex sheet behind the rotor. Figures 39 to 41 examine this phenomenon more thoroughly for three different flight conditions. These figures are contour maps of the measured local mean vorticity behind the rotor. The intersection of the outermost edge of the assumed wake (refs. 3, 4, and 6) with the survey plane is shown in each case by the dashed-line ellipse. If the assumed wake vortex pattern is correct, the contours of vorticity should be along this wake edge (or within it, depending upon the disk-load distribution).

In general, this is not true since the dominant feature in each case is the vorticity associated with the well-developed, rolled-up vortices behind the rotor tips. It should be noted that these vortices have only been displaced vertically about half as far as the center of the wake. The lower half of the elliptical sheet is essentially completely rolled up at the trailing edge (figs. 39, 40 (a), and 41). The upper half of the elliptical sheet (originating from the rear of the disk) is still visible at $X/R=1.07$, but it also is completely rolled up shortly after that point (figs. 40 (b) and 40 (c)).

The similarity between the flow behind the rotor and that behind a low-aspect-ratio wing is very close and it is possible to draw a somewhat more quantitative analogy.

Reference 15 examines the rolling up of the trailing-vortex system behind a low-aspect-ratio wing. For lift coefficients of the order of several tenths, the roll-up is essentially complete in a very short distance. Figure 9 of reference 15 shows that, for an untwisted, rectangular wing of aspect

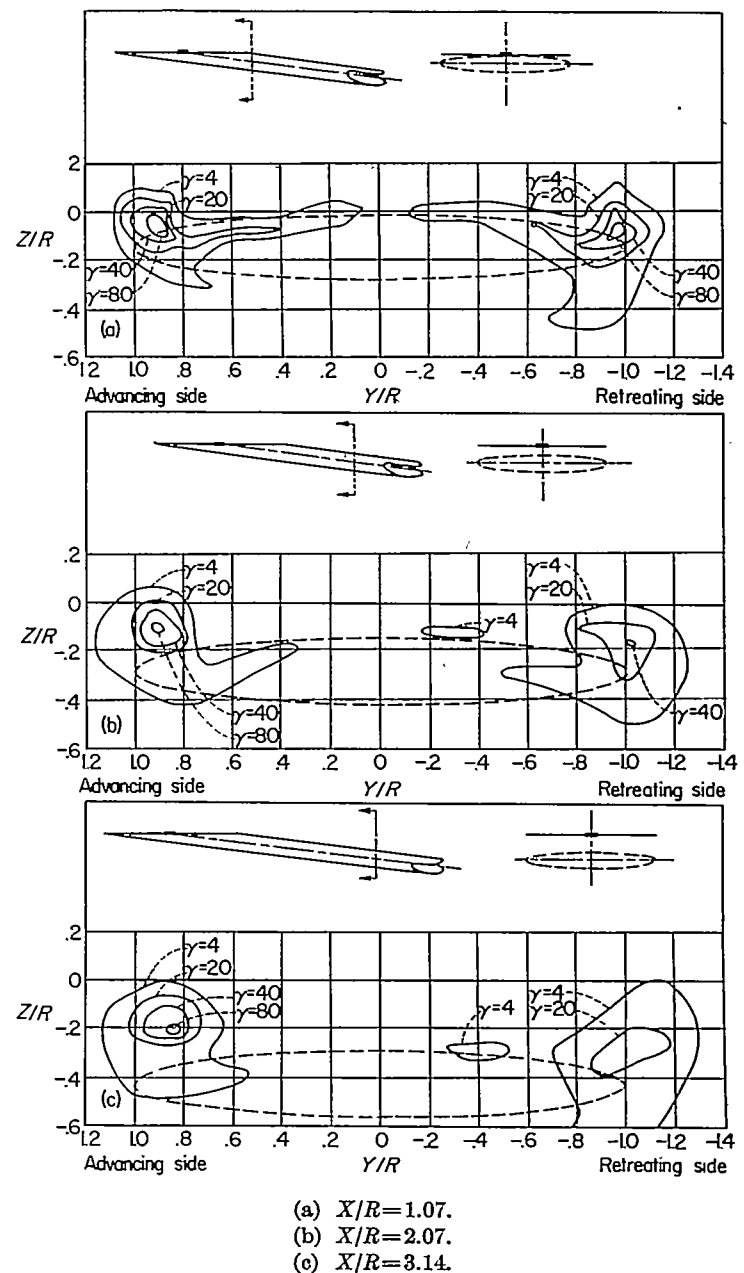


FIGURE 40.—Distribution of vorticity behind rotor. $\alpha=82.3^\circ$; $\mu=0.140$.

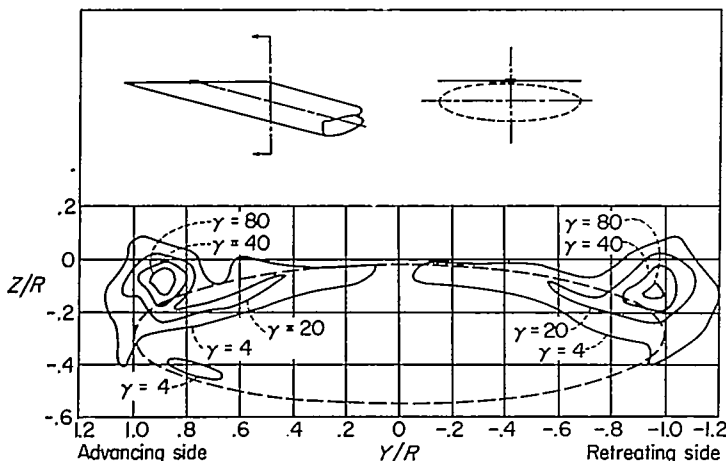


FIGURE 39.—Distribution of vorticity behind rotor. $X/R=1.07$; $\alpha=75.0^\circ$; $\mu=0.095$.

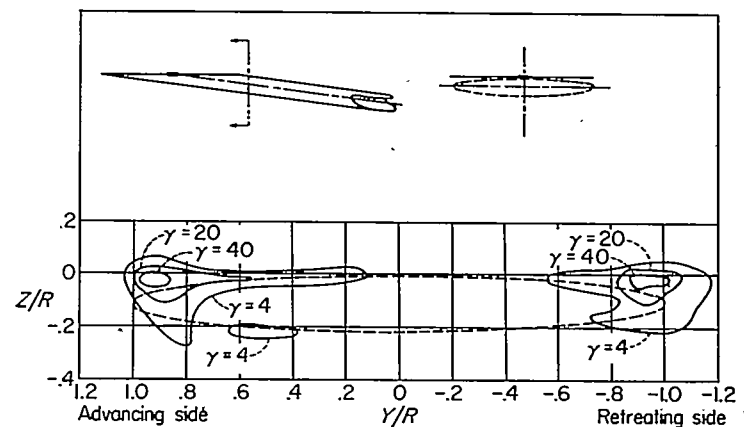


FIGURE 41.—Distribution of vorticity behind rotor. $X/R=1.07$; $\alpha=83.9^\circ$; $\mu=0.232$.

ratio $4/\pi$ (the same aspect ratio as a rotor), and for the lift coefficients used herein (0.720, 0.373, and 0.122), the roll-up distances should be 0.33, 0.64, and 1.97 times the chord length, respectively. It is more difficult to determine the rate of roll-up for something as complex as a rotor, but figures 39 to 41 indicate qualitatively that it is also extremely rapid.

These observations are further substantiated by the induced-velocity measurements previously examined in figures 19 and 21. The measured data in these figures show a marked discontinuity (which would be expected at the edge of an elliptical wake) only in the vicinity of the upper wake edge at $X/R=1.07$. Farther behind the rotor ($X/R=2.07$ and 3.14), there is no pronounced discontinuity; this condition indicates the absence of a strong vortex sheet in this region.

Figures 22 (f) and 22 (g) seem to show a discontinuity somewhat above the upper edge of the assumed wake. The previous analogy with low-aspect-ratio wings indicates the possibility that the roll-up would not be as rapid in this case because of the low rotor lift coefficient ($C_L=0.122$). The difference between the calculated and the measured flow fields may be explained on this basis. In the forward portions of the flow, the elliptical wake has not rolled up, and it therefore resembles the wake-vortex model used in the calculations. The wake here, has, of course, the greatest effect on the induced velocities in the forward portions of the flow and essentially determines their magnitude. Consequently, in this part of the flow, calculations give a reasonable picture of the actual induced velocity.

Farther rearward, however, the distorted portion of the wake has a greater effect in determining the actual induced velocity. The calculated flow field, therefore, is increasingly more inaccurate as its distance downstream increases.

A short distance behind the rotor, it should be possible to assume that the flow will be the same as that for an equivalent wing. The minimum distance behind the rotor at which this procedure will be valid is a function of the lift coefficient.

From reference 16 the induced velocity in the plane of symmetry of a uniformly loaded rectangular wing is

$$v = \frac{s\Gamma}{2\pi} \left[\frac{X}{\sqrt{s^2 + X^2 + Z^2}} \left(\frac{1}{X^2 + Z^2} + \frac{1}{s^2 + Z^2} \right) + \frac{1}{s^2 + Z^2} \right] \quad (3)$$

If it is assumed that the quarter chord of the equivalent wing and the lateral center line of the rotor coincide and also that $s=0.85R$ (the approximate center of gravity of the vortex system),

$$v = \frac{0.85R\Gamma}{2\pi} \left\{ \frac{X}{\sqrt{(0.85R)^2 + X^2 + Z^2}} \left[\frac{1}{X^2 + Z^2} + \frac{1}{(0.85R)^2 + Z^2} \right] + \frac{1}{(0.85R)^2 + Z^2} \right\} \quad (4)$$

If nondimensionalized, equation (4) becomes

$$\frac{2\pi Rv}{\Gamma} = 0.85 \left\{ \frac{(X/R)^2}{\sqrt{0.723 + \left(\frac{X}{R}\right)^2 + \left(\frac{Z}{R}\right)^2}} \left[\frac{1}{\left(\frac{X}{R}\right)^2 + \left(\frac{Z}{R}\right)^2} + \frac{1}{0.723 + \left(\frac{Z}{R}\right)^2} \right] + \frac{1}{0.723 + \left(\frac{Z}{R}\right)^2} \right\} \quad (5)$$

Now

$$\Gamma = \frac{L}{2\rho VR} \quad (6)$$

and, for skew angles near 90° ,

$$v_0 = \frac{L}{2\rho V\pi R^2} \quad (7)$$

Substituting equation (6) into equation (5) and dividing both sides of the resulting equation by equation (7) gives

$$\frac{v}{v_0} = 0.425 \left\{ \frac{\frac{X}{R}}{\sqrt{0.723 + \left(\frac{X}{R}\right)^2 + \left(\frac{Z}{R}\right)^2}} \left[\frac{1}{\left(\frac{X}{R}\right)^2 + \left(\frac{Z}{R}\right)^2} + \frac{1}{0.723 + \left(\frac{Z}{R}\right)^2} \right] + \frac{1}{0.723 + \left(\frac{Z}{R}\right)^2} \right\} \quad (8)$$

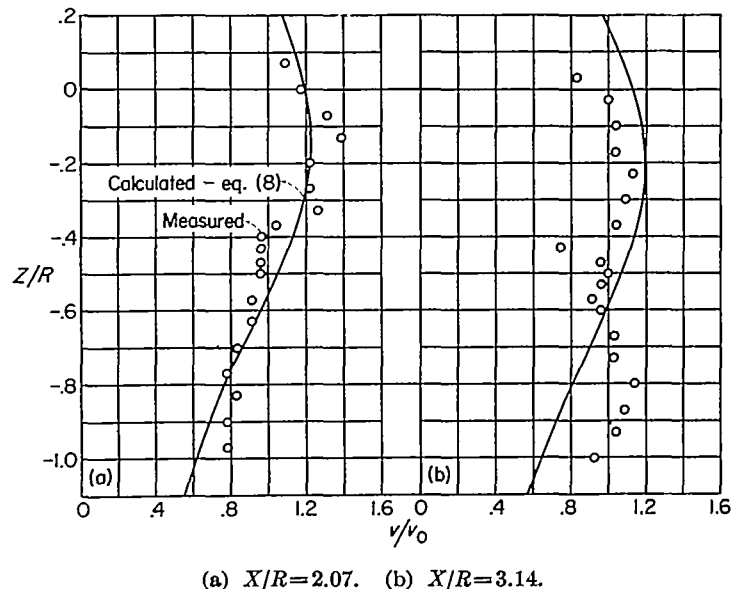


FIGURE 12.—Comparison in the plane of symmetry of measured values of induced-velocity ratio v/v_0 with those calculated for an equivalent wing. $\chi=82.3^\circ$; $\mu=0.140$.

The flow calculated by this equation is symmetrical about $Z/R=0$; that is, it does not allow for the vertical displacement of the wake. As pointed out previously, the centers of the vortices are displaced downward an amount

$$\Delta \frac{Z}{R} = \frac{1}{2} \frac{X}{R} \cot \chi \quad (9)$$

The induced velocity for this assumed wing has been calculated from equations (8) and (9) and is compared with the flow measured at $X/R=2.07$ and 3.14 (for $\mu=0.140$ and $\chi=82.3^\circ$) in figure 42. As expected in these rearward planes, it is a closer approximation to the actual flow than are the flows calculated on the basis of a skewed cylindrical wake (fig. 21, for example).

CONCLUSIONS FOR PART III

The results of this wind-tunnel investigation of the induced flow near a single rotor in simulated cruising and high-speed flight are as follows:

1. As far rearward as three-quarters of a diameter behind the leading edge of the rotor disk, the normal component of induced velocity of a lifting rotor may be calculated with good accuracy by available theory provided that a realistic nonuniform disk loading is assumed.
2. Rearward of this three-quarter diameter point, calculation of the induced velocity becomes increasingly inaccurate because the trailing-vortex system rolls up very rapidly, and the wake vortex pattern behind the rotor is altered from that assumed as a basis for the calculations.
3. At locations well behind the rotor, the induced flow may be calculated more accurately by assuming the rotor to be a uniformly loaded rectangular wing, provided that the rotor lift coefficient is sufficiently high.
4. There is little effect of the asymmetries associated with tip-speed ratio on the induced flow along the longitudinal axis of the rotor.
5. The induced-velocity calculations of Mangler and Squire can be modified to account for the wake crossing the flow because of the finite lift coefficient.

LANGLEY AERONAUTICAL LABORATORY,
NATIONAL ADVISORY COMMITTEE FOR AERONAUTICS,
LANGLEY FIELD, VA., December 7, 1956.

REFERENCES

1. Heyson, Harry H.: Preliminary Results From Flow-Field Measurements Around Single and Tandem Rotors in the Langley Full-Scale Tunnel. NACA TN 3242, 1954.
2. Falabella, Gaetano, Jr., and Meyer, John R., Jr.: Determination of Inflow Distributions From Experimental Aerodynamic Loading and Blade-Motion Data on a Model Helicopter Rotor in Hovering and Forward Flight. NACA TN 3492, 1955.

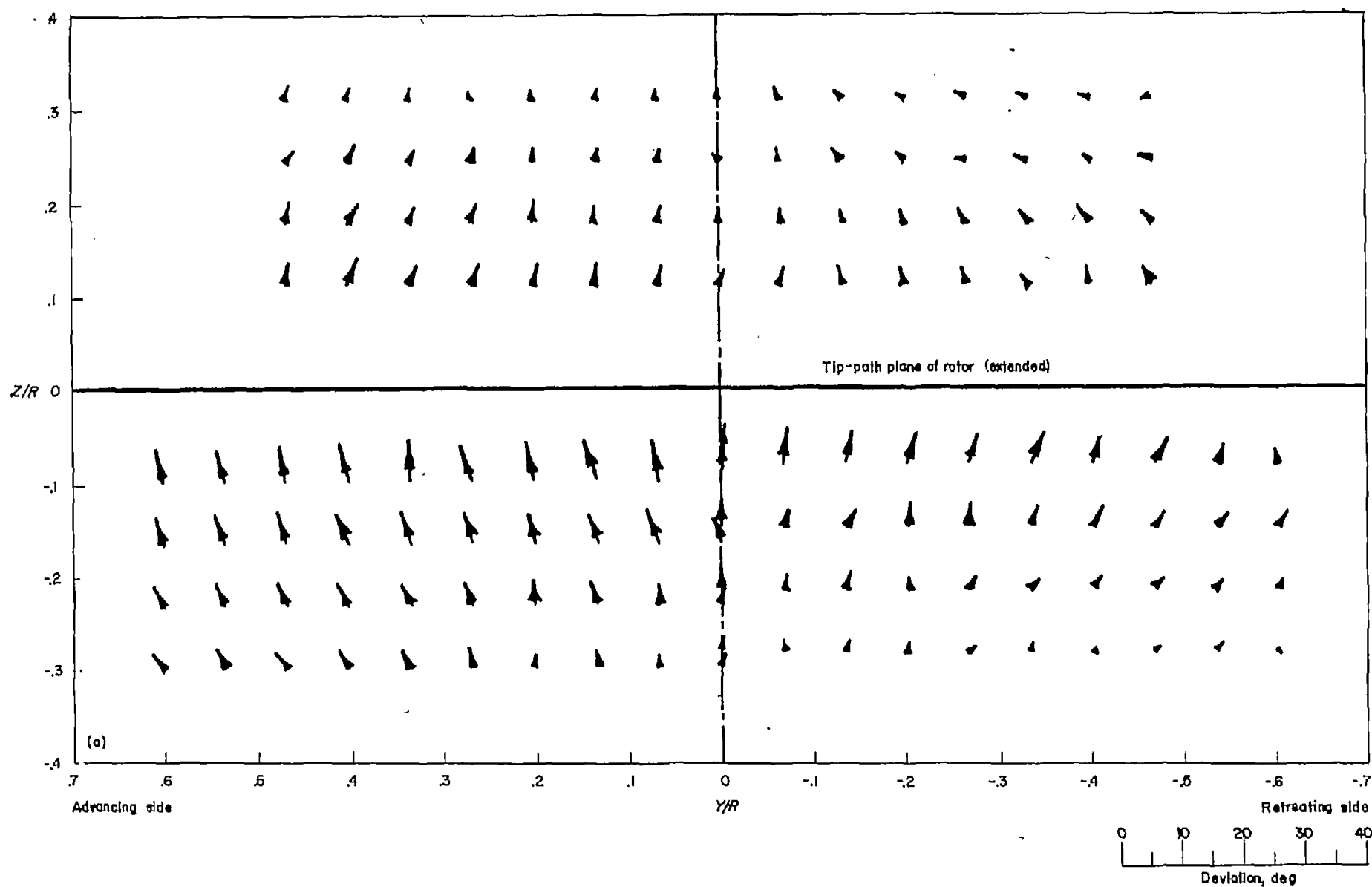
3. Coleman, Robert P., Feingold, Arnold M., and Stempin, Carl W.: Evaluation of the Induced-Velocity Field of an Idealized Helicopter Rotor. NACA WR L-126, 1945. (Formerly NACA ARR L5E10.)
4. Drees, J. Meijer: A Theory of Airflow Through Rotors and Its Application to Some Helicopter Problems. Jour. Helicopter Assoc. of Great Britain, vol. 3, no. 2, July-Aug.-Sept. 1949, pp. 79-104.
5. Mangler, K. W., and Squire, H. B.: The Induced Velocity Field of a Rotor. R. & M. No. 2642, British A.R.C., May 1950.
6. Castles, Walter, Jr., and De Leeuw, Jacob Henri: The Normal Component of the Induced Velocity in the Vicinity of a Lifting Rotor and Some Examples of Its Application. NACA Rep. 1184, 1954. (Supersedes NACA TN 2912.)
7. Gessow, Alfred: Review of Information on Induced Flow of a Lifting Rotor. NACA TN 3238, 1954.
8. Bateman, H.: Partial Differential Equations of Mathematical Physics. American ed., Dover Publications, 1944, p. 256.
9. Kennelly, A. E.: Tables of Complex Hyperbolic and Circular Functions. Second ed., Harvard Univ. Press, 1927.
10. Peirce, B. O.: A Short Table of Integrals. Third rev. ed., Ginn and Co., 1929, pp. 38-39.
11. DeFrance, Smith J.: The N.A.C.A. Full-Scale Wind Tunnel. NACA Rep. 459, 1933.
12. Lange, Roy H., and Fink, Marvin P.: Studies of the Flow Field Behind a Large-Scale 47.5° Sweptback Wing Having Circular-Arc Airfoil Sections and Equipped With Drooped-Nose and Plain Flaps. NACA RM L51L12, 1952.
13. Silverstein, Abe, and Katzoff, S.: Experimental Investigation of Wind-Tunnel Interference on the Downwash Behind an Airfoil. NACA Rep. 609, 1937.
14. Fail, R. A., and Eyre, R. C. W.: Downwash Measurements Behind a 12-Ft Diameter Helicopter Rotor in the 24-Ft Wind Tunnel. R. & M. No. 2810, British A.R.C., Sept. 1949.
15. Spreiter, John R., and Sacks, Alvin H.: The Rolling Up of the Trailing Vortex Sheet and Its Effect on the Downwash Behind Wings. Jour. Aero. Sci., vol. 18, no. 1, Jan. 1951, pp. 21-32, 72.
16. Silverstein, Abe, Katzoff, S., and Bullivant, W. Kenneth: Downwash and Wake Behind Plain and Flapped Airfoils. NACA Rep. 651, 1939.

APPENDIX

BASIC DATA

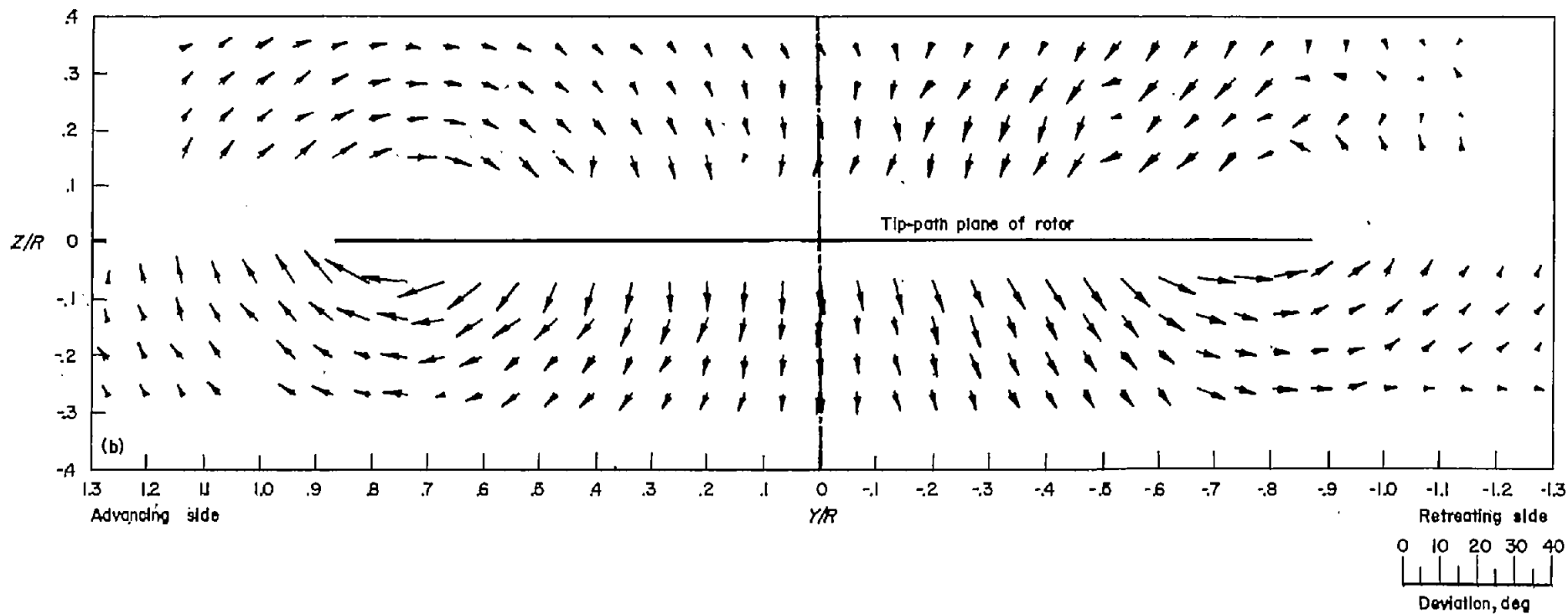
At present the knowledge of the flow field near a lifting rotor is very limited. Because of this lack of information substantially all of the basic data obtained in the experimental investigation are presented in this appendix. In each case, the rotor flight condition is identified by the skew angle χ and the tip-speed ratio μ . Table I (p. 877) identifies the flight conditions more completely.

Figures 43 to 45 show the measured stream angles in the flow; figures 46 to 48 show contours of dynamic-pressure ratio; and figures 49 to 69 give the measured values of the induced velocity ratio. The fairings of the measured data, shown in figures 49 to 69, are those used in the analysis of part III.



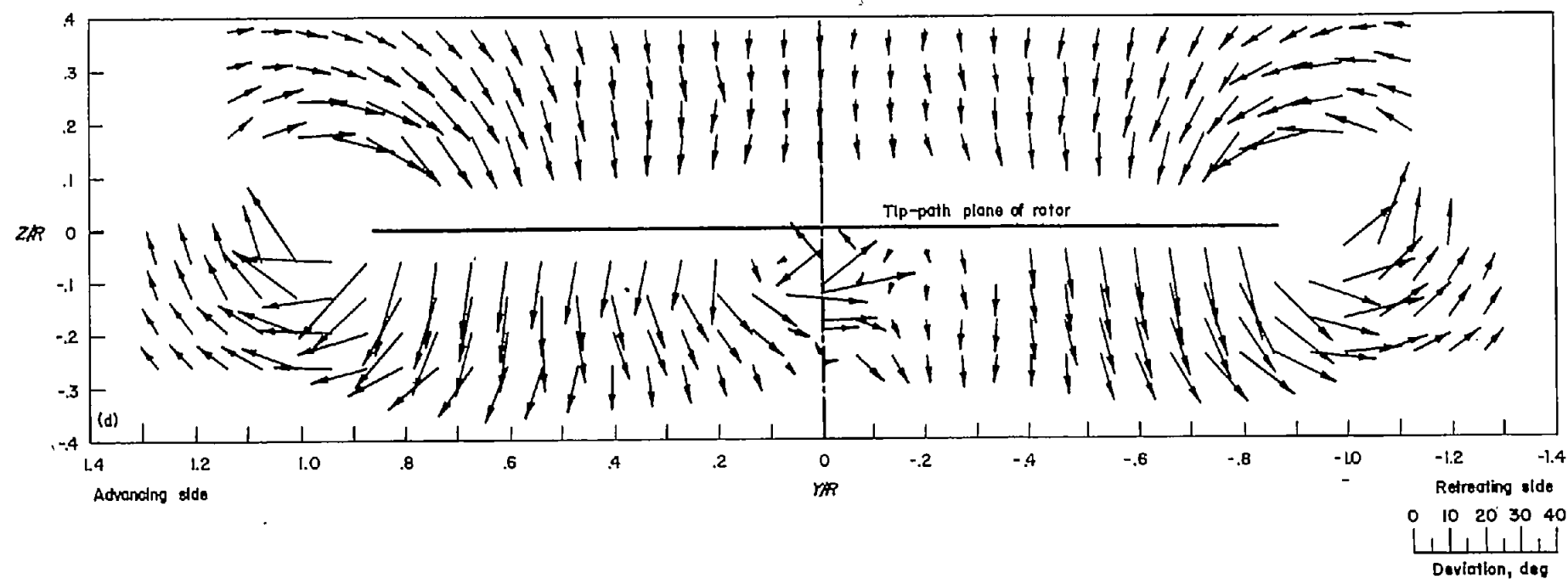
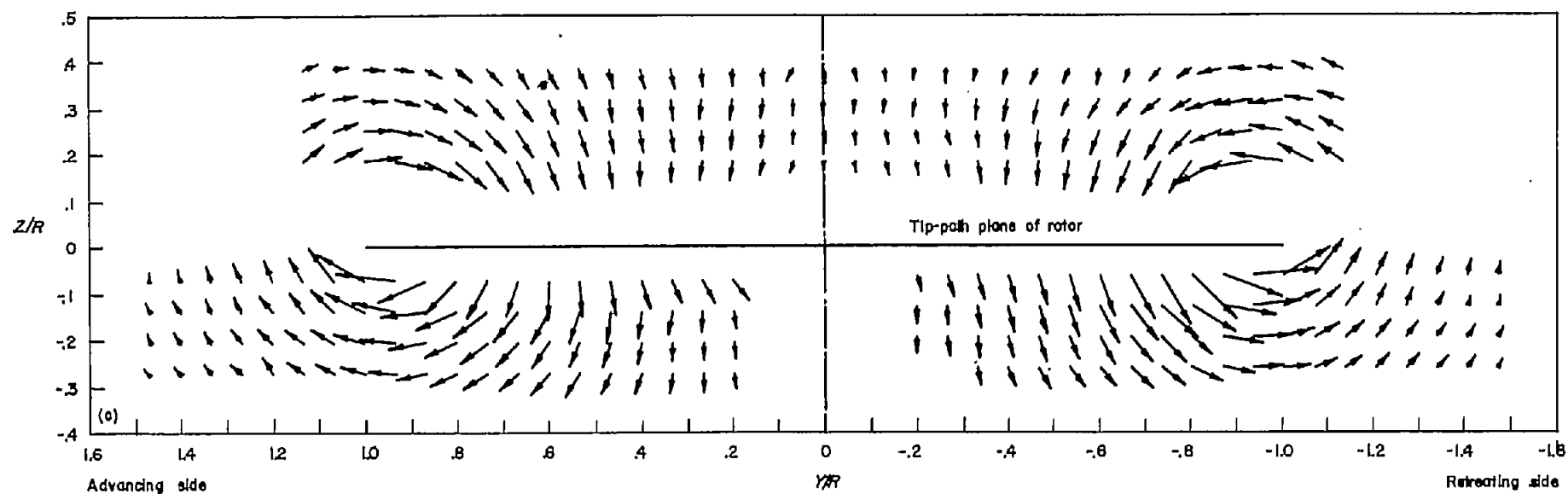
(a) $X/R = -1.0$.

FIGURE 43.—Measured stream angles in vicinity of rotor. Horizontal and vertical components of vectors represent yaw and pitch angles. Base of vector is at point of measurement. $\alpha = 75.0^\circ$; $\mu = 0.095$.



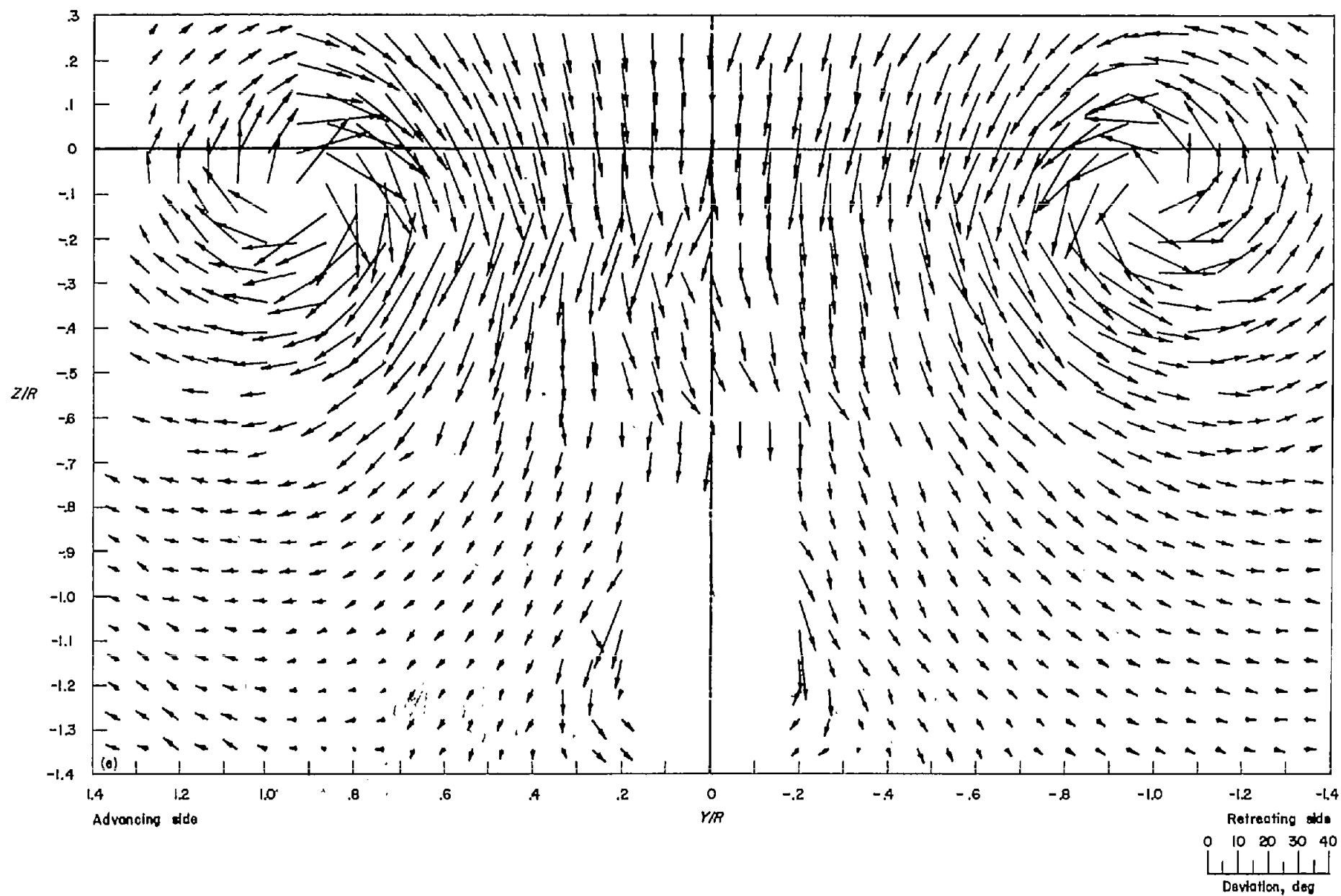
(b) $X/R = -0.5$.

FIGURE 48.—Continued.



(c) $X/R=0$.
(d) $X/R=0.5$.

FIGURE 43.—Continued.



(a) $X/R=1.07$.
FIGURE 43.—Continued.

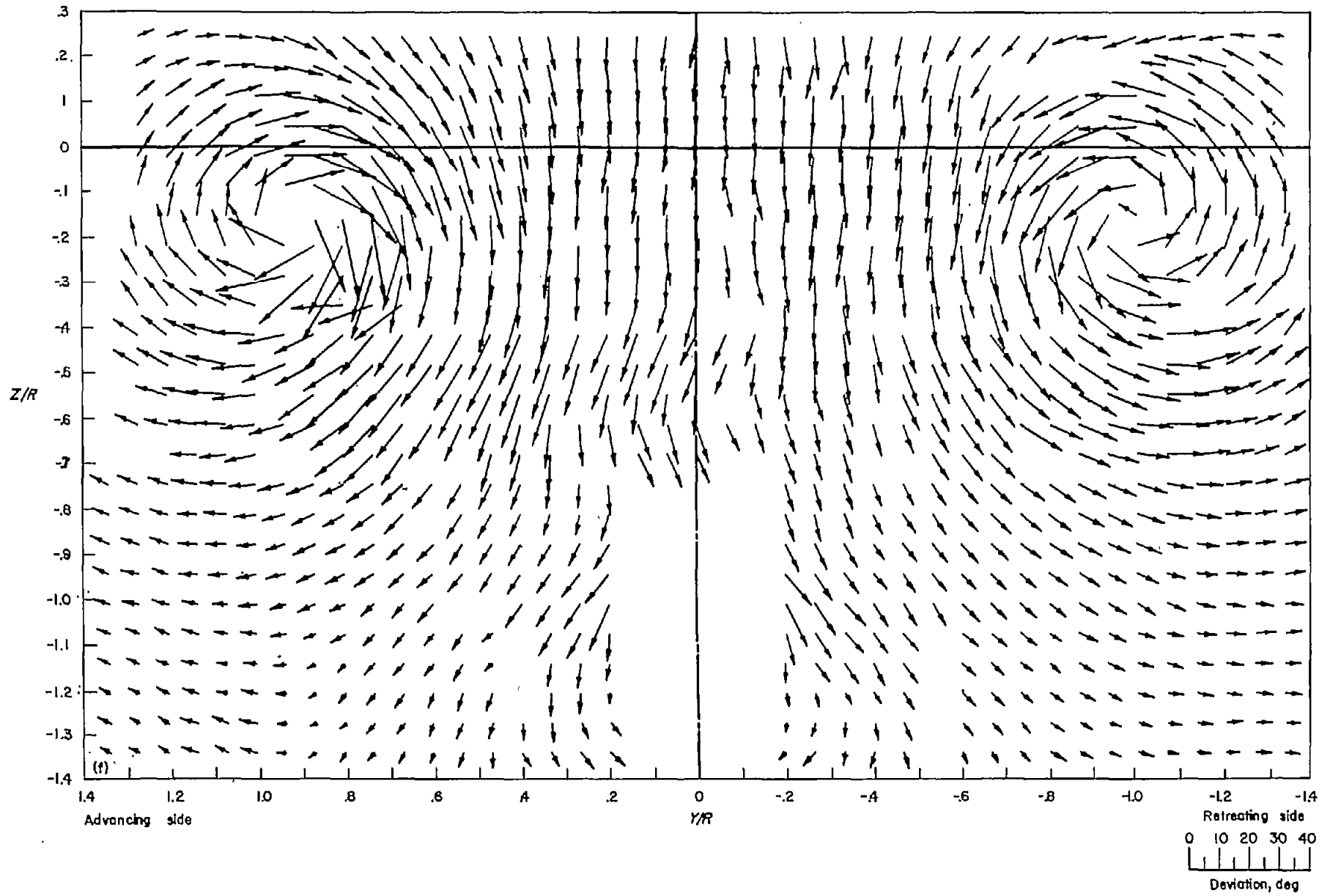
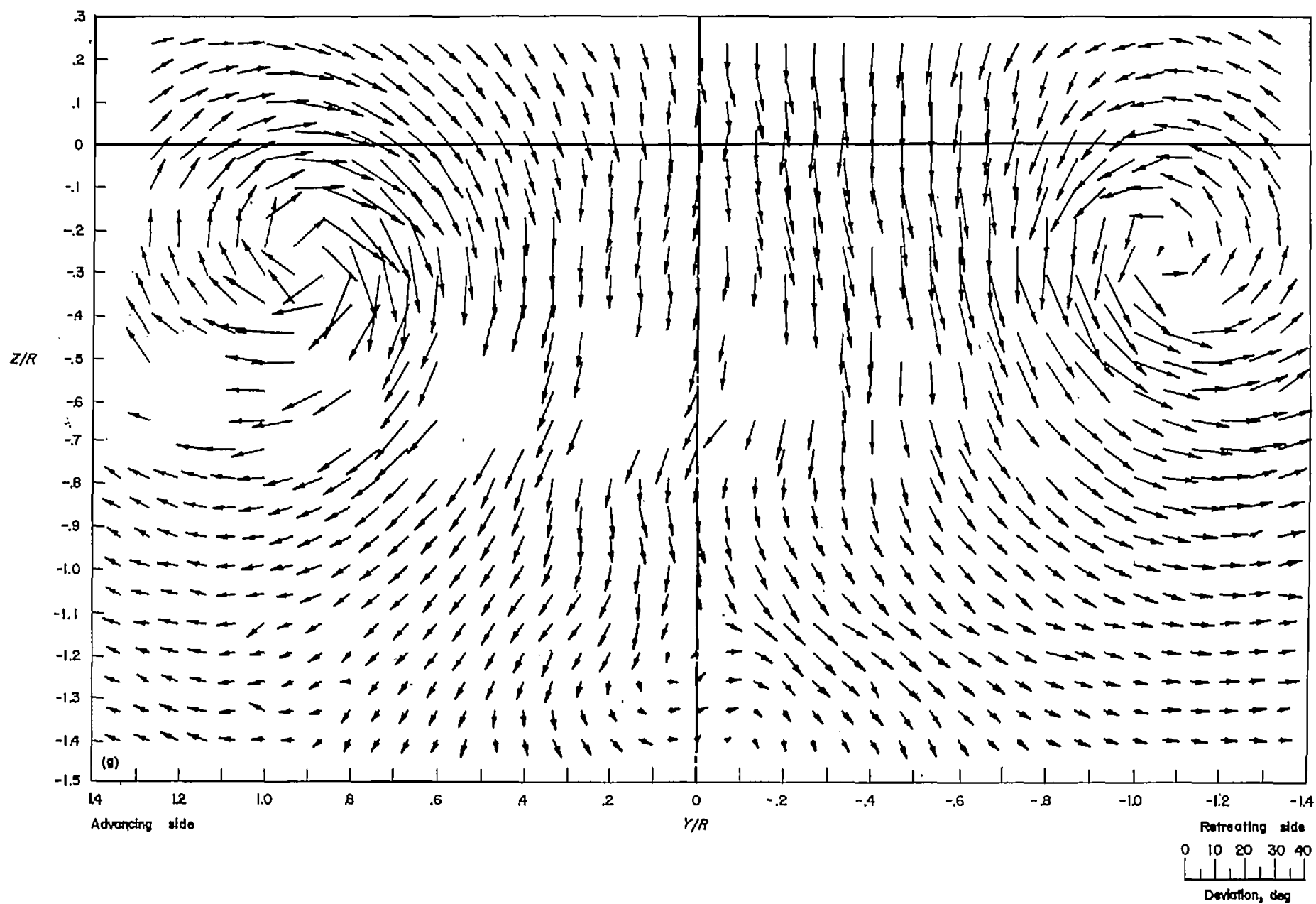
(f) $X/R=2.07$.

FIGURE 43.—Continued.



(g) $X/R=3.14$.

FIGURE 43.—Concluded.

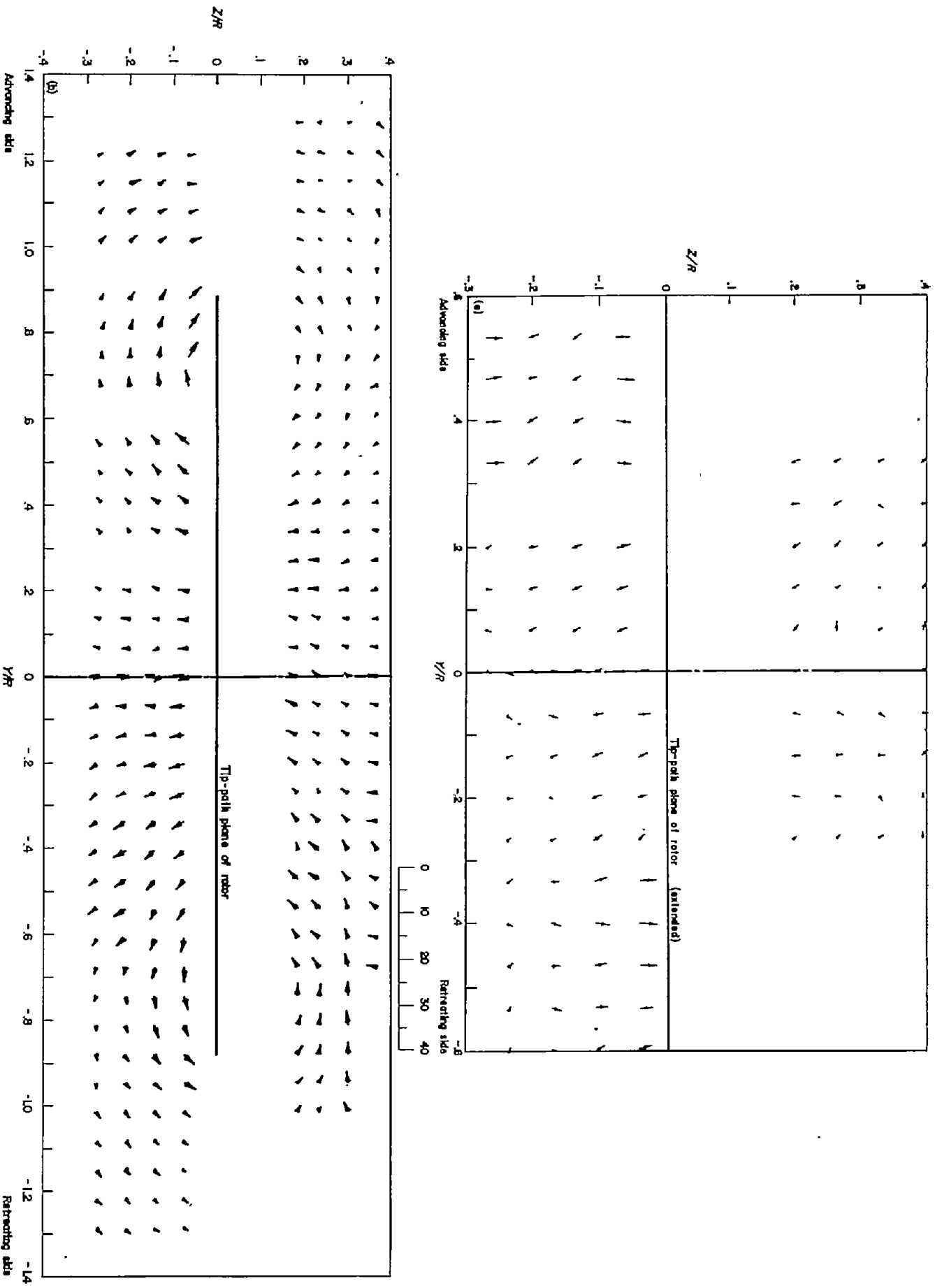
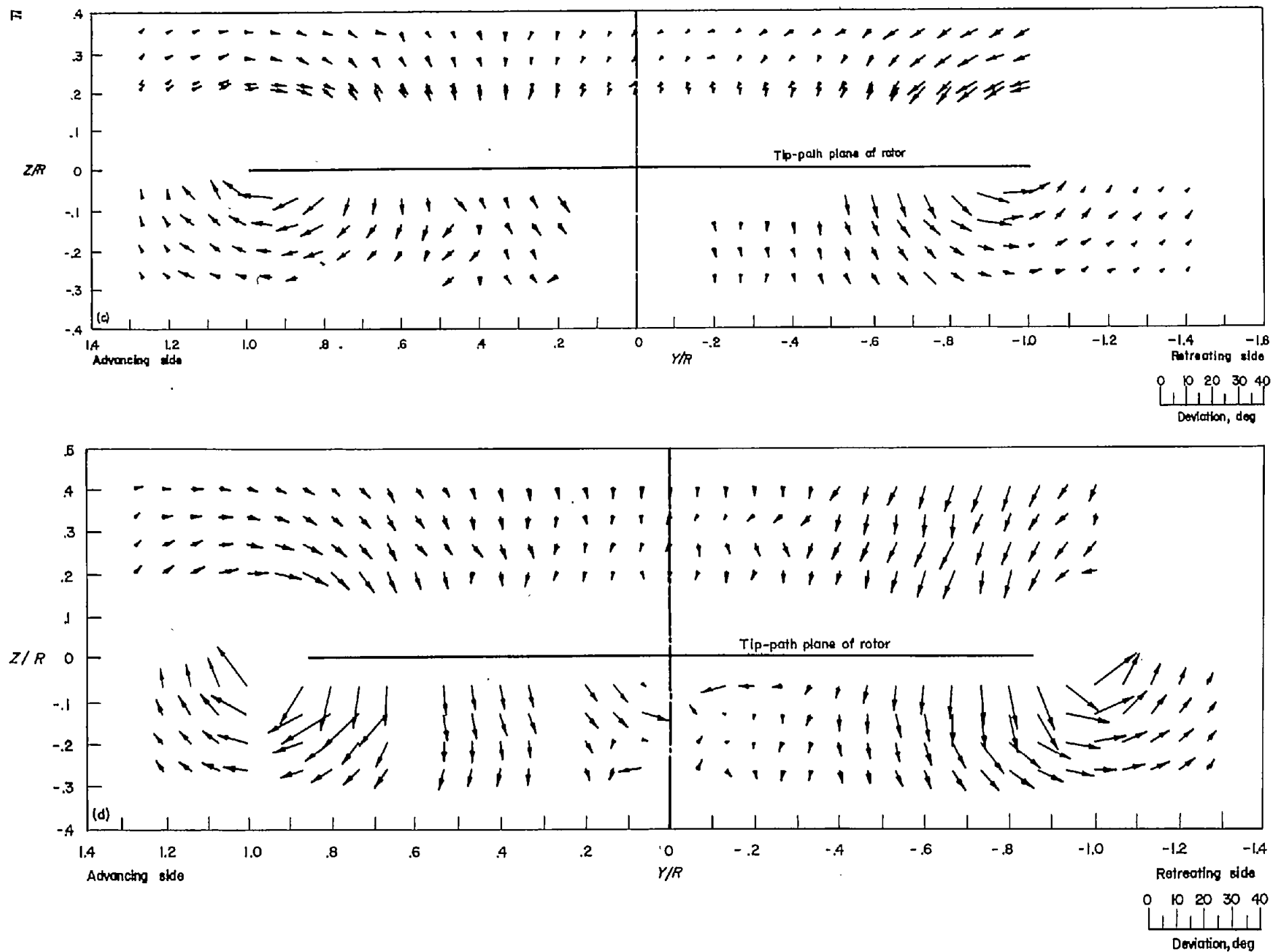
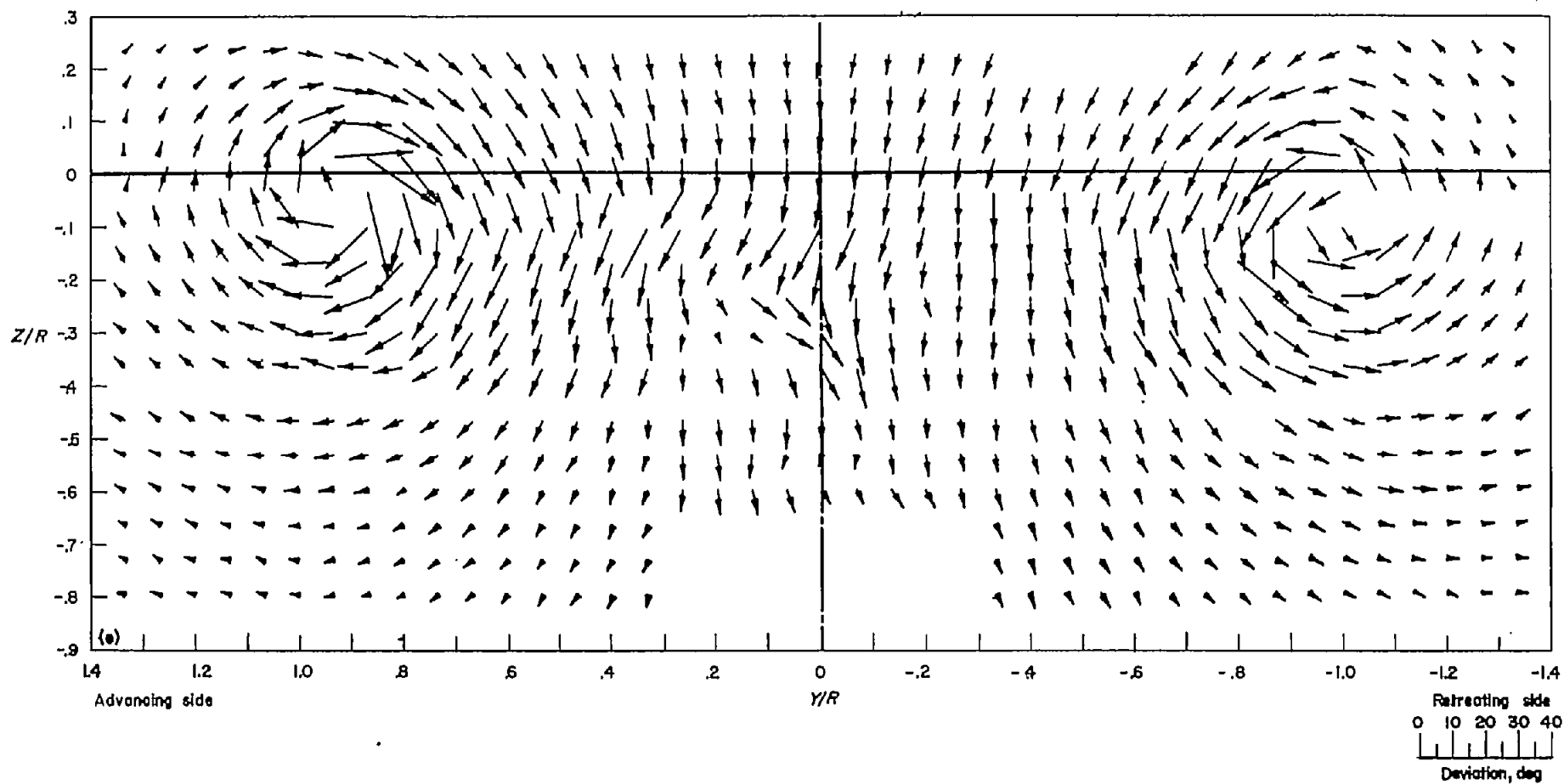


FIGURE 44.—Measured stream angles in vicinity of rotor. Horizontal and vertical components of vectors represent yaw and pitch angles. Base of vector is at point of measurement. $\alpha = 82.3^\circ$ $\mu = 0.140$.

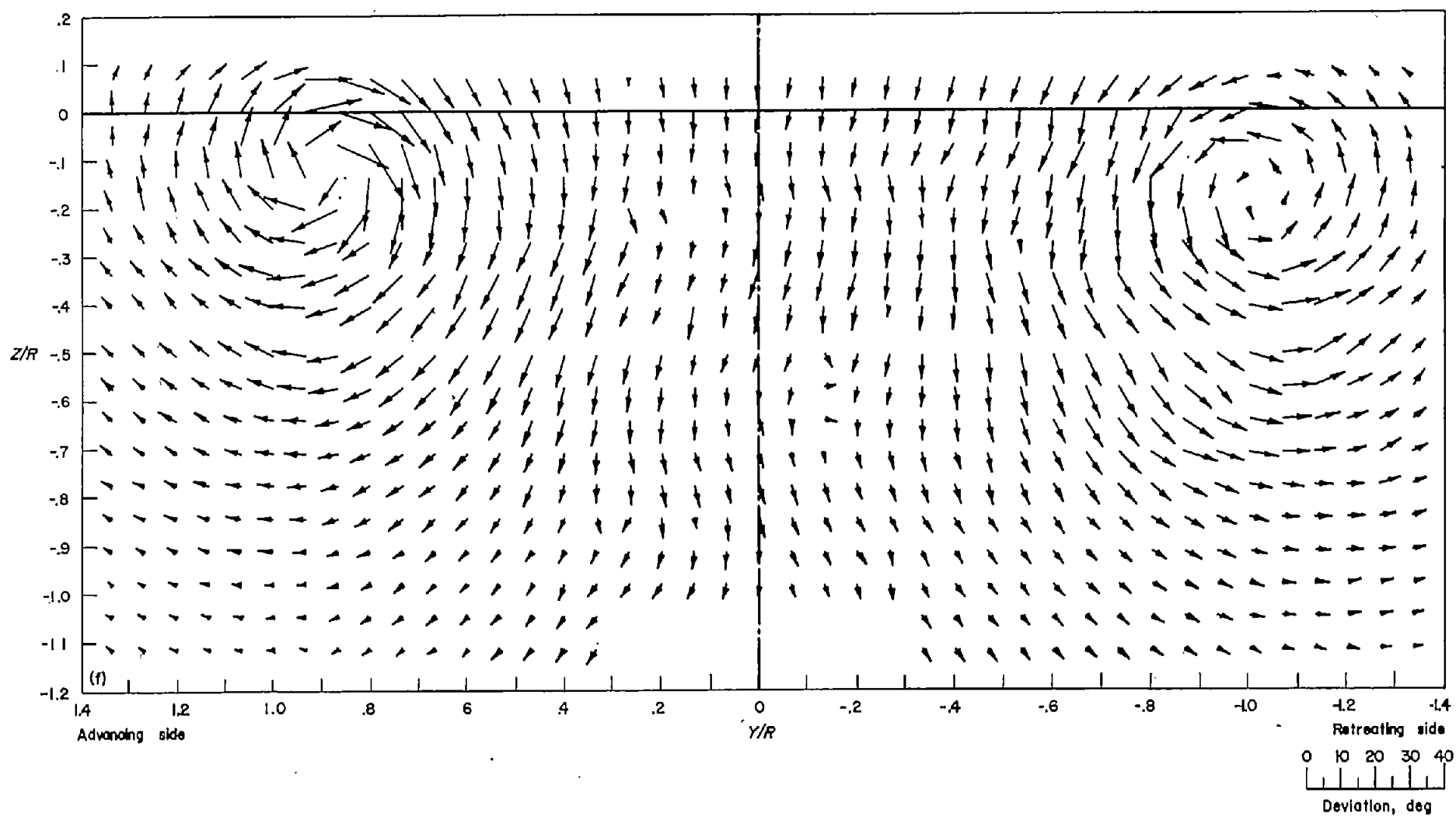


(c) $X/R=0$.
 (d) $X/R=0.5$.

FIGURE 44.—Continued.

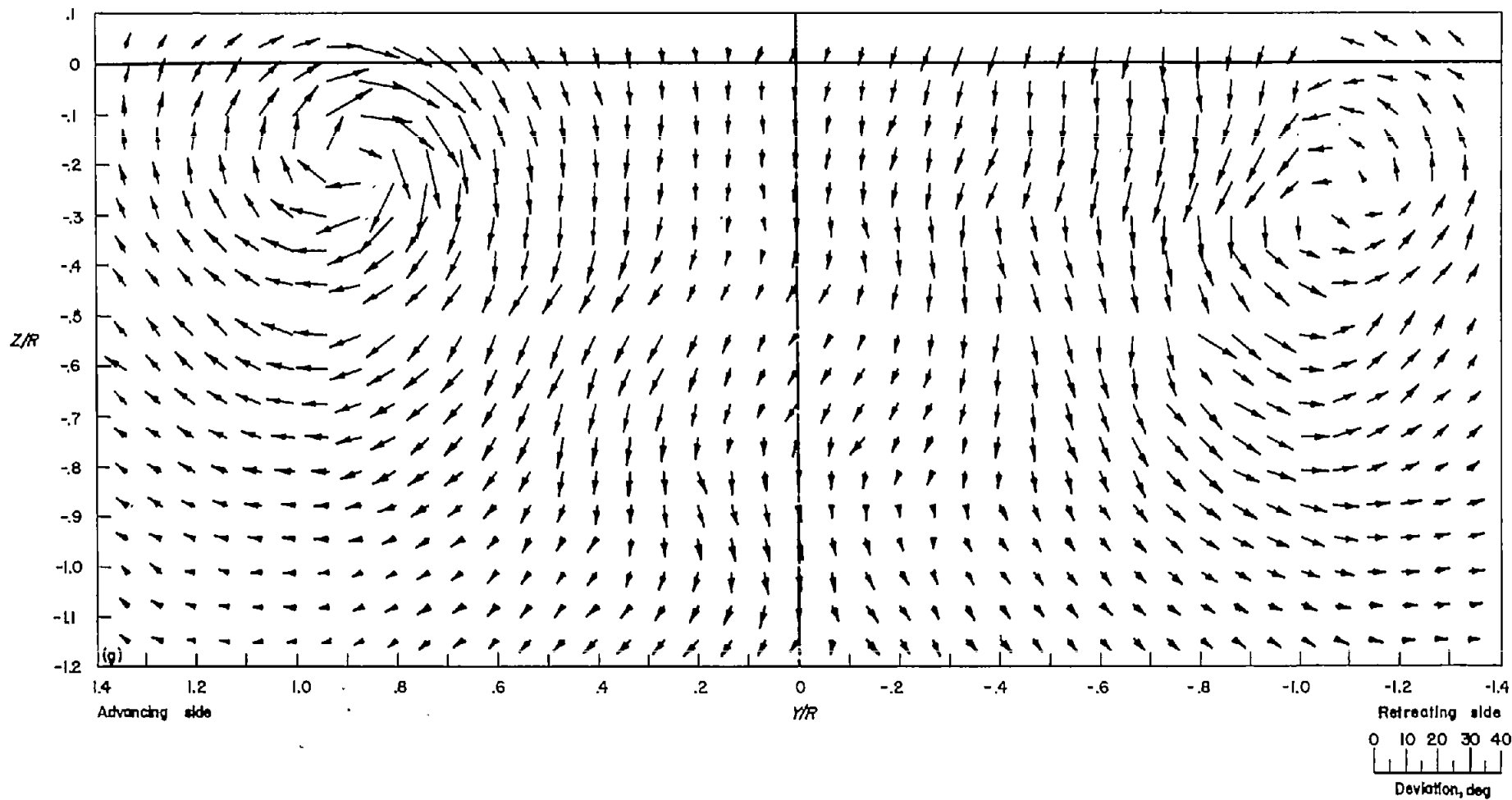


(e) $X/R=1.07$.
FIGURE 44.—Continued.



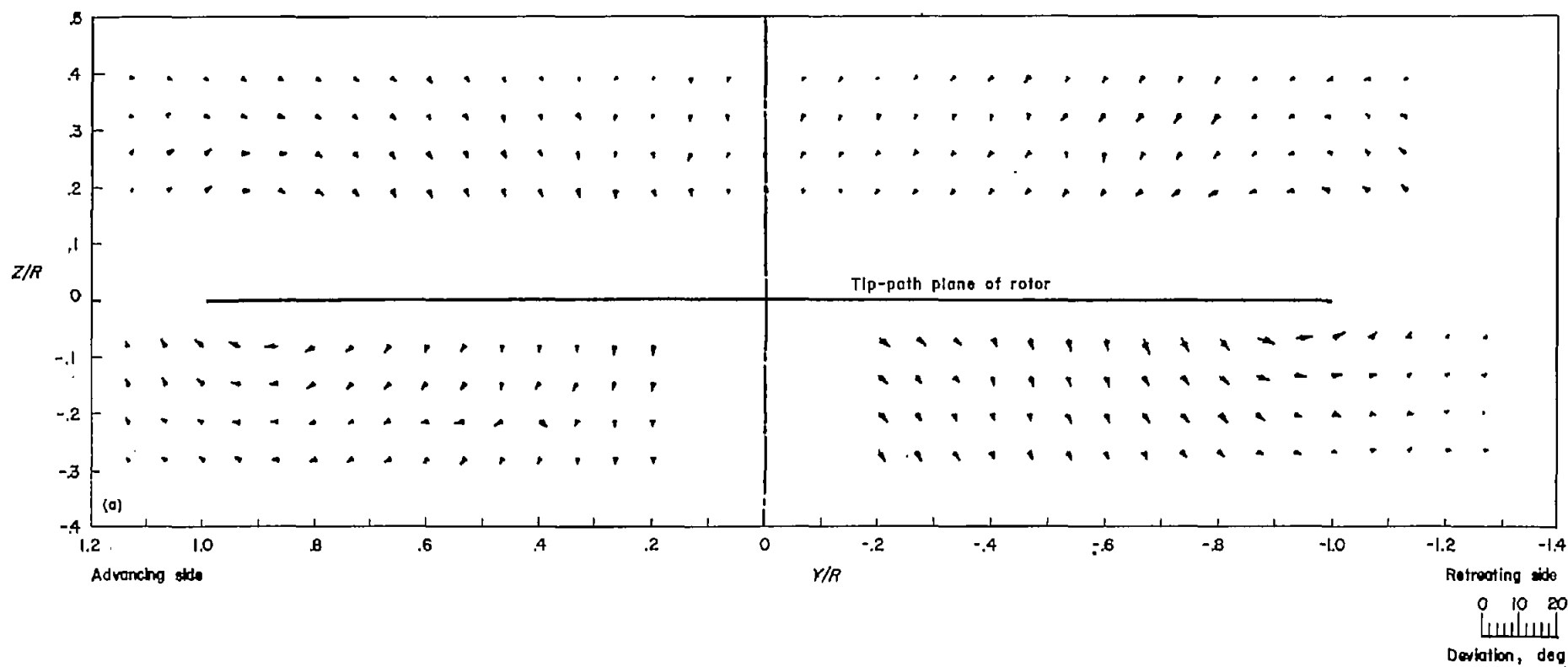
(f) $X/R=2.07$.

FIGURE 44.—Continued.



(g) $X/R=3.14$.

FIGURE 44.—Concluded.



(a) $X/R=0$.

FIGURE 45.—Measured stream angles in vicinity of rotor. Horizontal and vertical components represent yaw and pitch angles. Base of vector is at point of measurement. $\alpha=83.9^\circ$; $\mu=0.232$.

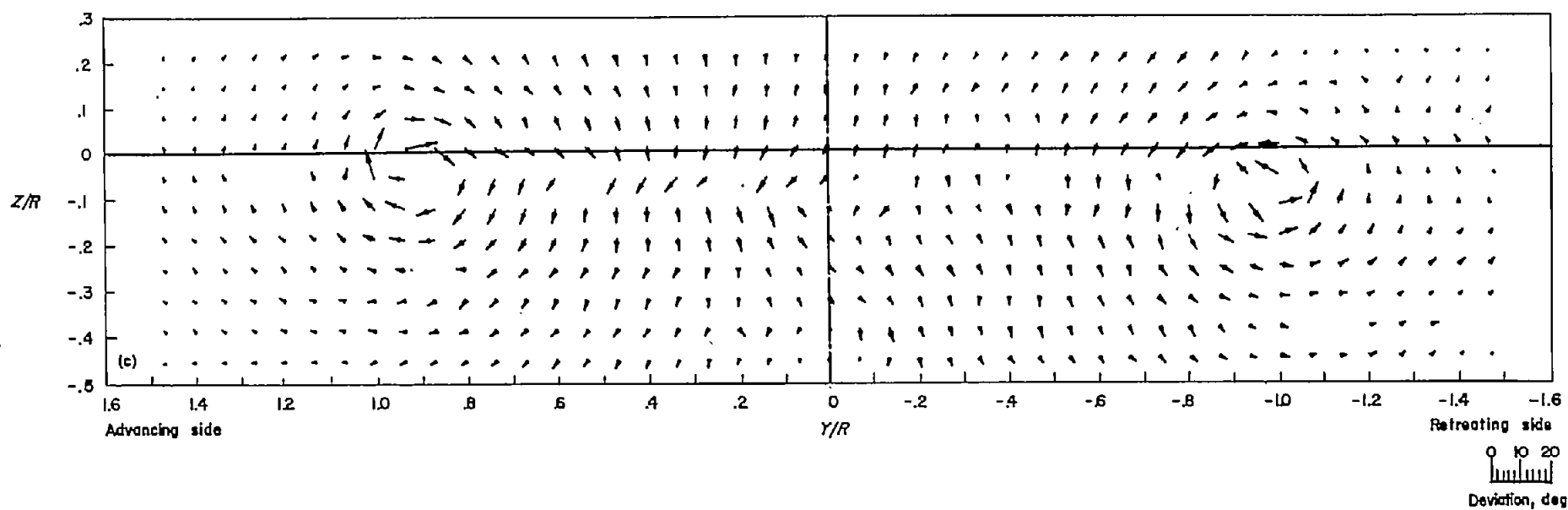
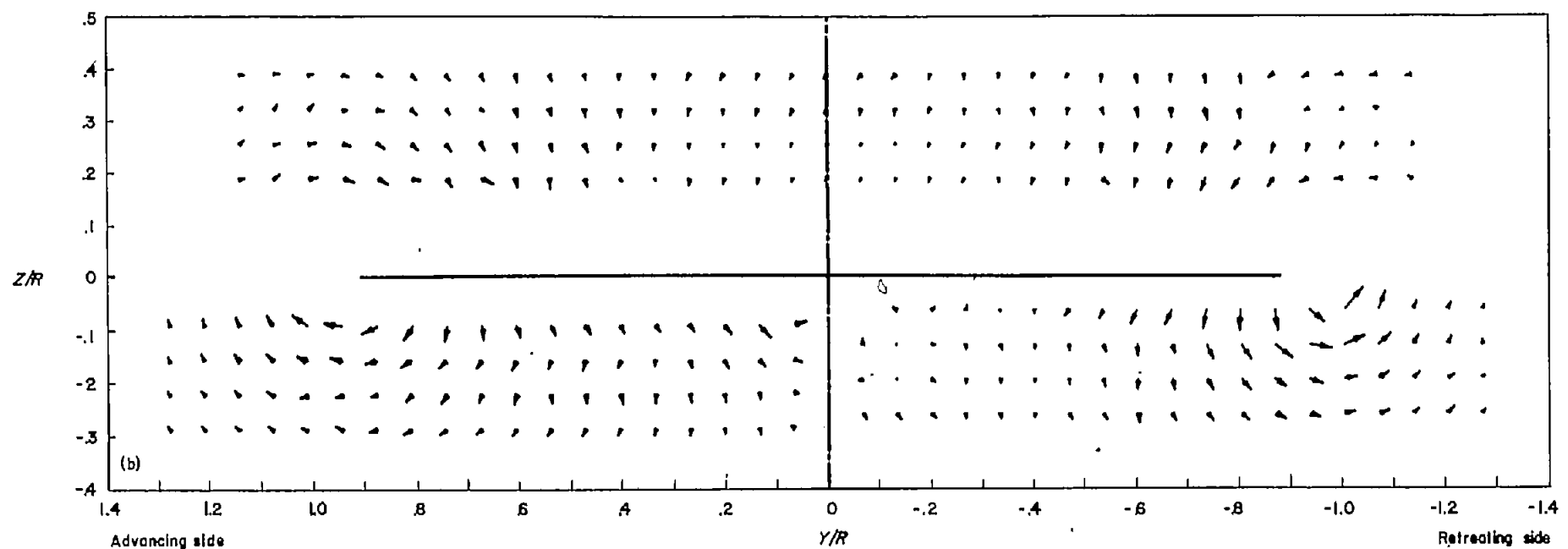
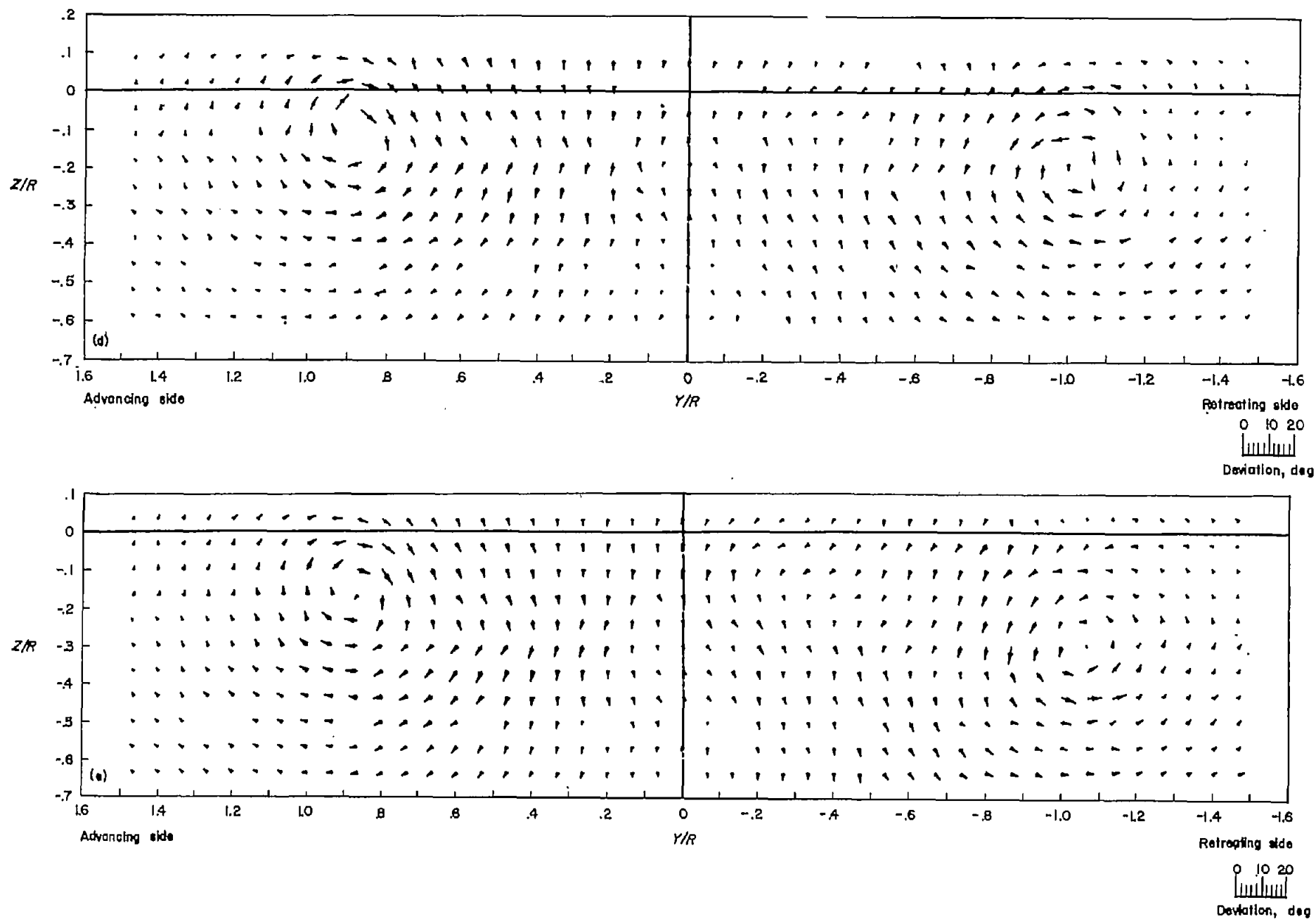
(b) $X/R=0.5$.(c) $X/R=1.07$.

FIGURE 45.—Continued.



(d) $X/R = 2.07$.

(e) $X/R = 3.14$.

FIGURE 45.—Concluded.

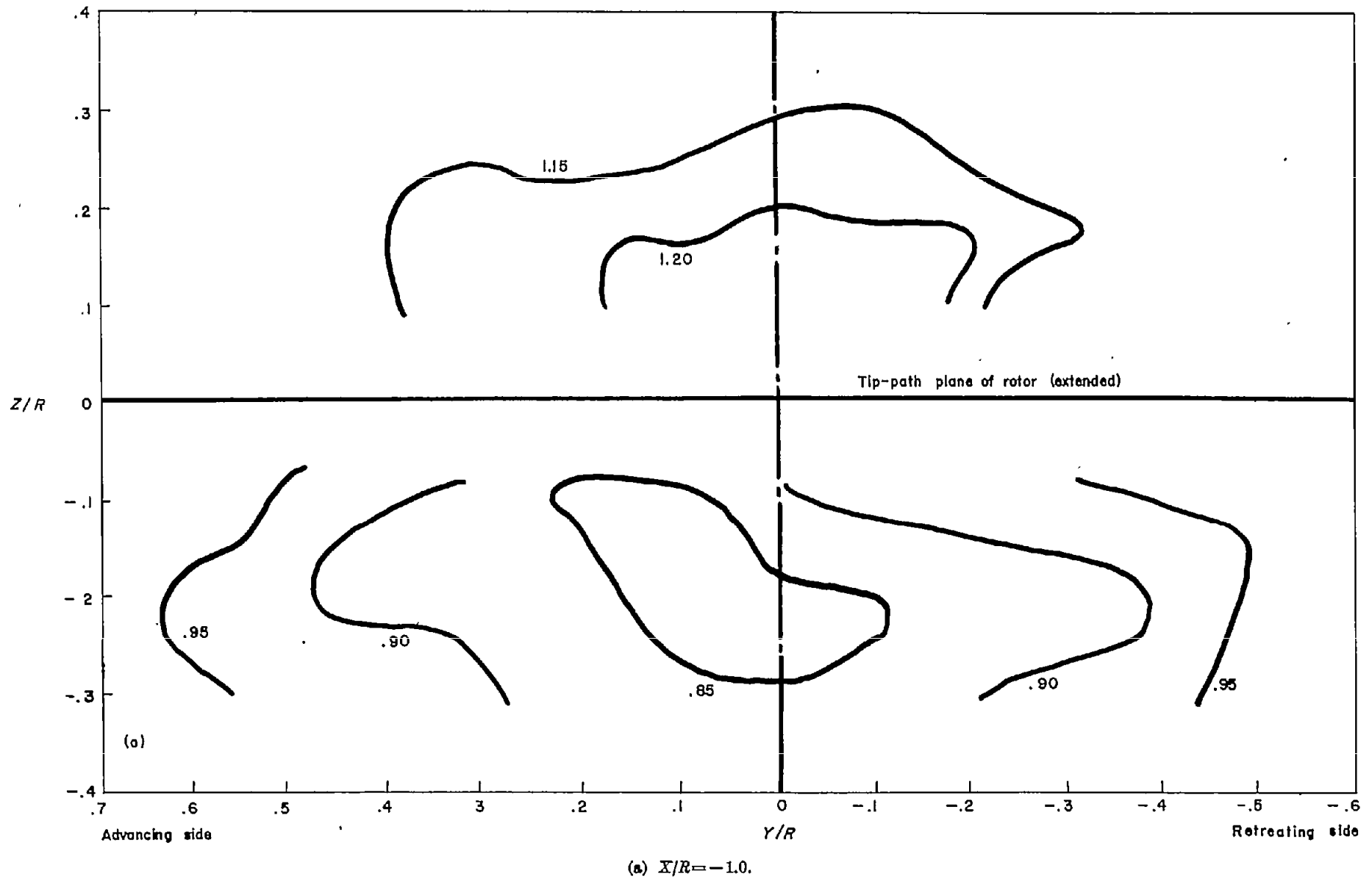
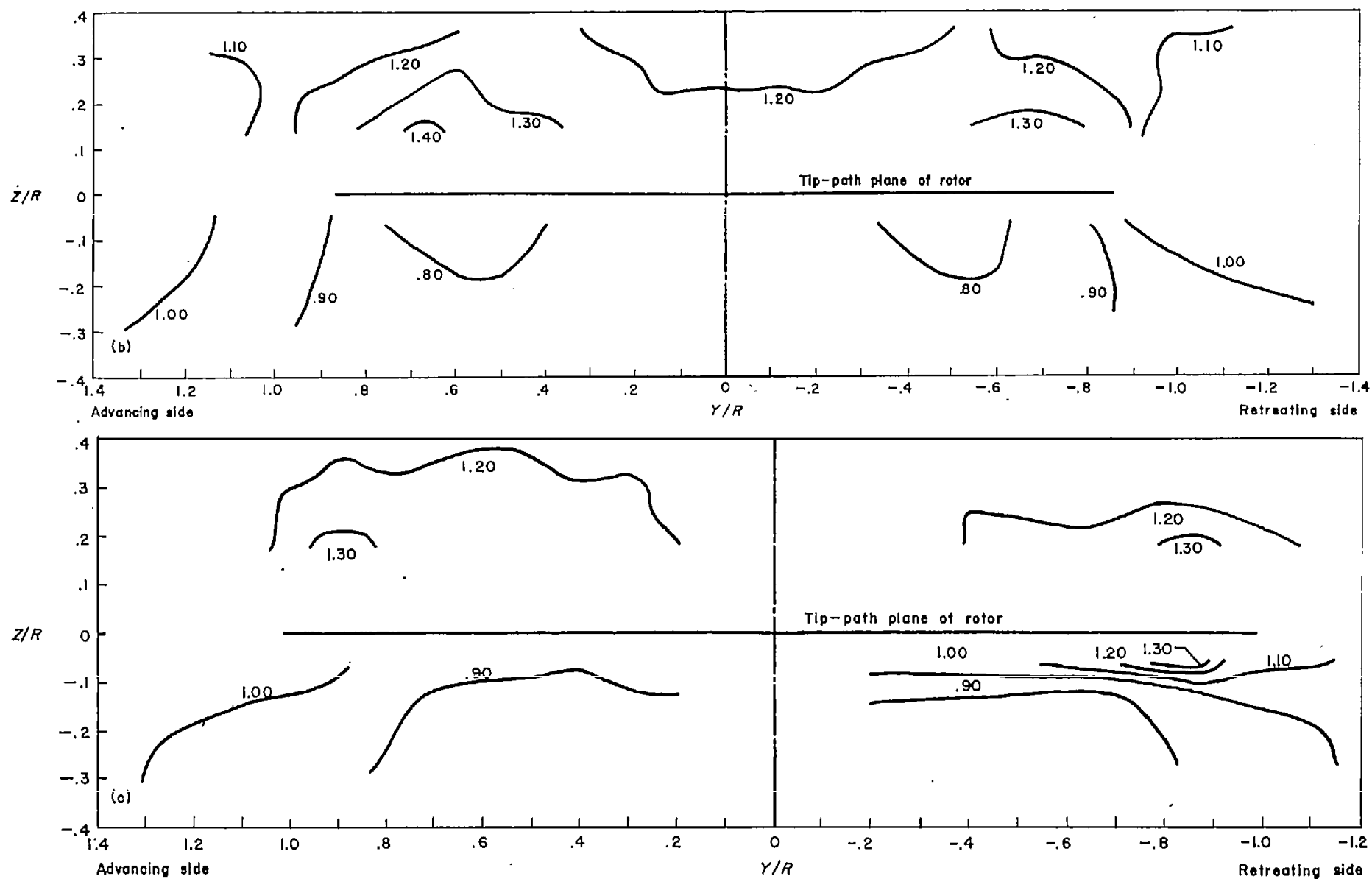


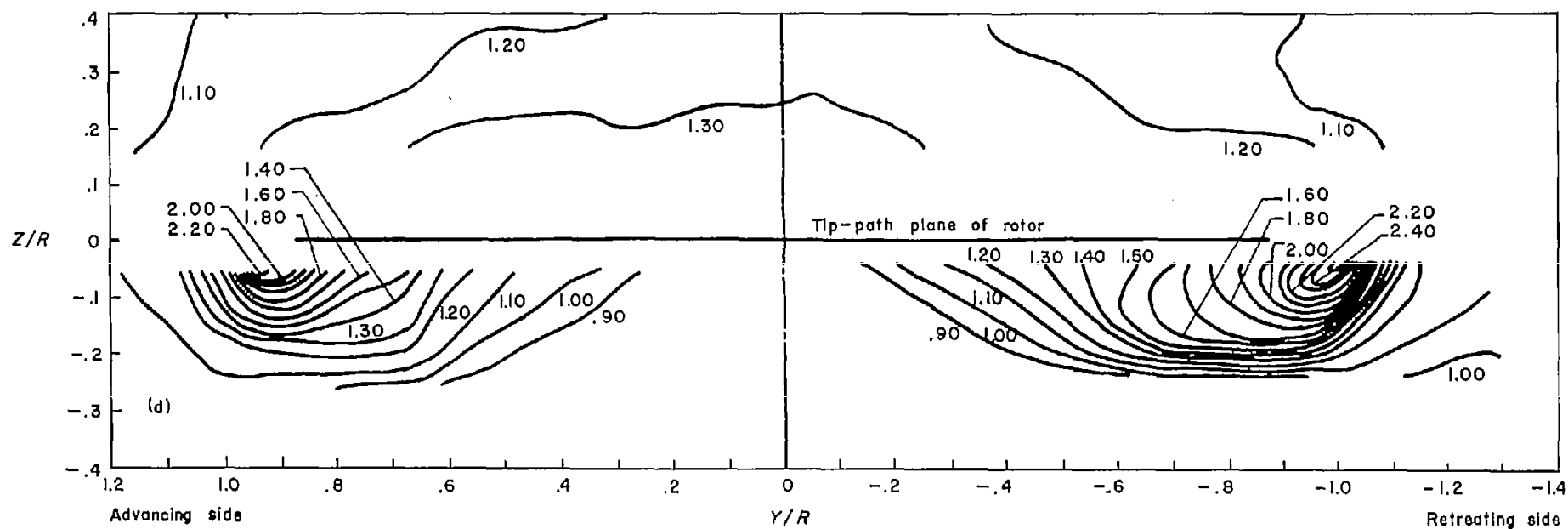
FIGURE 46.—Contours of dynamic pressure q/q_0 in the vicinity of the rotor. $\chi = 75.0^\circ$; $\mu = 0.095$.



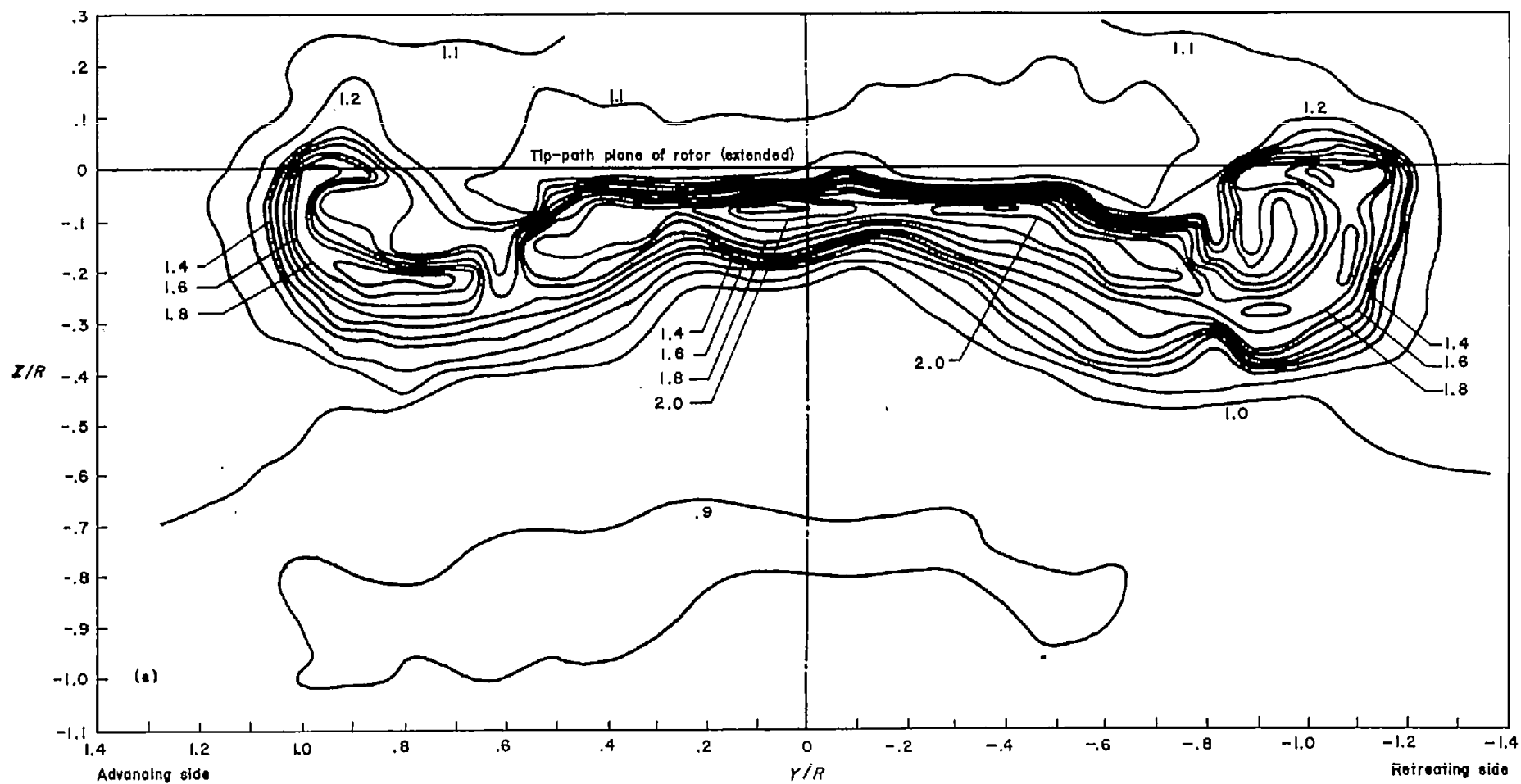
(b) $X/R = -0.50$,

(c) $X/R = 0$.

FIGURE 4b.—Continued.



(d) $X/R=0.5$.
FIGURE 40.—Continued.



(a) $X/R=1.07$.

FIGURE 46.—Continued.

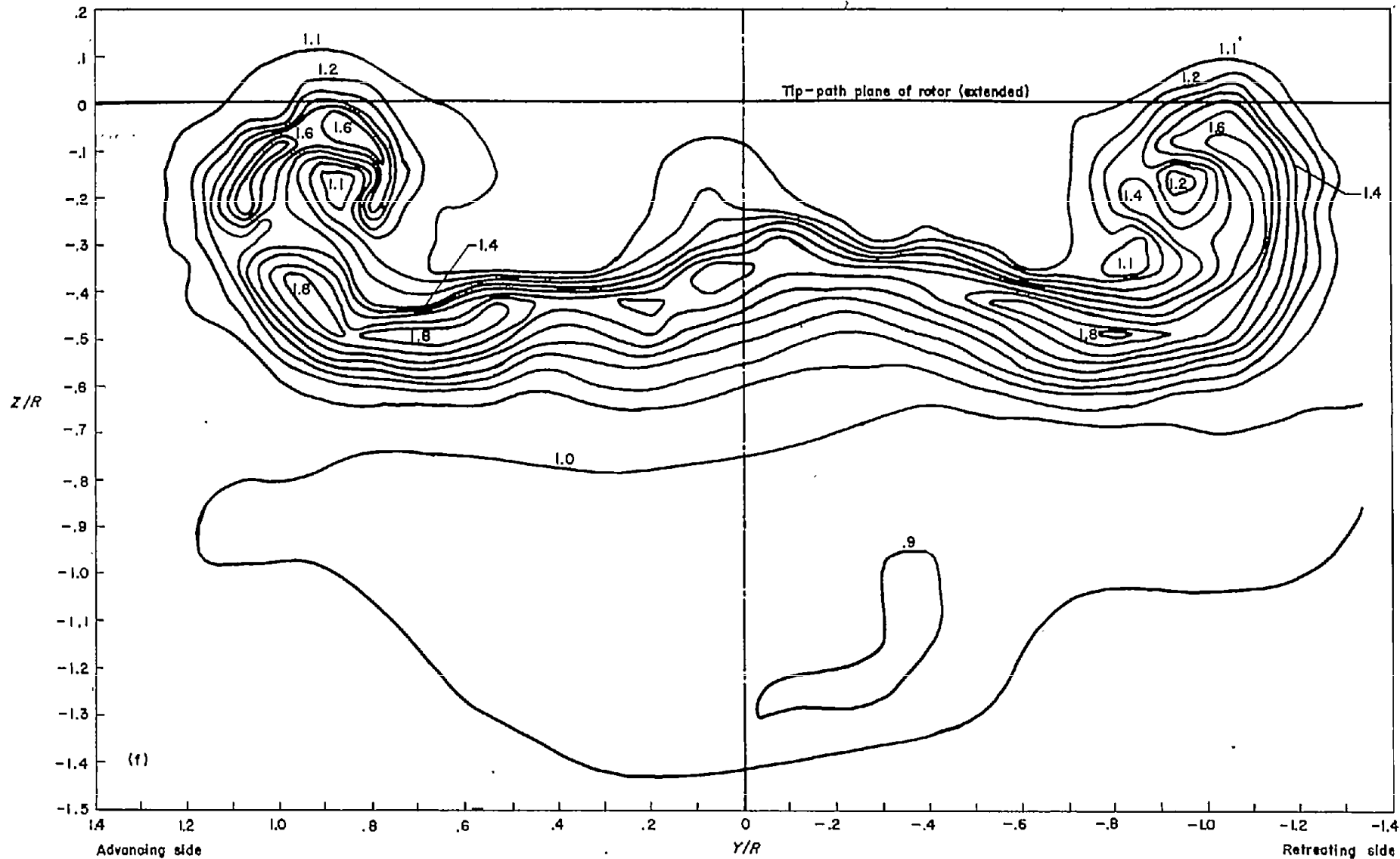
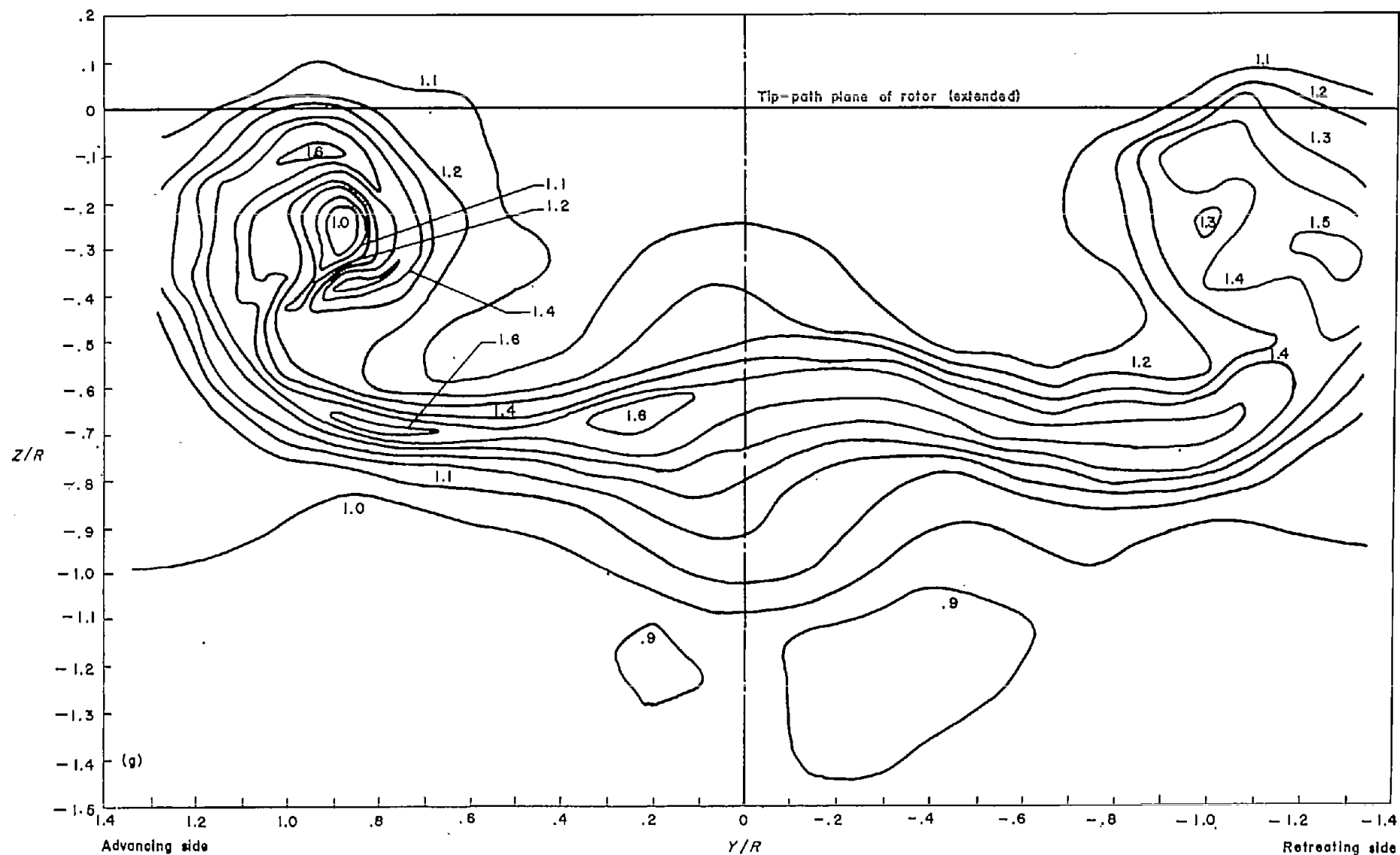
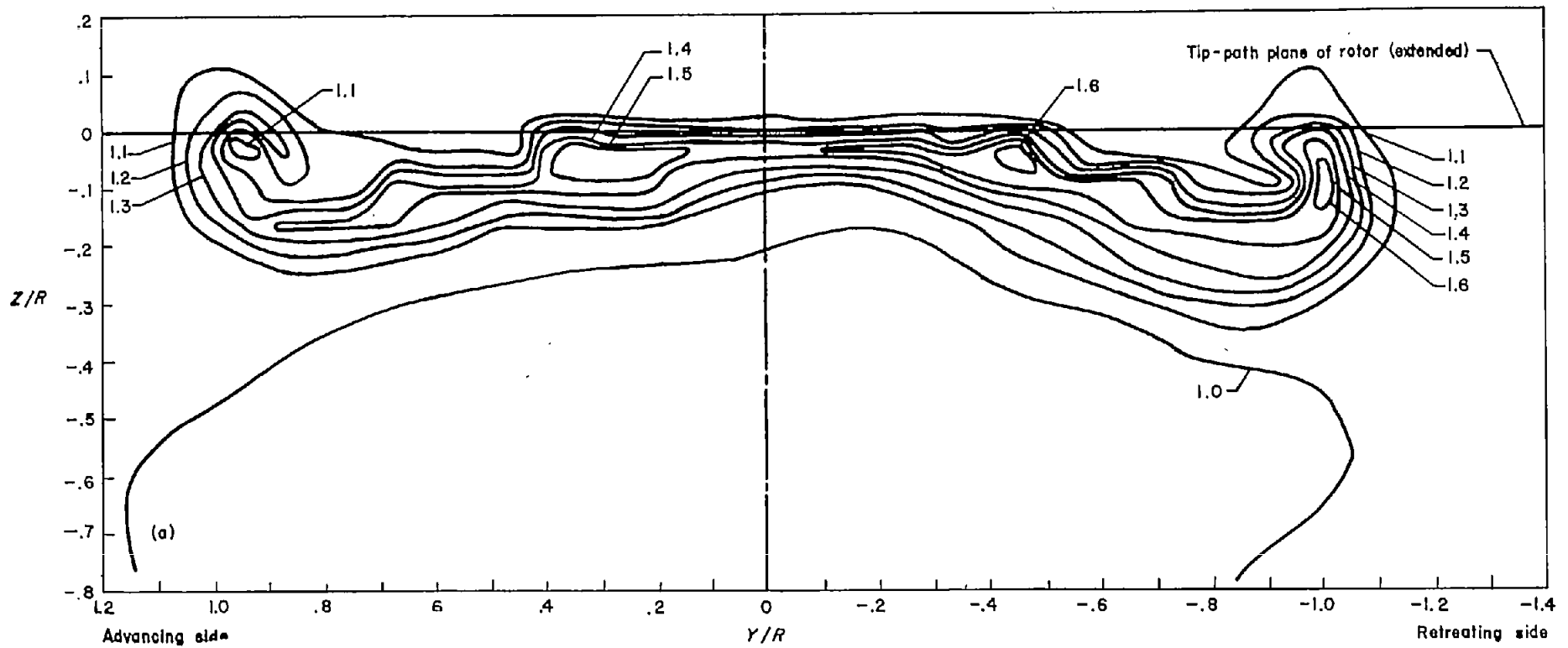
(f) $X/R=2.07$.

FIGURE 46.—Continued.

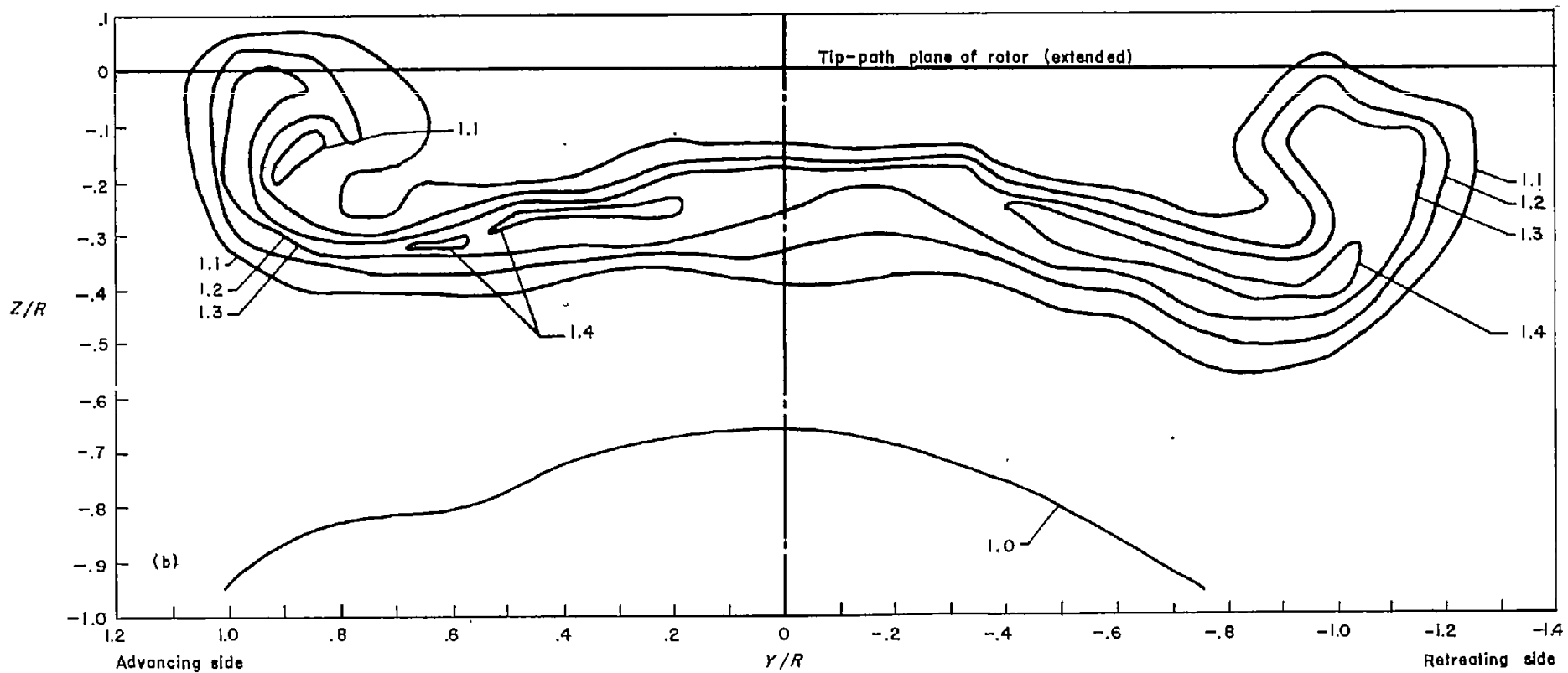


(g) $X/R=3.14$.
FIGURE 40.—Concluded.



(a) $X/R=1.07$.

Figure 47.—Contours of dynamic pressure q/q_0 in the vicinity of rotor. $\chi=82.3^\circ$; $\mu=0.140$.



(b) $X/R=2.07$.
FIGURE 47.—Continued.

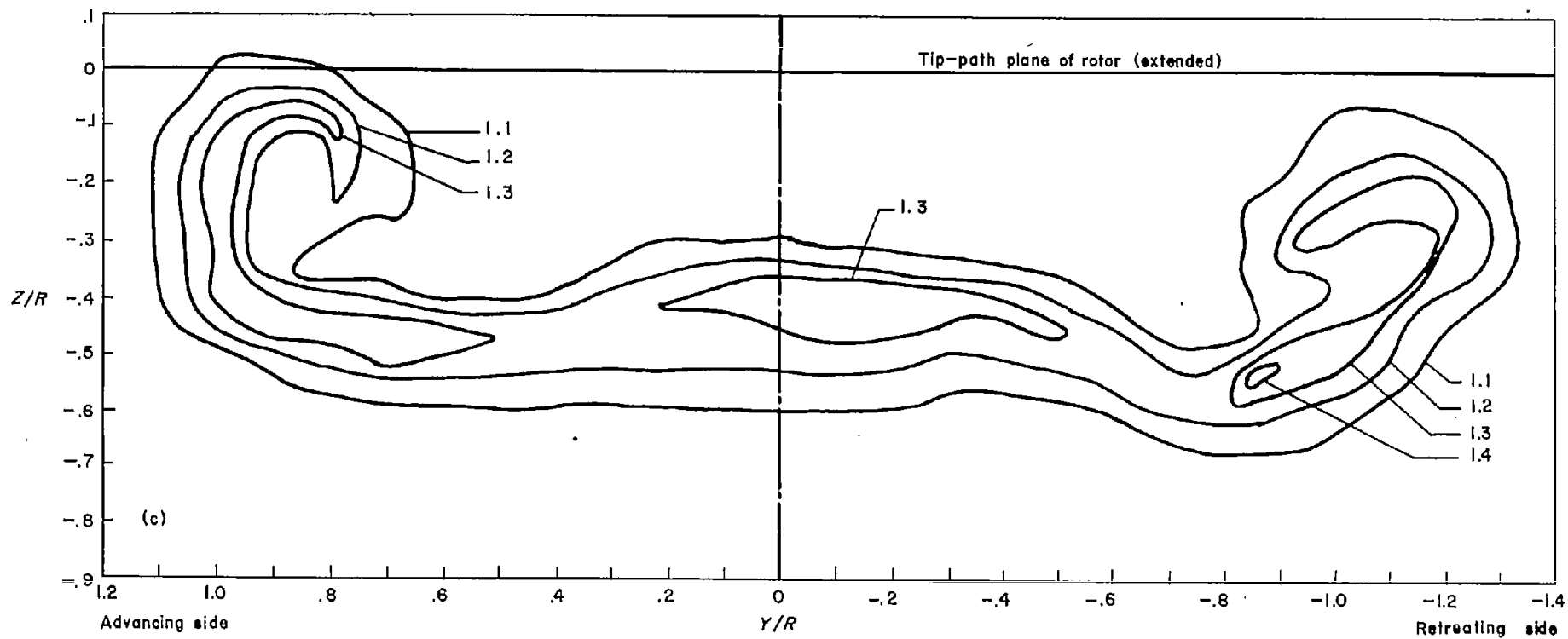
(c) $X/R=3.14$.

FIGURE 47.—Concluded,

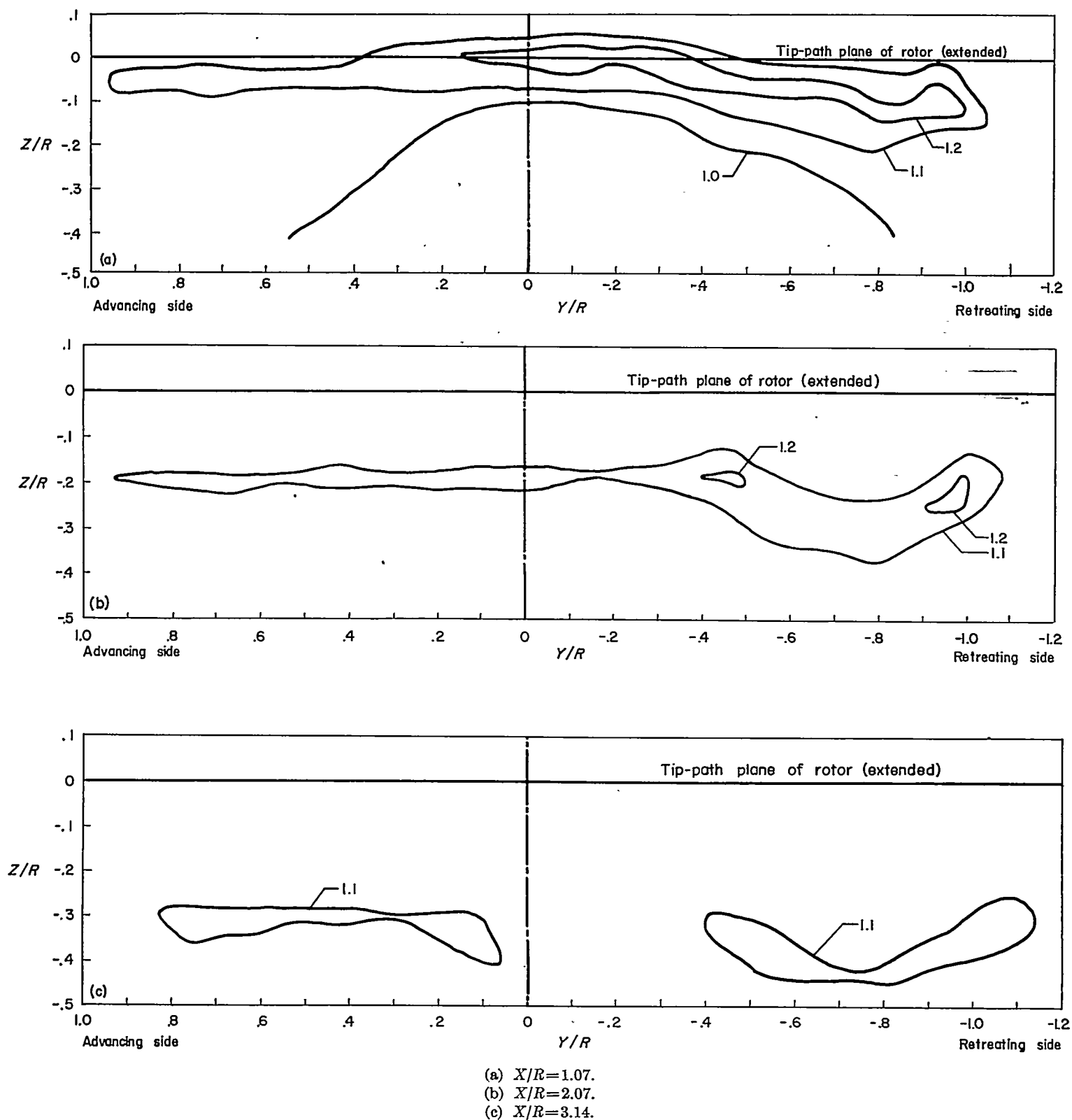


FIGURE 48.—Contours of dynamic pressure q/q_0 in the vicinity of the rotor. $\chi=83.9^\circ$; $\mu=0.232$.

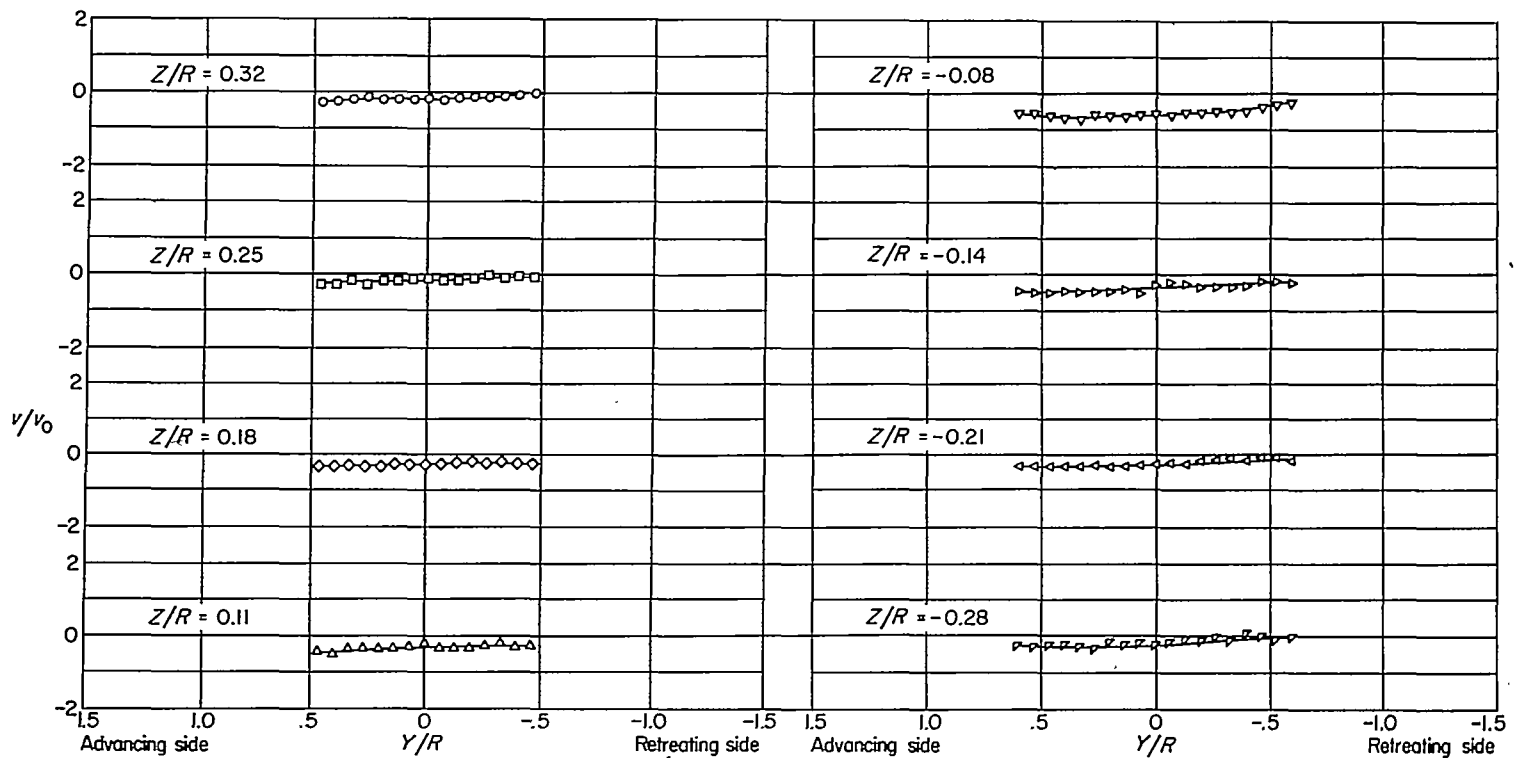


FIGURE 49.—Measured values of induced-velocity ratio v/v_0 . $X/R = -1.0$; $\chi = 75.0^\circ$; $\mu = 0.095$.

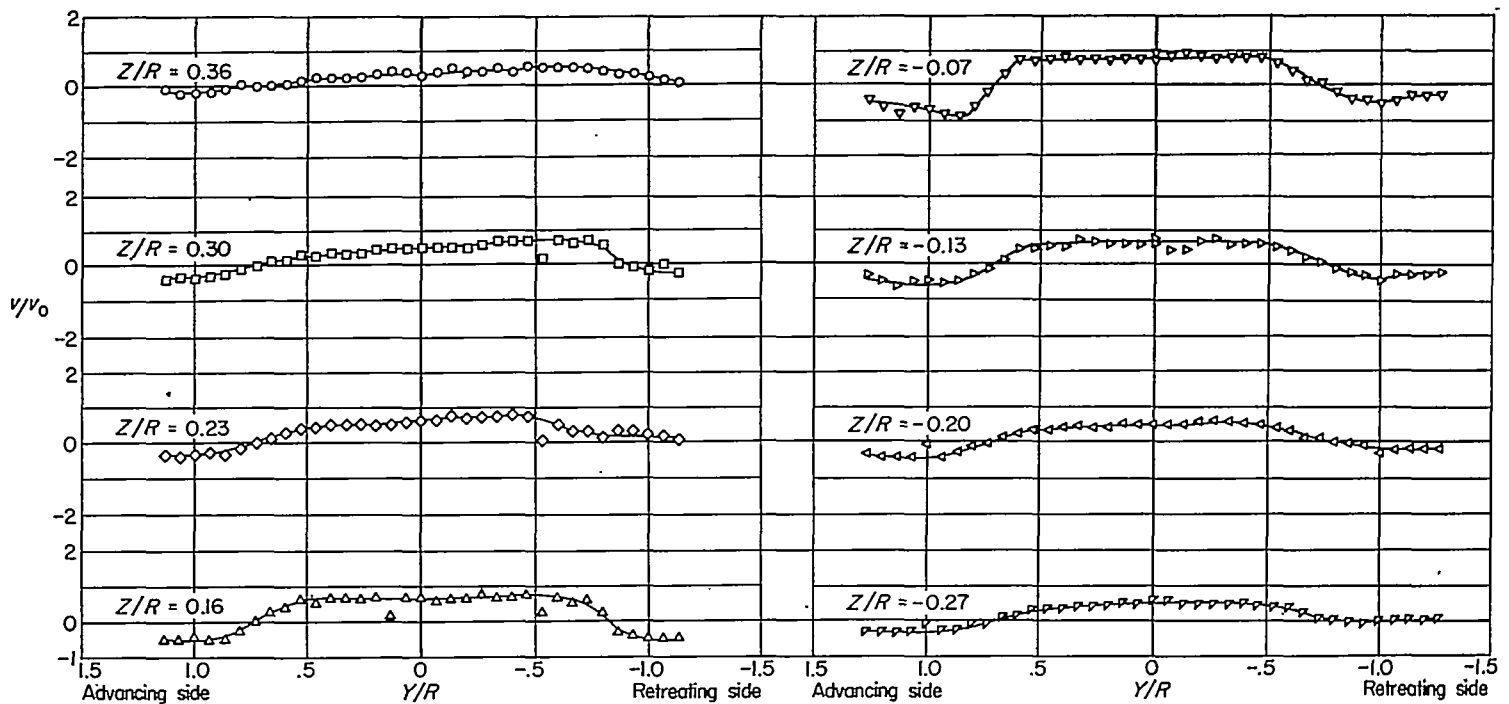
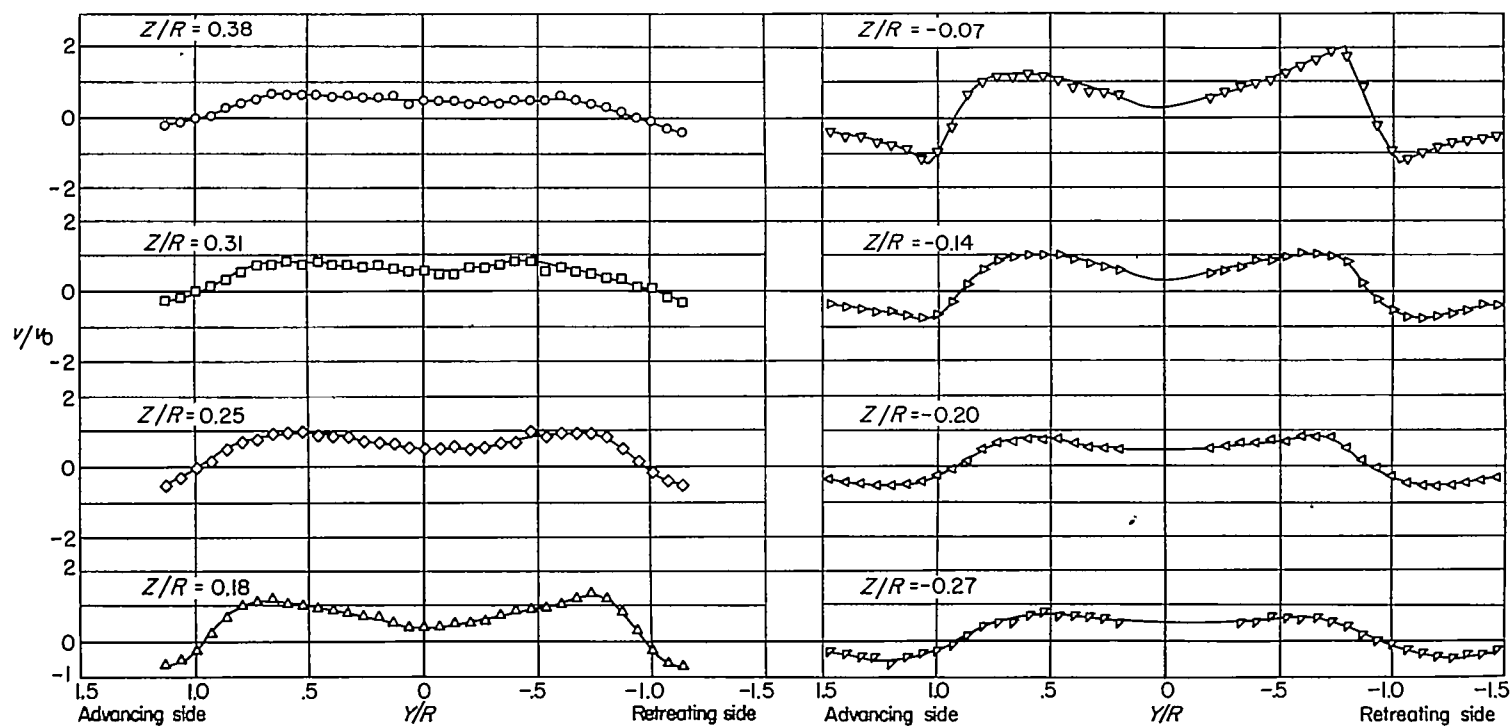
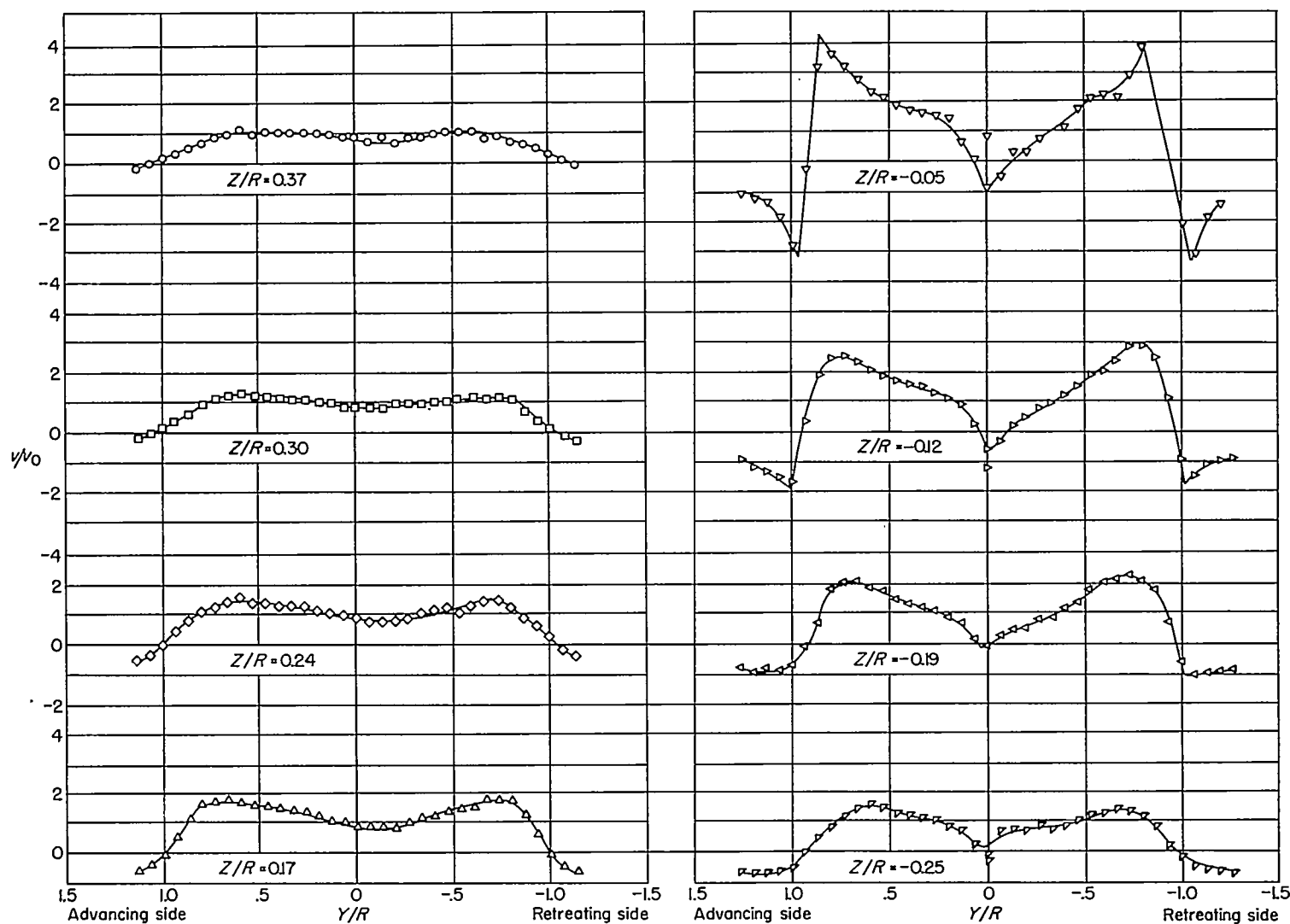


FIGURE 50.—Measured values of induced-velocity ratio v/v_0 . $X/R = -0.5$; $\chi = 75.0^\circ$; $\mu = 0.095$.

FIGURE 51.—Measured values of induced-velocity ratio v/v_0 . $X/R=0$; $\chi=75.0^\circ$; $\mu=0.095$.FIGURE 52.—Measured values of induced-velocity ratio v/v_0 . $X/R=0.5$; $\chi=75.0^\circ$; $\mu=0.095$.

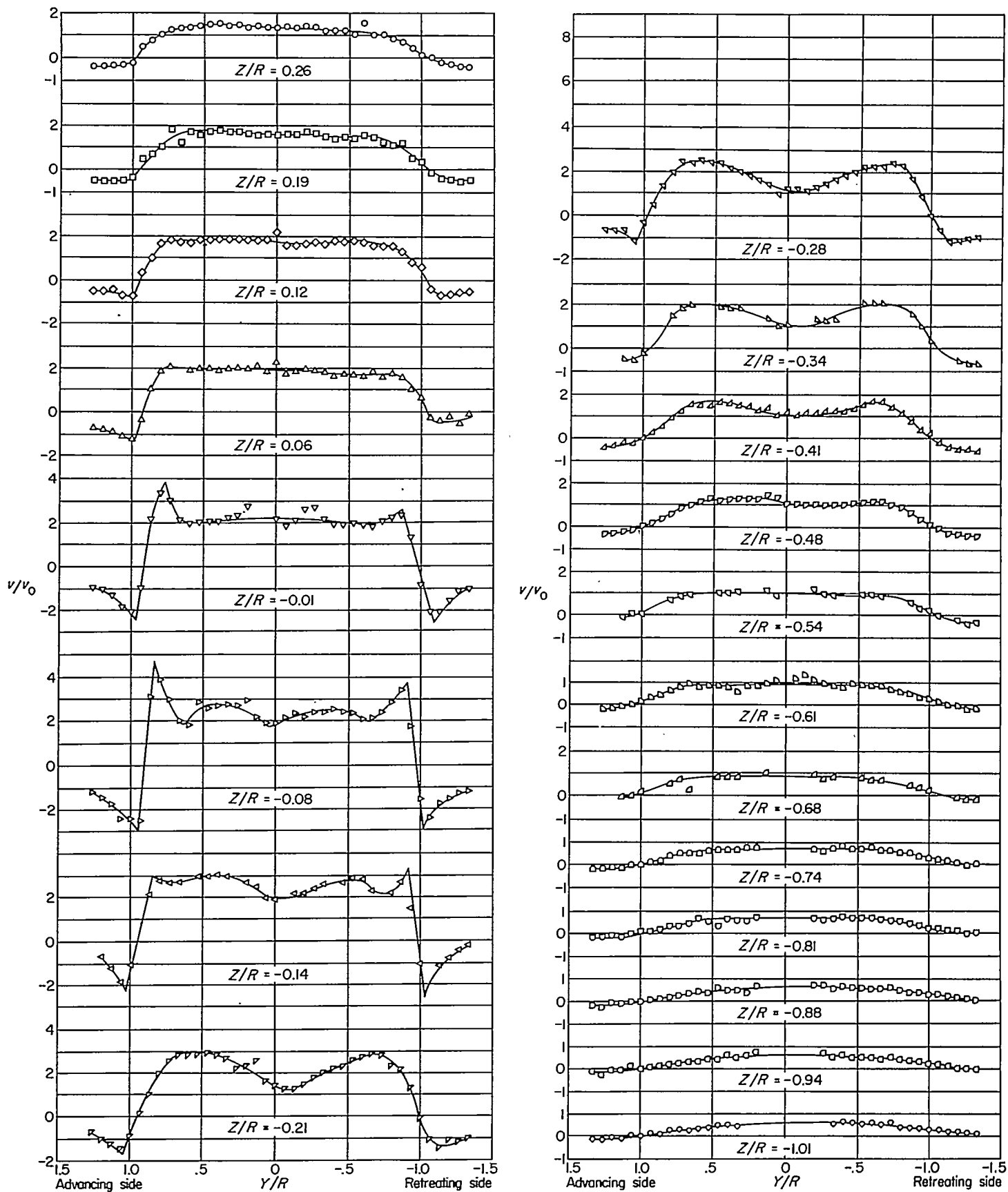
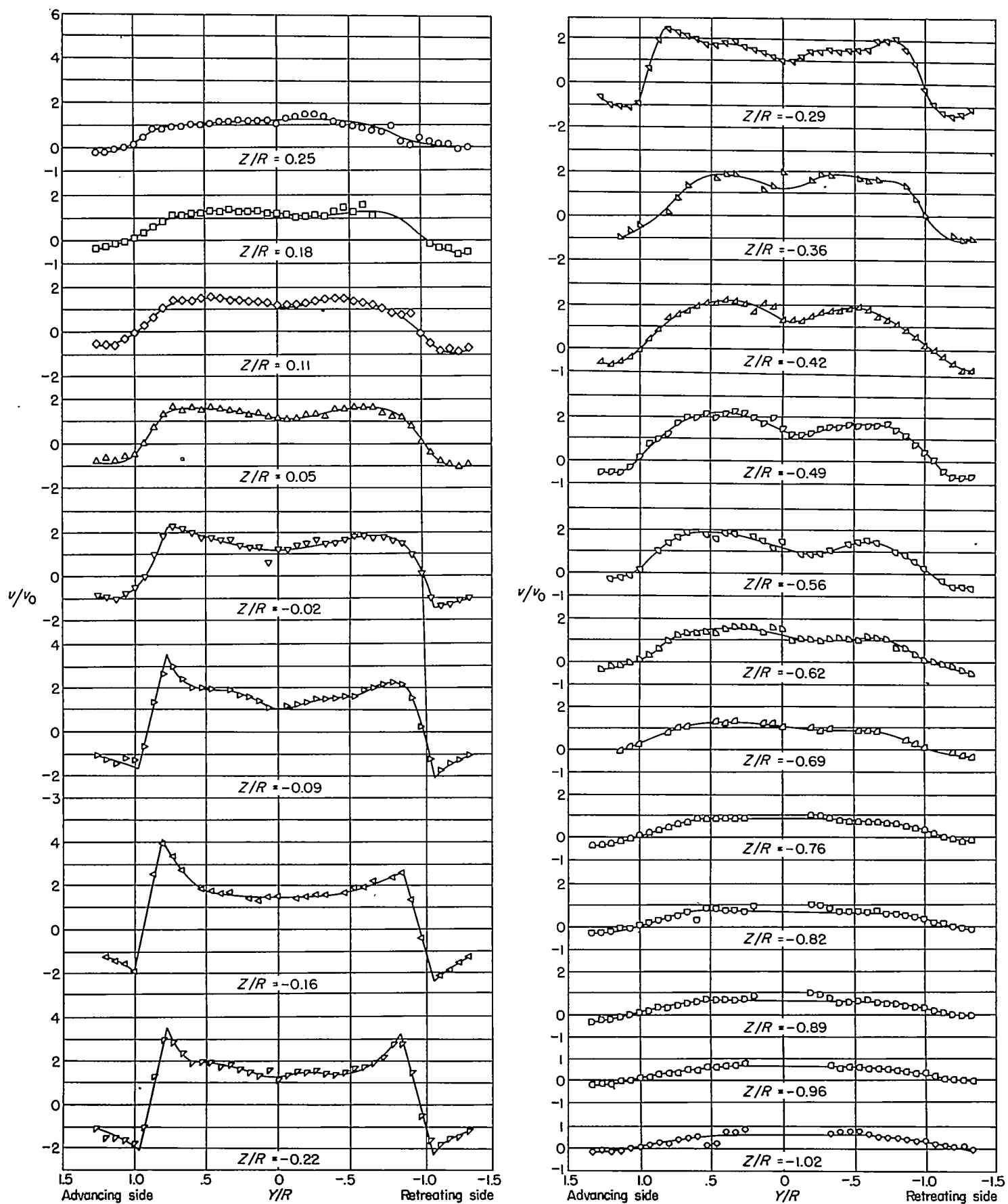


FIGURE 53.—Measured values of induced-velocity ratio v/v_0 . $X/R=1.07$; $\chi=75.0^\circ$; $\mu=0.095$.

FIGURE 54.—Measured values of induced-velocity ratio v/v_0 . $X/R=2.07$; $\alpha=75.0^\circ$; $\mu=0.095$.

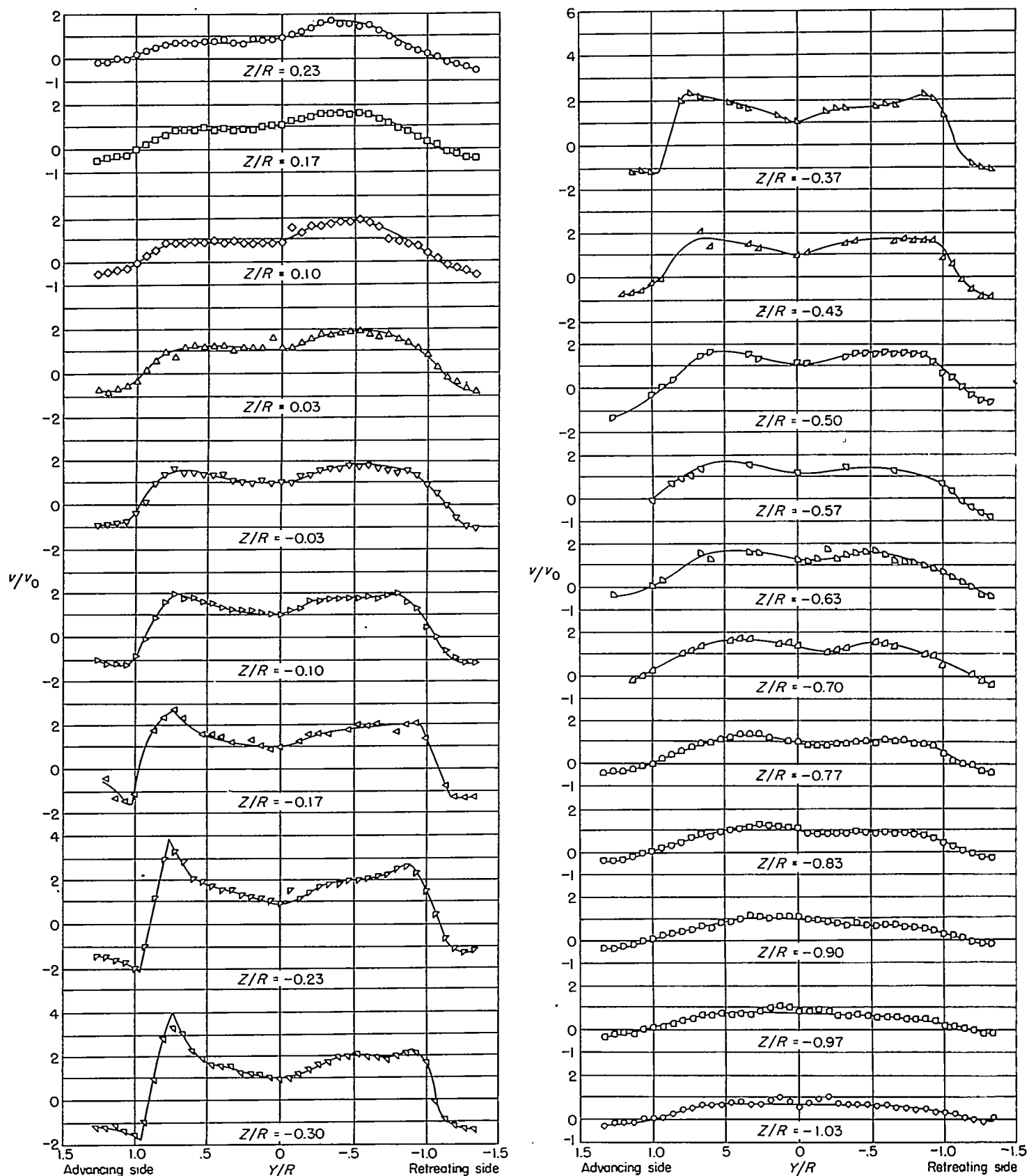
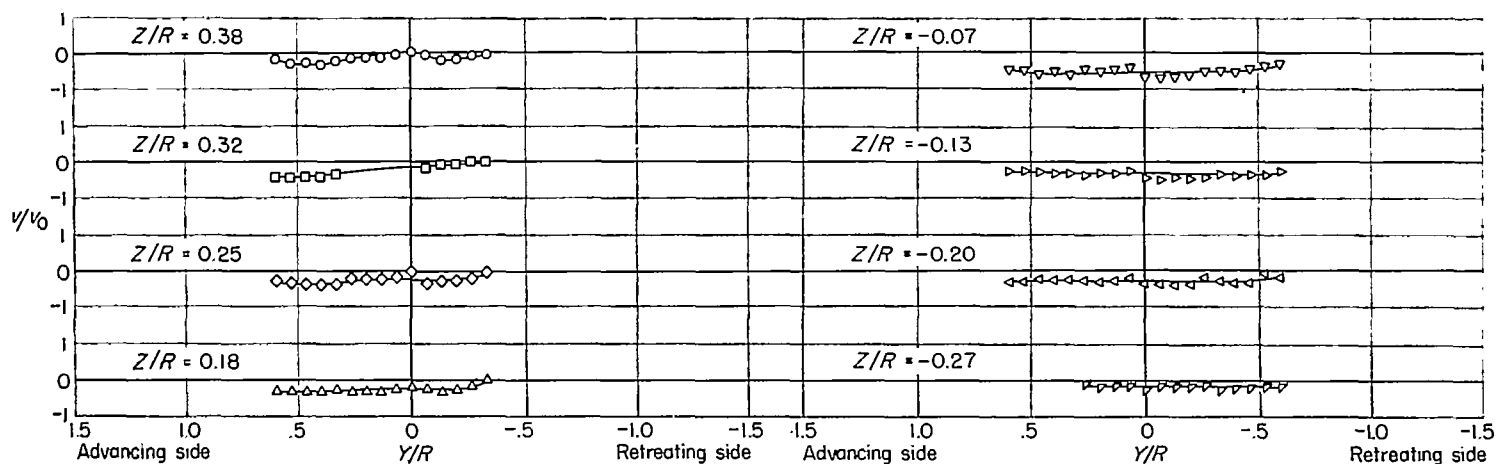
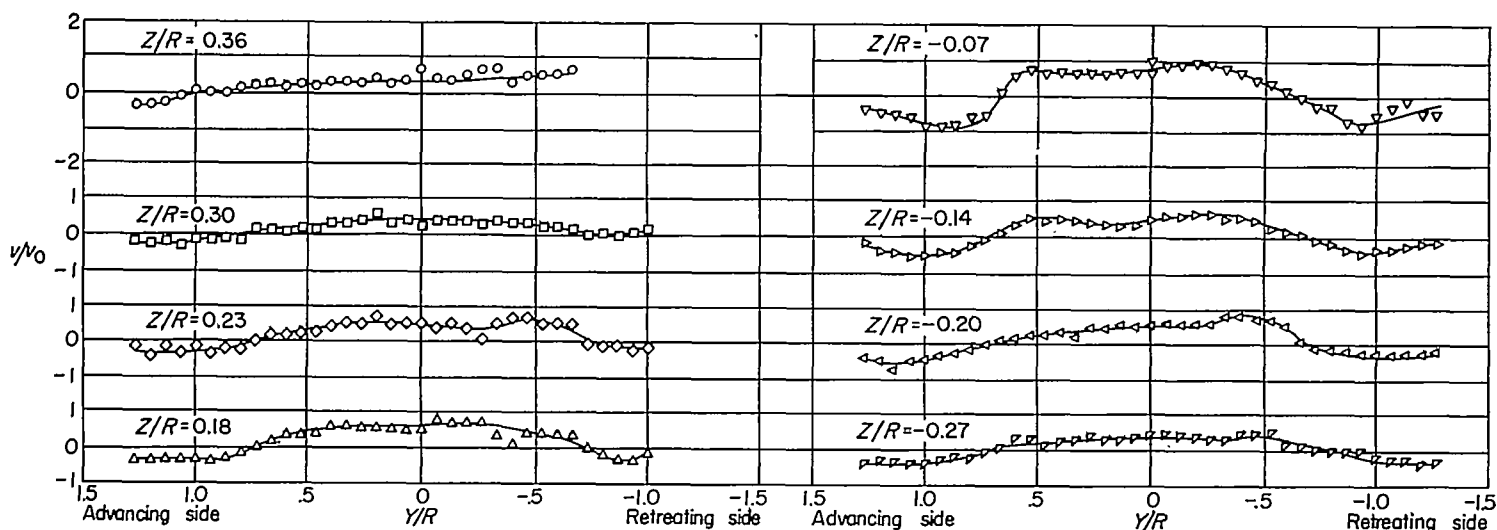
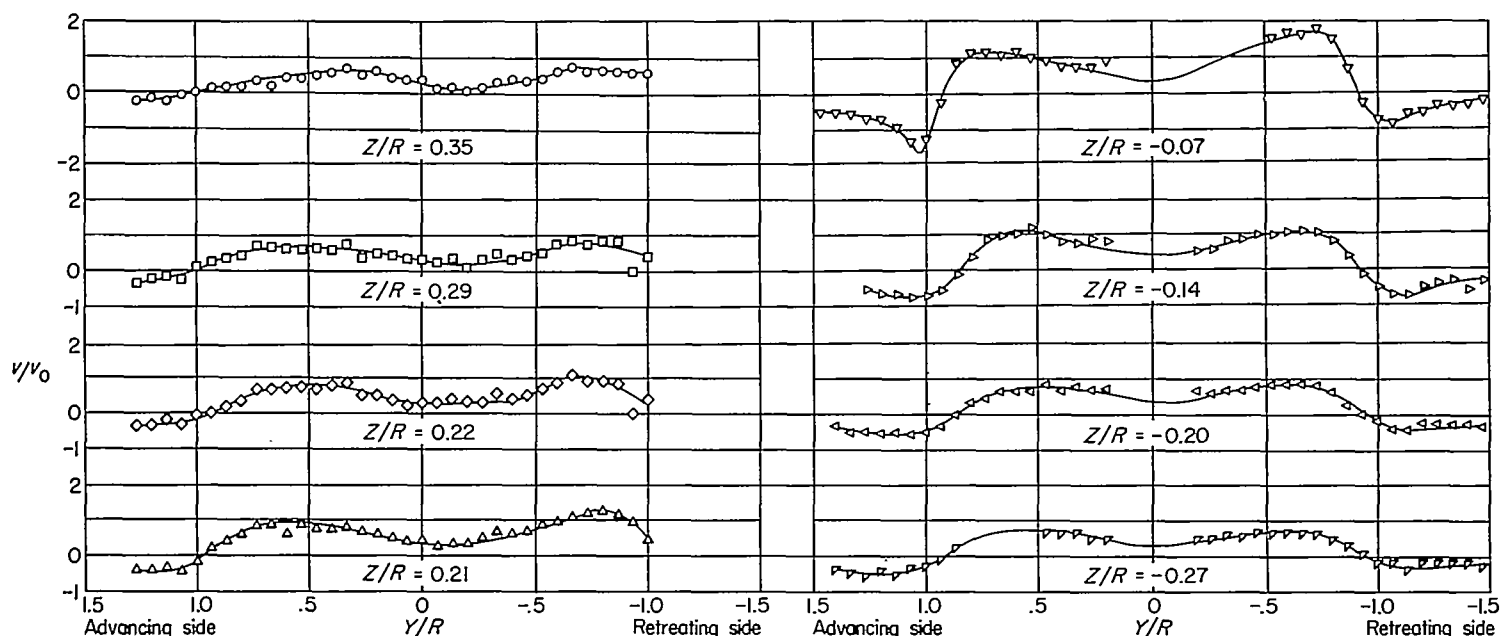


FIGURE 55.—Measured values of induced-velocity ratio v/v_0 . $X/R=3.14$; $\chi=75.0^\circ$; $\mu=0.095$.

FIGURE 56.—Measured values of induced-velocity ratio v/v_0 . $X/R = -1.0$; $\chi = 82.3^\circ$; $\mu = 0.140$.FIGURE 57.—Measured values of induced-velocity ratio v/v_0 . $X/R = -0.5$; $\chi = 82.3^\circ$; $\mu = 0.140$.FIGURE 58.—Measured values of induced-velocity ratio v/v_0 . $X/R = 0$; $\chi = 82.3^\circ$; $\mu = 0.140$.

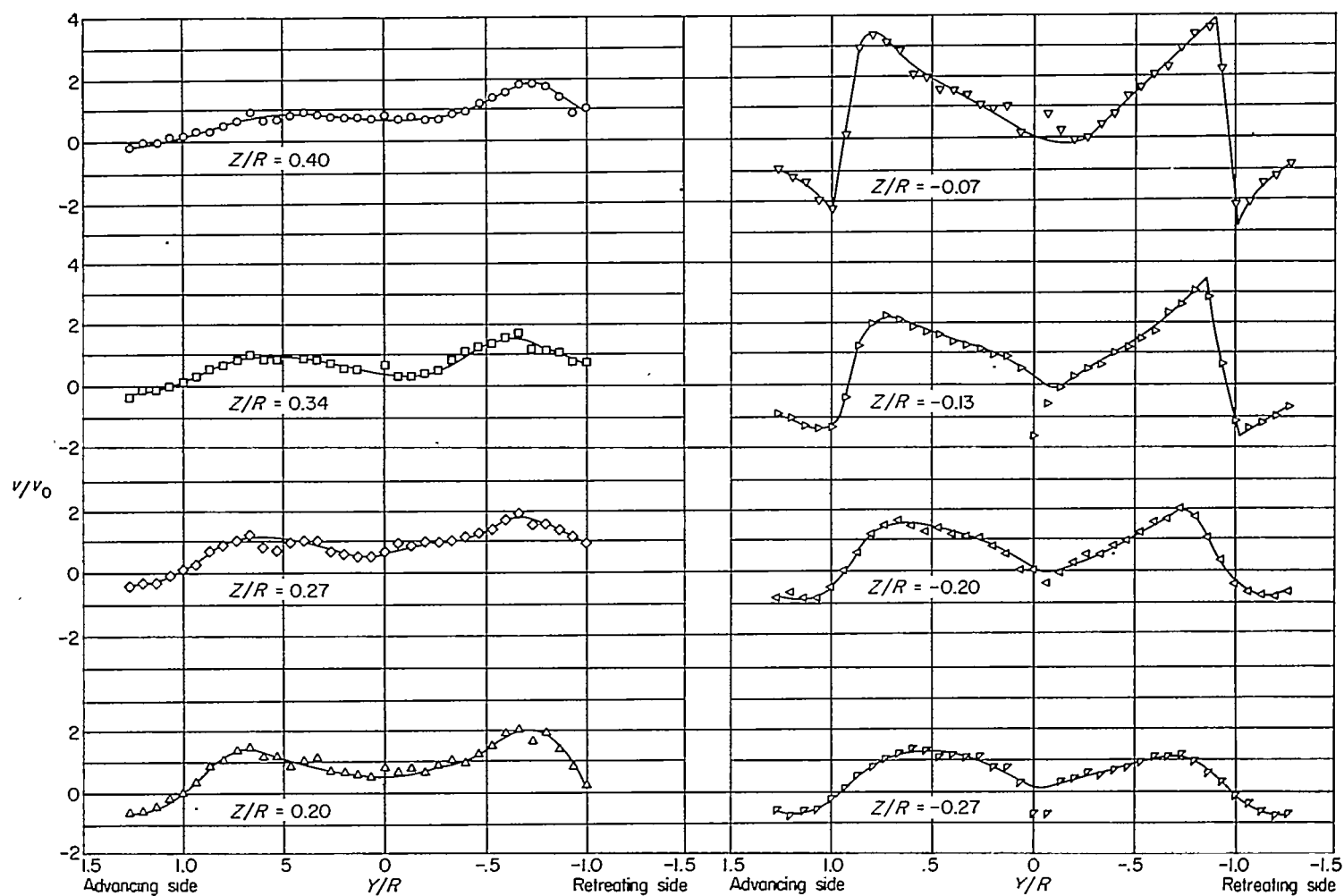


FIGURE 59.—Measured values of induced-velocity ratio v/v_0 . $X/R=0.5$; $\chi=82.3^\circ$; $\mu=0.140$.

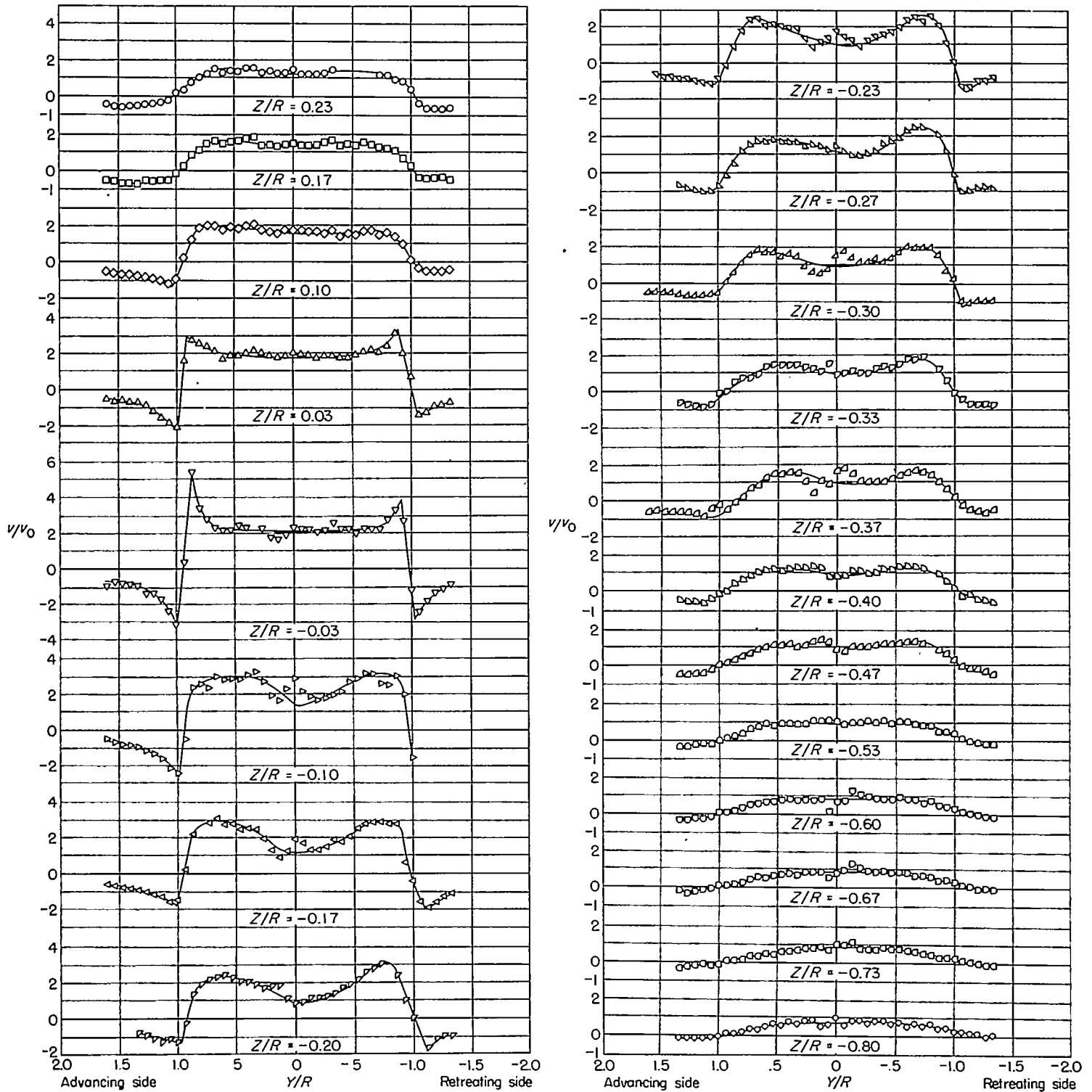


FIGURE 60.—Measured values of induced-velocity ratio v/v_0 . $X/R=1.07$; $\alpha=82.3^\circ$; $\mu=0.140$.

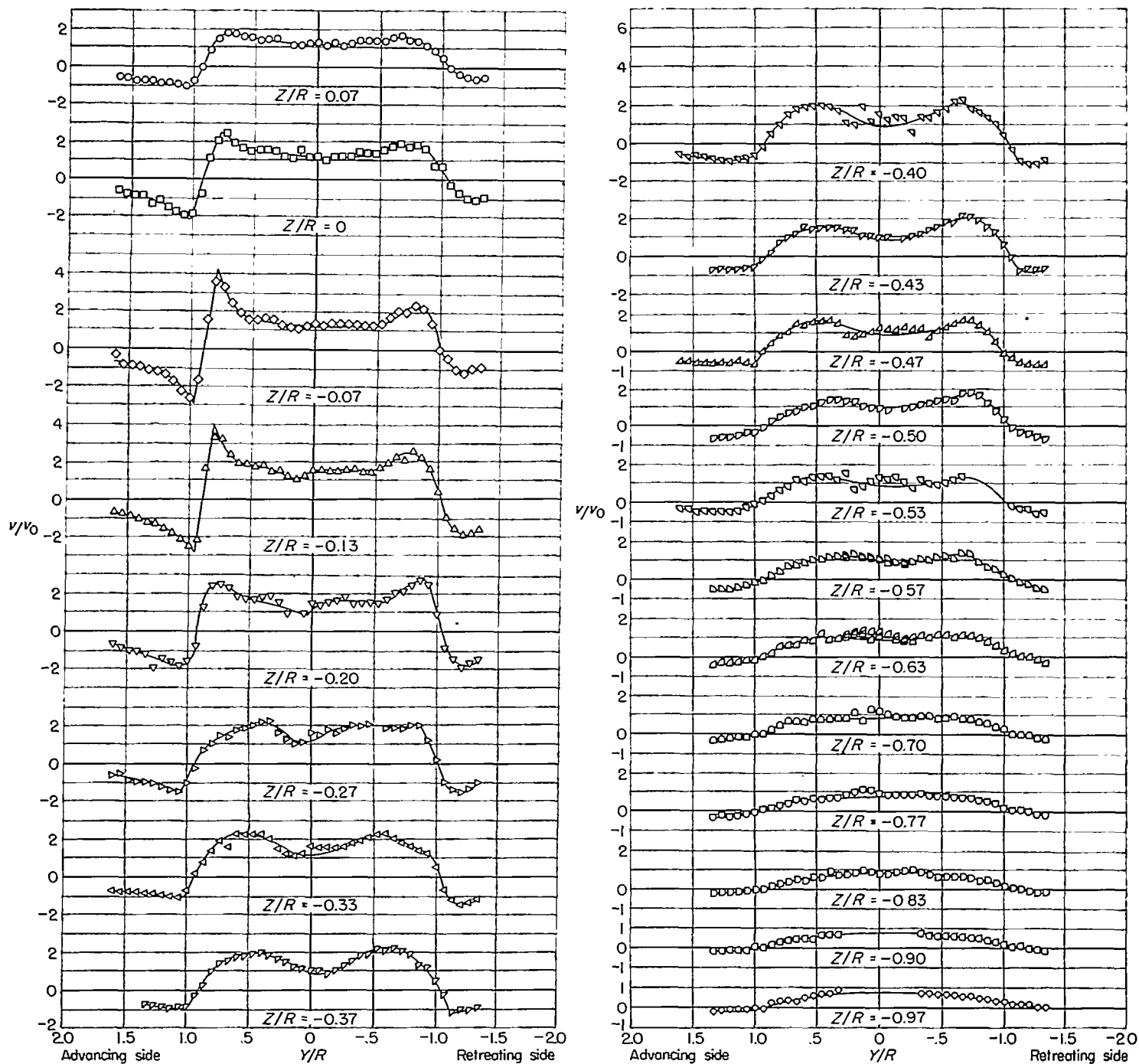


FIGURE 61.—Measured values of induced-velocity ratio v/v_0 . $X/R=2.07$; $\chi=82.3^\circ$; $\mu=0.140$.

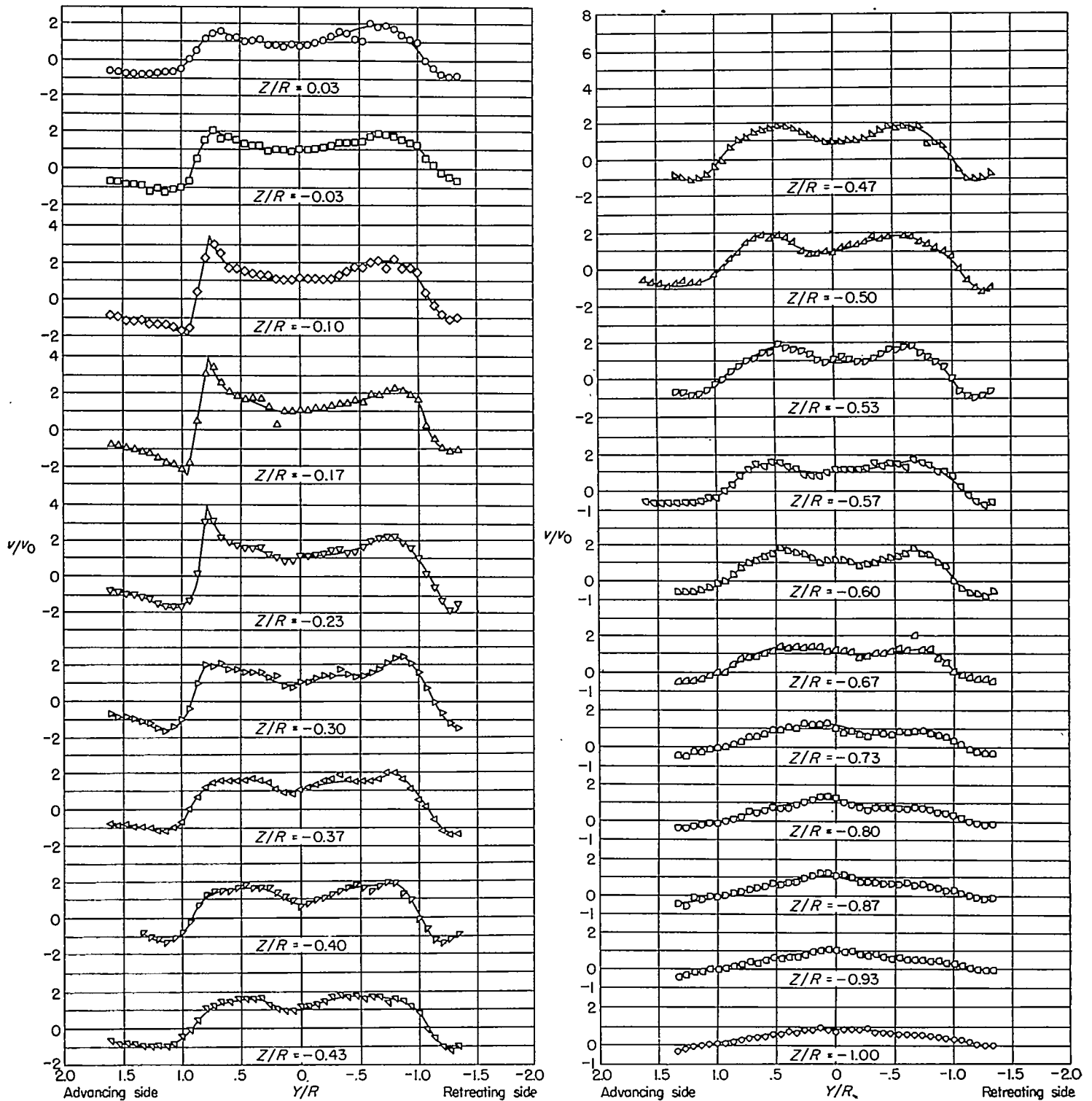


FIGURE 62.—Measured values of induced-velocity ratio v/v_0 . $X/R = 3.14$; $\chi = 82.3^\circ$; $\mu = 0.140$.

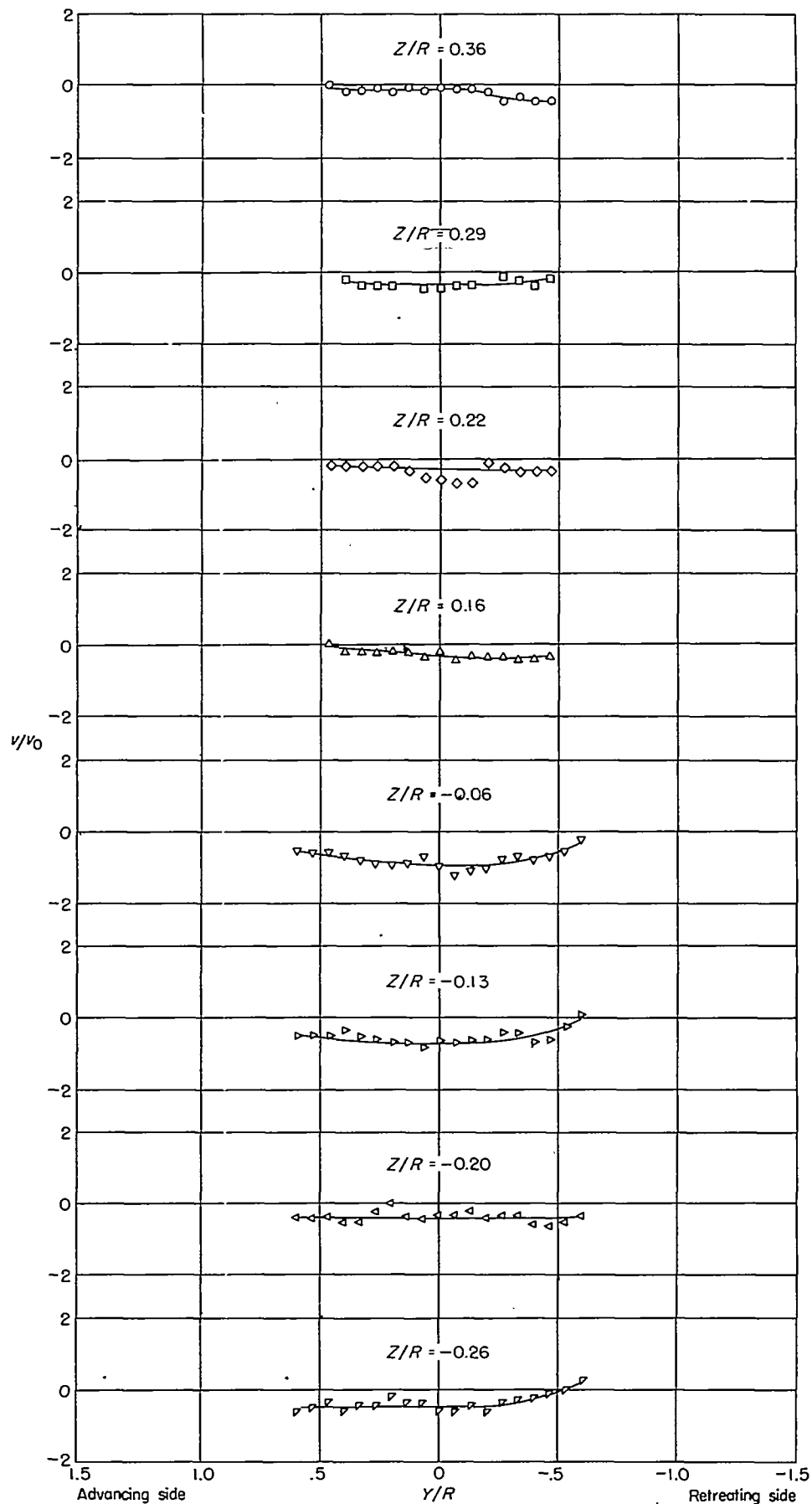


FIGURE 63.—Measured values of induced-velocity ratio v/v_0 . $X/R = -1.0$; $\alpha = 83.9^\circ$; $\mu = 0.232$.

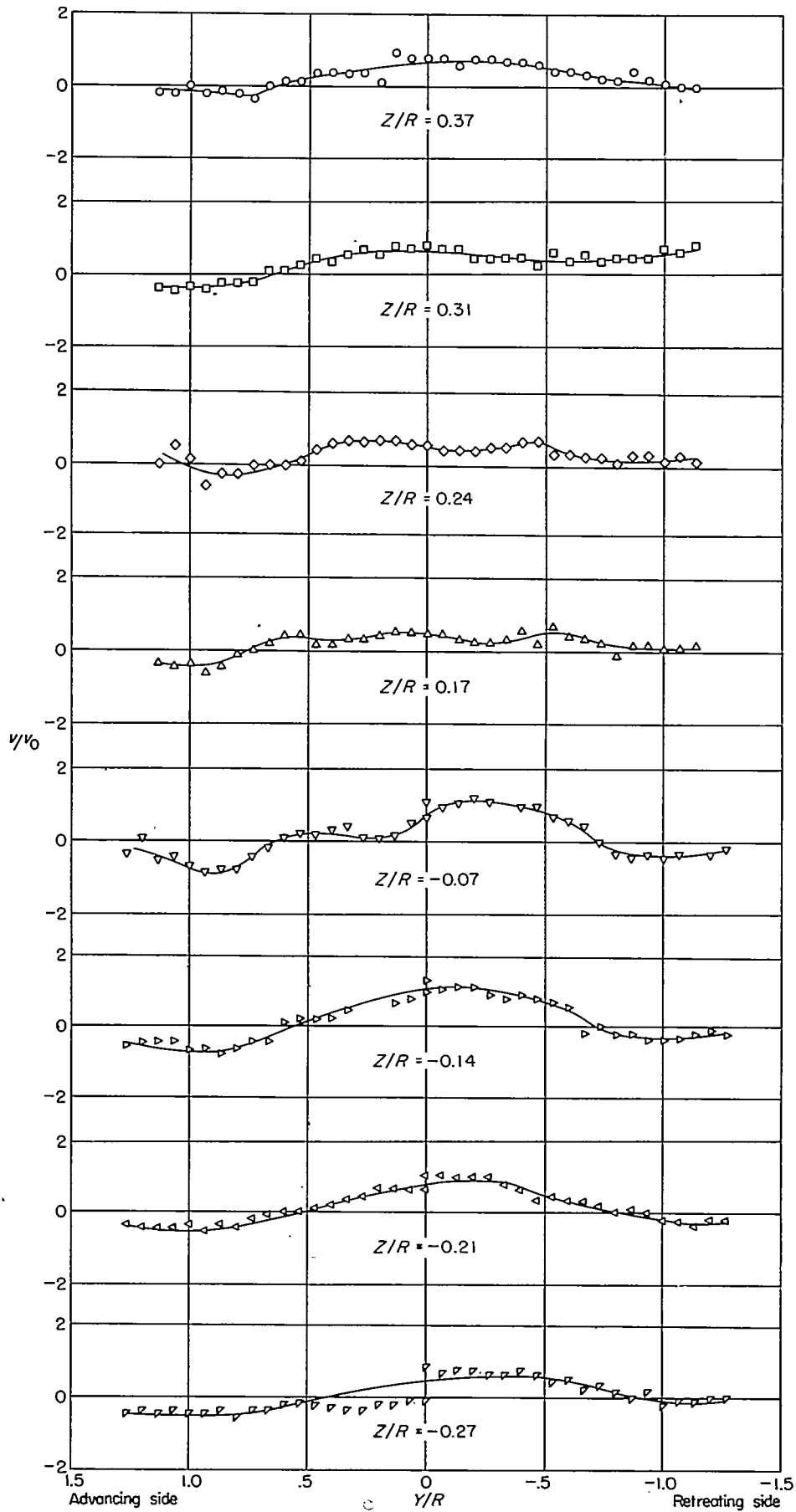


FIGURE 64.—Measured values of induced-velocity ratio v/v_0 . $X/R = -0.5$; $\chi = 83.9^\circ$; $\mu = 0.232$.

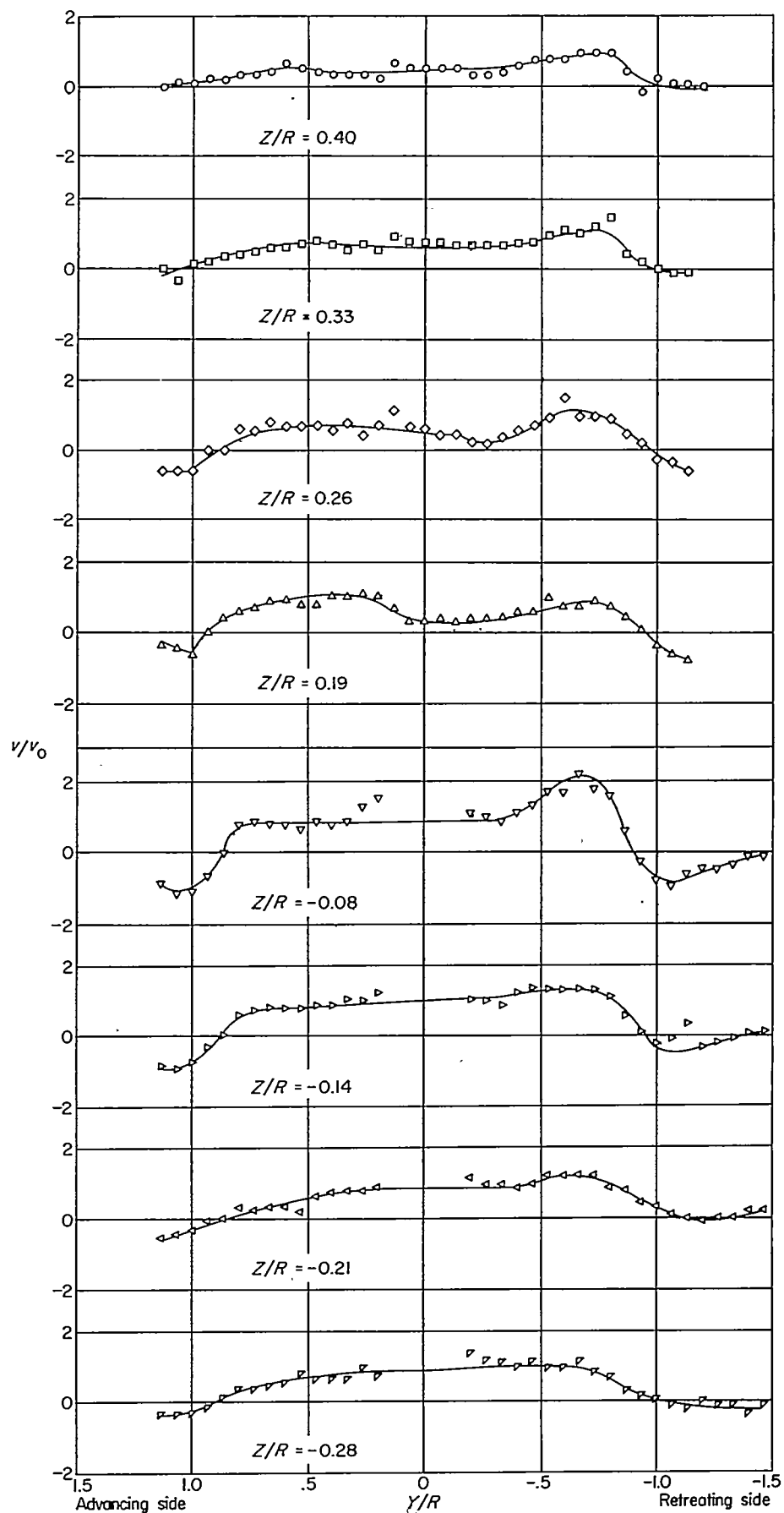


FIGURE 65.—Measured values of induced-velocity ratio v/v_0 . $X/R=0$; $\alpha=83.9^\circ$; $\mu=0.232$.

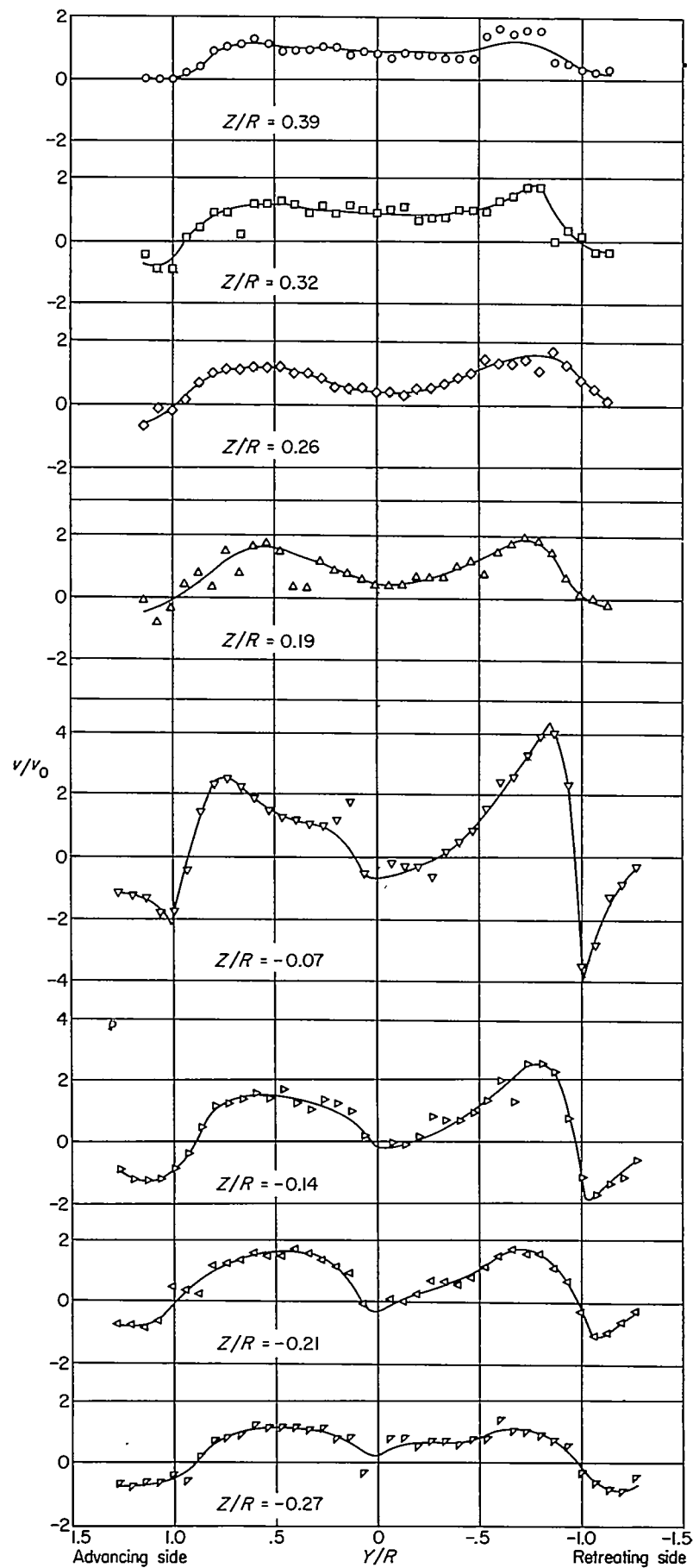


FIGURE 66.—Measured values of induced-velocity ratio v/v_0 . $X/R=0.5$; $\chi=83.9^\circ$; $\mu=0.232$.

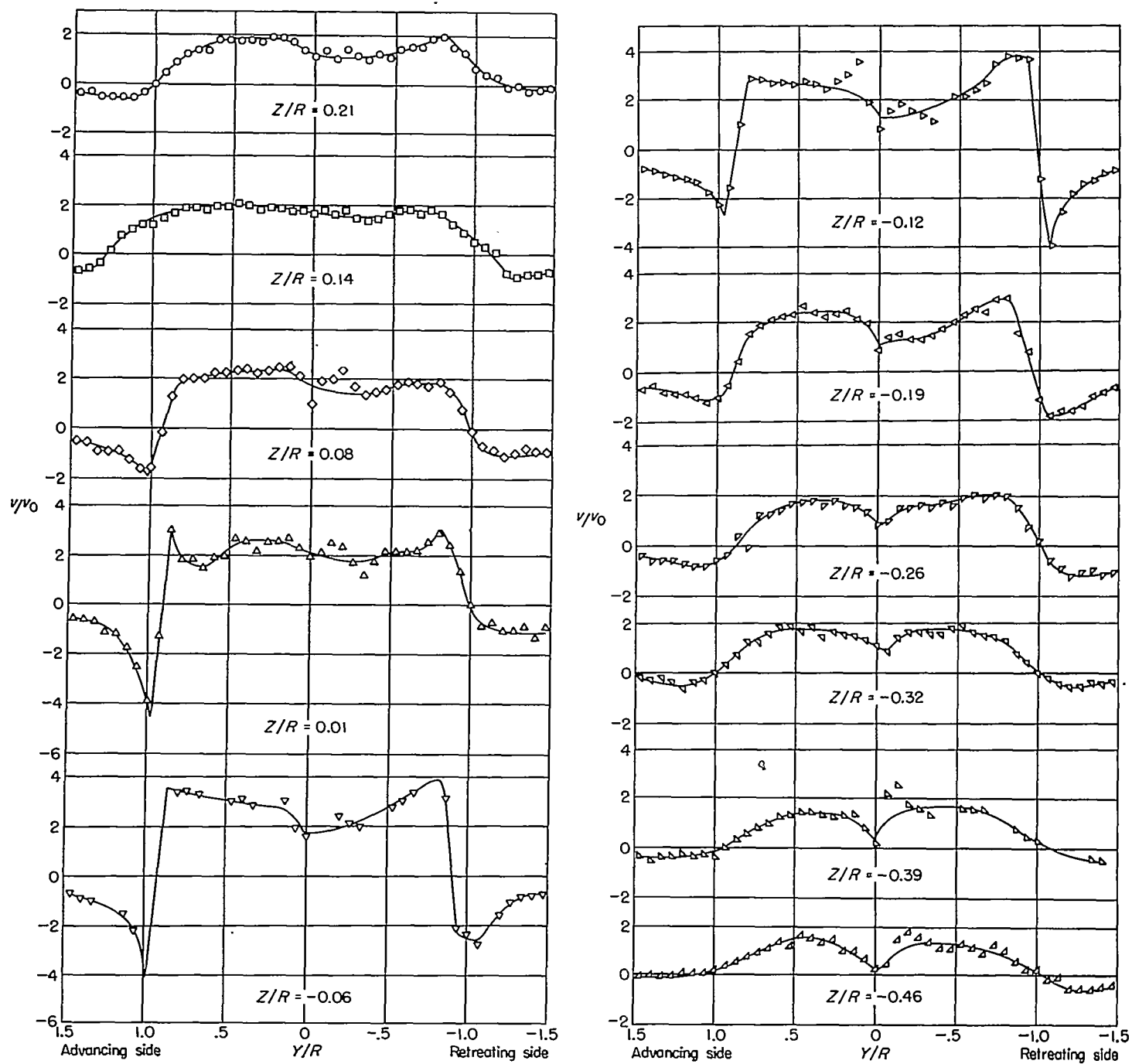


FIGURE 67.—Measured values of induced-velocity ratio v/v_0 . $X/R=1.07$; $\chi=83.9^\circ$; $\mu=0.232$.

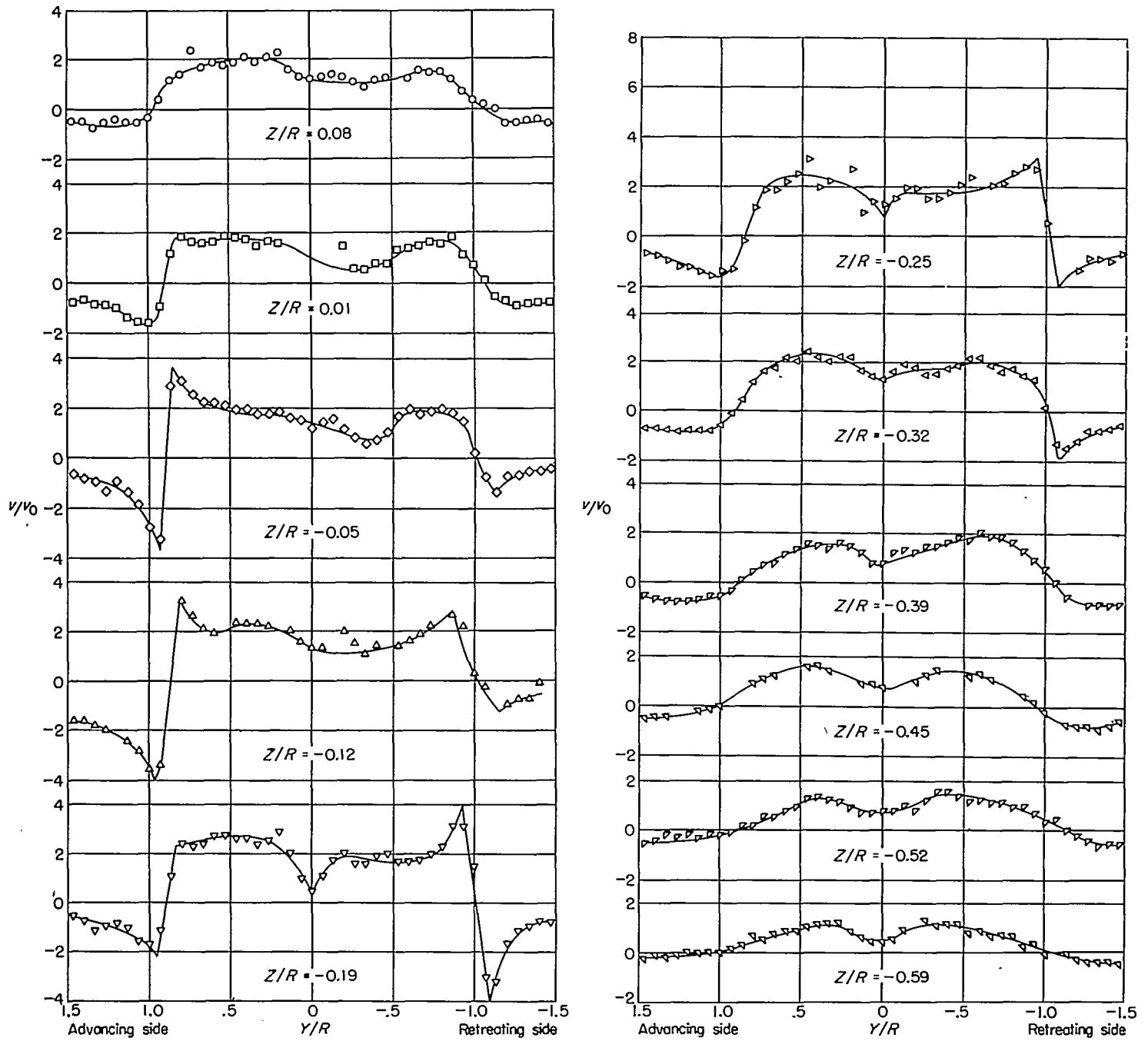


FIGURE 68.—Measured values of induced-velocity ratio v/v_0 . $X/R=2.07$; $\chi=83.9^\circ$; $\mu=0.232$.

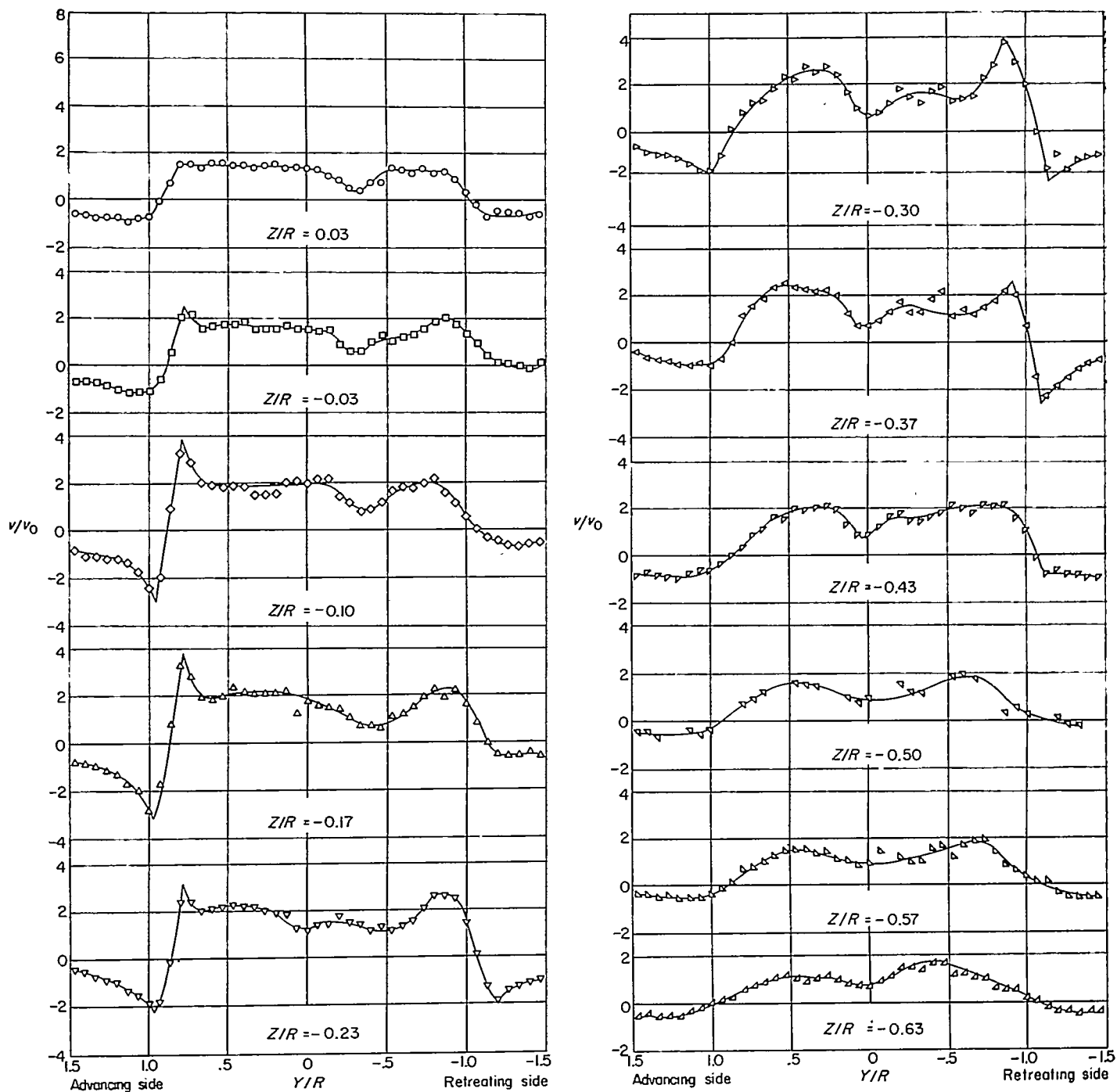


FIGURE 69.—Measured values of induced-velocity ratio v/v_0 . $X/R=3.14$; $\chi=83.9^\circ$; $\mu=0.232$.